Optical Emission Spectroscopy of ultra-short Laser-induced Plasmas

Inaugural-Dissertation

zur Erlangung des Doktorgrades
der Mathematisch-Naturwissenschaftlichen Fakultät
der Heinrich-Heine-Universität Düsseldorf

vorgelegt von
Steffen Mittelmann
aus Schwelm

Düsseldorf, November 2022

aus dem Institut für Laser- und Plasmaphysik
der Heinrich-Heine-Universität Düsseldorf

Gedruckt mit der Genehmigung der
Mathematisch-Naturwissenschaftlichen Fakultät
der Heinrich-Heine-Universität Düsseldorf

Berichterstatter:

1. Prof. Dr. Georg Pretzler
Institut für Laser- und Plasmaphysik
Heinrich-Heine-Universität Düsseldorf

2. PD Dr. Götz Lehmann
Institut für Theoretische Physik I
Heinrich-Heine-Universität Düsseldorf

Tag der mündlichen Prüfung:
27.01.2023

Abstract

Optical Emission Spectroscopy (OES) is widely known and applied to classical plasmas found in industry and laboratories for various applications. These plasmas exhibit temperatures of a few eV, which is "cold" compared to early stage laser-induced plasmas. Still, those are of high interest in material diagnostic application, which is called Laser-Induced Breakdown Spectroscopy (LIBS).

LIBS is a powerful, versatile, low invasive tool to quickly analyze the material composition of diverse kinds of samples. For example, it can be used to detect minor elements and isotopes in alloys or other material mixtures, independent of their state of matter and physical form. Moreover, it brings material information without the need for any sample preparation, which makes it suitable for on-line and hands-off experiments in inaccessible areas, for example in space or in nuclear safety zones. For these reasons, LIBS and a few other laser-induced diagnostics are proposed to be used to detect depositions and fuel retention in plasma-facing components of the inner walls of magnetic confinement fusion reactor vessels as *in-situ* techniques. Their applicability can be tested in experimental fusion facilities like, without limitation, EAST in China, ITER in France, or Wendelstein 7-X in Germany.

This thesis intends to describe the ultra-short laser-induced plasma expansion dynamic in different environments with the focus on femtosecond lasers in high vacuum conditions. The research question treated is whether ultra-short femtosecond LIBS can be a reasonable alternative in the described context inside the fusion vessel. Here, a collection of different experiments is presented using several laser systems. In the beginning, the laser ablation characteristic of lasers with strongly deviating pulse duration in vacuum will be compared in an extensive study on the test material tantalum. This comparison will be followed by comprehensive examinations of the plasma induced by sub-10-fs pulses in vacuum using an imaging system and time resolved OES. Regarding the initial objective, this part will demonstrate some challenges in the use of these laser pulses in LIBS analyses and propose a tool to improve their applicability. This tool is a pre-pulse module that brings the opportunity to enhance the emitted spectral intensity of the expanding plasma and decreases the detection limit of certain species in the plasma.

The fuels in the fusion reactor are basically the heavier isotopes of hydrogen: deuterium and tritium. As the objective of this thesis includes the quantification of fuel retention in the plasma-facing components, two closing experiments will be presented demonstrating the feasibility of hydrogen isotope detection in high-Z metals tungsten and tantalum with a nanosecond- and a femtosecond laser. Here, a calibration free LIBS approach is applied to determine the total amount of deuterium retention in these metal tiles. The results are shown to be in good agreement with Thermal Desorption Spectroscopy (TDS) data, which makes this a meaningful proof-of-principle experiment for further applications in this context.

To gain a deeper understanding of the fundamentals of laser-plasma coupling, ablation processes, and plasma expansion, this thesis aspires to give a review on the physical concepts behind the effects observed in experiments integrated in published literature in the field.

Contents

Chapter 1

Introduction

With a rising need for energy, in particular electricity, with more and more industrialized countries all over the world, the biggest challenge in the 21st century is the development of more carbon emission free (or limited) energy sources. For example, rising industrial states like China increased their need for electricity by 14.7 % between 2018 and 2021 to 8.31×10^{12} kWh as shown in ref. [1]. Although, sustainable power plants using wind, water, solar, biomass, or geothermal energy having rising influence in the overall production, still a huge amount of fossil fuel based sources are used, which tend to emit too much CO_2 and are presumed to be one of the main driver for human made climate change effects, see ref. [2]. According to the Federal Statistical Office of Germany (ref. [3]), the whole electricity production in Germany of 582.9 TWh in 2021 was composed by 39.7 % of sustainable sources, 48.5 % fossil fuels and others, and 11.8 % nuclear sources. The mentioned nuclear power plants basically generate heat from induced fission processes in the heavy metal uranium. This process involves the production of radioactive fission products that has to be stored safely for several decades. This and the invasive mining of the raw uranium does not make it a reliable source for the future energy production. Instead, extensive studies were set on the opportunity to use the fusion of light elements (e.g. hydrogen and its isotopes deuterium and tritium) to generate a scalable energy source providing emission free power in the near future. The next sections first give an overview on the operation mode and technical conditions of possible magnetic confinement fusion reactors, second it presents the opportunity to use a laser-based diagnostic to ensure a secure operation of a fusion reactor, and lastly formulate the research objective of this thesis.

Magnetic Confinement Fusion

Although the work presented in this thesis does not include actual applications of the motivated laser-based diagnostic in a current fusion experiment, a short overview of this promising technique is necessary as a motivation. Therefore a brief overview of the path of fusion experiments and a description of the necessary plasma parameters will follow.

In 1950 Andrei Sakharov and Igor Tamm proposed the first design of a magnetic confinement fusion experiment, the tokamak [4], while Lyman Spitzer presented his concept of the stellarator in 1958 [5]. Today, both designs have been tested in various experiments over the whole world. The tokamak designed JET (Joint European Torus) in Culham, UK achieved first large-scale tests of deuterium-tritium reactions in 1991 with a fusion power of 2 MW in 2 s (see ref. [6]). Likewise, the stellarator designed Wendelstein 7-X in Greifswald, Germany was able to produce a hydrogen plasma lasting at least 26 s in 2018 (more details in ref. [7]). To investigate the behavior of larger scale plasma in high confinement mode (H-mode) that is necessary to achieve the criterion for the fusion process, devices like EAST (Experimental Advanced Superconducting Tokamak) in Hefei, China are build. Here, variations of different first wall and divertor material can be tested. All these experimental results are contributing to the joined project ITER (International Thermonuclear Experimental Reactor) in Cadarache, France. In this device an output power of 500 MW in 400 s pulses is planned. ITER will cover questions on feasibility of fusion power plants including nuclear safety aspects.
This promising path to a future power plant using nuclear fusion as as energy source is driven by the fundamental process taking place in our Sun. Due to its enormous mass of about 332946 times the mass of Earth, in its center extreme conditions of pressure (150 billion bar) and temperature (15 million °C) are present to initiate the proton-proton cycle. Here, two protons (${}^{1}_{1}\mathrm{p}$) are converted into the heavy hydrogen isotope deuterium (${}^{2}_{1}\mathrm{D}$), which involves the conversion of a proton into a neutron (${}^{1}_{0}\mathrm{n}$) including the production of a positron (e^{+}) and a neutrino (ν), as

$$ {}^{1}_{1}\mathrm{p} + {}^{1}_{1}\mathrm{p} \rightarrow {}^{2}_{1}\mathrm{D} + \mathrm{e}^{+} + \boldsymbol{\nu} + 0.42\,\mathrm{MeV} \tag{1.1} $$

followed by the annihilation of the positron into two gamma-ray photons

$$ \mathrm{e}^{+} + \mathrm{e}^{-} \rightarrow 2\boldsymbol{\gamma} + 1.022\,\mathrm{MeV}. \tag{1.2} $$

It is called a cycle because the deuterium atom and another proton are converted into helium (${}^{3}_{2}\mathrm{He}$) and two helium atoms are able to create a new proton. Using this cycle, in addition to various other products, the sun is converting 4 million tonnes of mass into heat and radiation in one second. The goal of the aforementioned fusion experiments is to establish comparable, controlled conditions on Earth. An important indicator for this is the so called Lawson Criterion [8], also referred to as the triple product of density n, temperature T, and confinement time τ_E. In general the energy produced by the fusion process has to exceed all radiation and conduction losses including the efficiency of the energy conversion process. Lawson assumes that a possible fusion reactor contains a plasma with particle positions distributed in a Gaussian curve, and a Maxwell-Boltzmann velocity distribution $\langle v \rangle$ that is indicated by the plasma temperature. The cross section of the fusion process is given as σ.

The energy E_{ch} of charged fusion products, while neutrons cannot heat the plasma, is taken into account to form the triple product as

$$nT\tau_E \geq \frac{12}{E_{ch}} \frac{T^2}{\langle \sigma v \rangle}. \tag{1.3}$$

The easiest way to fulfill the necessary density for a sufficient confinement time of the plasma in magnetic confinement fusion is achieved by the deuterium-tritium (DT) reaction

$$^2_1\mathrm{D} + ^3_1\mathrm{T} \rightarrow ^4_2\mathrm{He}(3.5\,\mathrm{MeV}) + \mathrm{n}(14.1\,\mathrm{MeV}) \tag{1.4}$$

while tritium is produced in a lithium reactor

$$\begin{aligned} ^6_3\mathrm{Li} + \mathrm{n} &\rightarrow ^4_2\mathrm{He} + ^3_1\mathrm{T} + 4.78\,\mathrm{MeV} \\ ^7_3\mathrm{Li} + \mathrm{n} &\rightarrow ^4_2\mathrm{He} + ^3_1\mathrm{T} + ^1_0\mathrm{n} - 2.47\,\mathrm{MeV}. \end{aligned} \tag{1.5}$$

The value of the triple product for this reaction at the temperature $T = 14\,\mathrm{keV}$, where the minimum occurs, is given as

$$nT\tau_E \geq 3 \cdot 10^{21}\,\mathrm{keV\ s/m^3} \tag{1.6}$$

and has not been achieved in all fusion test devices. Nevertheless, it is worth following this path, because of the huge impact a fusion based power plant can have on our energy production. As an example for this it can be calculated that 15 g of deuterium and tritium fuel is sufficient for the energy need of one EU citizen for 80 years.
The achievement of this goal depends on the understanding of all different effects that influences the efficiency and nuclear safety of magnetic confinement devices. Before describing the huge impact of Plasma-Wall Interactions (PWI) and underlining the importance of this work on laser-based diagnostics, a short introduction to the confinement process will be given.
Due to the Lorentz force, a charged particle in a strong magnetic field follows a helical path around linear field lines with a radius of gyration $r_L = v_\perp/\omega_c$. Here, $v_\perp$ describes the particle velocity perpendicular to the field lines and ω_c is given as the angular cyclotron frequency dependent on particle charge q, mass m, and magnetic induction strength B as

$$\omega_c = \frac{q \cdot B}{m}. \tag{1.7}$$

The guiding center moves with a velocity $v_\parallel$ parallel to the field lines. One of the simplest concepts to use these field lines to confine the ions and electrons in a specified volume is a “magnetic bottle” or “magnetic mirror”. This can be pictured as a cylinder with parallel magnetic field lines, where the density of the field lines increases at the edges. The higher magnetic induction strength leads to a increasing force on particles approaching the edges and can cause a movement in the reverse direction. With this conceptional machine only particles that have a sufficient perpendicular velocity can be trapped. Due to this, and because of other instabilities, “leaky” systems like this can not be used to achieve the Lawson

criterion. The solution to this is to use a toroidal shaped device where the two ends of the cylinder are attached to each other. However, a simple toroidal magnetic field would indicate a higher magnetic field line density in the center than at the outer part of the torus. This would lead to a vertical drift of the particles that are supposed to be confined. The results are charge build-ups and plasma losses. To overcome this, a second poloidal magnetic field component is applied to compensate the vertical drift. The two different approaches to an application of this principle were mentioned in the beginning of this section. In the stellarator scheme the necessary magnetic field is obtained by a complex set of magnetic coils around the torus. This concept allows a continuous operation of the plasma confinement in contrast to a pulsed operation in the tokamak. Here, the poloidal magnetic field lines are generated by an induced current inside the confined plasma itself. This is achieved by an inductively induced current using a transformer like scheme. This current is also used to heat the plasma due to its conductivity. Additional vertical field coils are necessary to resist expansion forces of the plasma-current.
Considering this basic description of the confinement process in a tokamak or a stellarator, among others, one of the main challenges is to control the fuel content (deuterium and tritium) and the amount of impurities e.g. helium ash and removed wall materials to minimize radiation and conduction losses. During different operation modes of the plasma it appears that the so called first wall or other Plasma-Facing Components (PFC) interact with the confined plasma. From a safety point of view, the steady accumulation of tritium to the plasma-facing material can not be tolerated. To overcome this, the material of the first wall has been changed from carbon to tungsten and tungsten based alloys. Although carbon is a good heat conductor, does not melt in the mentioned conditions, and has a high sublimation temperature, it appears that the erosion level with hydrogen is high due to the formed hydrocarbon compounds (see without limitation ref. [9]–[11]).
As noted from the safety point of view, any steady deposition of hydrogen isotopes to the plasma-facing materials need to be quantified. For this purpose a laser-induced diagnostic approach is proposed by Huber et al. in ref. [12]. Here, an *in-situ* approach, e.g. during the low confinement mode of the plasma operation, using Optical Emission Spectroscopy (OES) of a laser-induced plasma at the inner wall can be used to examine the fuel content in PFCs. This technology is called Laser-Induced Breakdown Spectroscopy (LIBS) and is described in the following section. However, this thesis is focused on the investigation of PFCs using different kind of laser pulses in a wide range of pulse duration and wavelengths outside the fusion plasma vessel.

Laser-Induced Breakdown Spectroscopy

The development of Light Amplification by Stimulated Emission of Radiation (LASER) opened a wide field of applications using coherent light sources. Particularly the invention of the first pulsed laser in 1960 creates the opportunity to generate high intensity laser pulses that are able to initiate a plasma. Time resolved OES of these plasmas enabled the opportu-

nity to analyze chemical and physical material composition. A spectro-chemical analysis of the breakdown in air was performed in 1962 (ref. [13]), which is the basic process of Laser-Induced Breakdown Spectroscopy (LIBS). Now, LIBS is used as a variant tool for hands-off material and environment analysis. Famous examples are the use of LIBS on the Mars Science Laboratory (MSL) Curiosity rover to analyze soils, rocks, and possible hydrogen compounds on Mars surface described in ref. [14], a machine learning supported approach to recognize cancer in tissues in ref. [15], interesting applications in waste separation in ref. [16], and the *in-situ* application of LIBS in the context of nuclear security. Here, different fields are of interest, for example the on-line monitoring isotopic analysis of fission products investigated in ref. [17] or the already mentioned *in-situ* diagnostic of plasma-facing components in fusion devices.

The experiments shown in this thesis will cover the analysis of relevant material for magnetic confinement fusion devices using various laser systems. Here, the experiments are executed with lasers of different pulse duration, wavelength, and in varying environments. The results are discussed with regard to the basic physical processes, and the applicability in the context mentioned above covering different advantages and disadvantages of the lasers used. Special attention is given to the use of ultra-short laser pulses with pulse durations in the range of a few picoseconds to sub-10-fs as the driving laser sources for the laser ablation process. Since the invention of Chirped Pulse Amplification (CPA) by the 2018 Nobel prize winners Donna Strickland and Gérard Mourou (1985, ref. [18]) these ultra-short pulses can gain enough energy for laser processing and plasma generation to be possible. Shorter pulses have the big advantage compared to nanosecond and longer pulse duration that the heat impact to the system is much lower, which results in a highly accurate ablation region. This high accuracy can be used to establish a diagnostic scheme with a high depth resolution on the order of the optical penetration depth ($\sim 10\,\mathrm{nm}$, depending on laser wavelength and material properties). In ref. [19] for example, material composition could be analyzed with a depth resolution of 7 nm on a silicon (Si) based substrate. This was established with a frequency tripled ($\lambda = 343\,\mathrm{nm}$) diode pumped Ytterbium laser with 500 fs pulse duration, which is also used in one of the experiments presented in this thesis.

Research Objective

The described technique LIBS has already been tested inside of fusion devices with lasers of pulse duration of a few nanoseconds. See for example the findings in ref. [20] and [21], where LIBS is performed on inner walls of EAST. Despite the advantages of a nanosecond laser-induced plasma with regard to the size, life-time, and brightness of the source, a big drawback appears in the quantification of stored minor elements, particularly in a depth resolved analysis. The high thermal impact of nanosecond lasers to the investigated sample can lead to desorption of stored light elements from the whole material bulk. This Heat Affected Zone (HAZ) decreases the accuracy of the analyses of deposited material, and the stored fuel in form of the heavier hydrogen isotopes deuterium and tritium. Apparently,

lasers of lower pulse duration in the range of picoseconds to femtoseconds appear to have a significant lower thermal impact in the interaction region and ablated craters exhibit higher accuracy [22]. From this point of view, a femtosecond system can be a major benefit for the field in the diagnosis of depth resolved fuel retention. Now, the purpose of this work is to demonstrate applicability and limitations of LIBS with femtosecond lasers to achieve high lateral and depth resolution for the detection of hydrogen isotopes in typical PFC materials by presenting a collection of novel experiments.

These experiments include an intensive study on the laser-induced ablation characteristics on tantalum with three different laser sources covering a wide range of pulse duration in chapter 4. The high-Z metal tantalum can be seen as a surrogate to investigate the influence of the different lasers on typical PFCs, which are usually made from tungsten and tantalum based alloys. This study will be followed by more detailed investigations of the laser-induced plasma by an ultra-short sub-10-fs laser in a vacuum environment and an approach to enhance the optical emission spectra using a pre-pulse configuration in chapter 5. Note that it is a novel approach to perform OES on plasmas induced by laser pulses of this short pulse duration. With their high possible intensity, usually those pulses are used to enable high-harmonic generation, particle acceleration, or are able to initiate characteristic x-rays by inner shell excitation. This thesis will give a classification of laser intensities reasonable for the aspired application with the ultra-short pulses used.

In chapter 6, proof-of-principle experiments on hydrogen isotopic analysis will be shown with two different lasers exhibiting pulse duration of nanosecond and femtosecond. Here, a quantitative approach is included to determine the total amount of deuterium retention in the investigated tungsten tiles. The underlying fundamental physical concepts that are necessary to understand the experiments will be explained in chapter 2, and the used methodologies and instruments are described in chapter 3. This work will conclude by giving an evaluation to the initial question, whether femtosecond LIBS is a suitable diagnostic technique to analyze the fuel content in plasma-facing components with the scope to use it *in-situ* at an actual magnetic confinement fusion experiment or even at an upcoming power plant to ensure a safe operation of the facility.

Chapter 2

Theoretical Background

To be able to interpret the findings presented in this thesis, a number of fundamental descriptions need to be understood. From the laser beam alignment and preservation of optical properties over the laser-material interaction itself to the plasma expansion process, a couple of models and concepts will be explained in this chapter. Its purpose is to give a detailed overview of the powerful diagnostic technique LIBS, which is used as an all-optical tool to analyze the composition of PFCs. The description of short and ultra-short laser pulse propagation in the first part will be followed by the conceptual explanations of laser ablation and plasma expansion in the second part.

2.1 Short and Ultra-Short Laser Pulses

In the following, the concepts of laser geometry and propagation are explained showing spatial and temporal changes. The description focuses on characteristics of Gaussian and Super-Gaussian beam-profiles in the first part, and dispersion effects of ultra-short broadband laser pulses in the second section part of this section. All concepts are supplemented by actual measurements from the used lasers in this work. For more technical details on the generation processes of the different used lasers refer to chapter 3.1.

2.1.1 Laser Beam Geometry

The propagation of a laser beam in a homogeneous medium (e.g. air or vacuum) is mainly influenced by the beam divergence. This characterizes how the beam radius expands far from the beam waist. In general, collimated beams with a very small divergence (approximately constant beam radius over an appropriate distance) are used to guide the beam to the experiment where a focussing optic (e.g. dispersive lenses or spherical mirrors) changes the divergence. These optics ensure to bundle the light on small areas to achieve necessary intensities or fluences for different experiments. Due to different production processes, different lasers exhibit different spatial profiles. In the following, the laser beam geometry characteristics for Gaussian and flat-top profiles are described based on reasonable measurements.

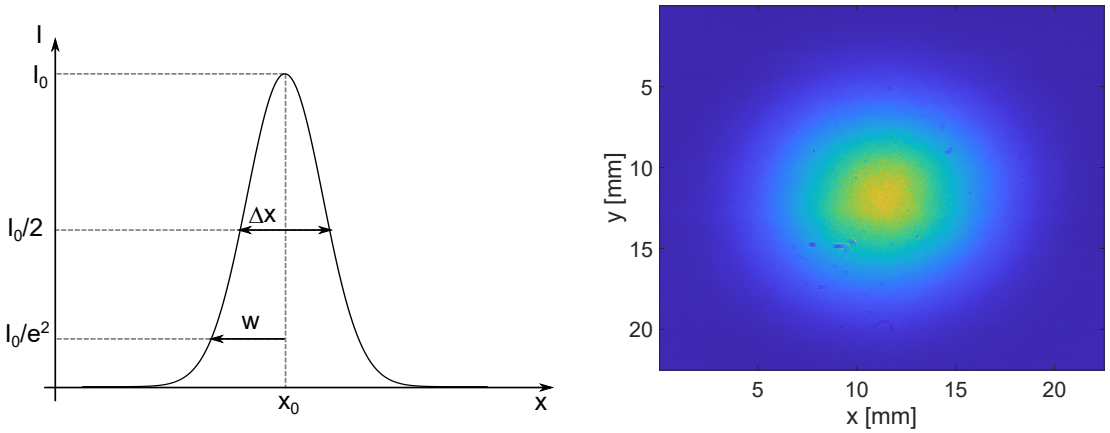

(a) (b)

Figure 2.1: (a) Generic beam profile of amplitude I_0 around the spatial coordinate x_0 including the Gaussian width w and FWHM Δx. (b) Corresponding beam profile measurement of the Ti:Sa laser in front of the beam expansion telescope and the focussing mirror.

Gaussian Beam Profile

In the case of a laser beam that has a Gaussian like shaped transversal profile the intensity is given as

$$I = I_0 \cdot \exp\left[-2\left(\frac{x - x_0}{w}\right)^2\right] \tag{2.1}$$

where w is given as the half width at $1/e^2$ of the maximum intensity value I_0. It also corresponds to the Gaussian width of the electric field, due to the fact that the intensity is proportional to the squared electric field component. Here, the definition of the beam diameter $D_0 = 2w$ can be given. Within an area defined by the diameter D_0, 86.5 % of the laser energy is included. Sometimes the diameter is also defined by $D = 4w$ that includes 99.9 % of the energy. Another characteristic magnitude to describe the beam size is the FWHM (full width at half maximum) of the electric field and intensity respectively which are given as

$$\Delta x_E = 2\sqrt{\ln 2} \cdot w \quad \text{and} \quad \Delta x_I = \sqrt{2 \ln 2} \cdot w. \tag{2.2}$$

In fig. 2.1 the beam profile of a Gaussian shaped laser beam is presented by a typical measurement and a corresponding transversal amplitude distribution perpendicular to the direction of propagation is shown.

Another important point to observe is the beam diameter dependence on the position along the optical axis z when it is focused. The characteristics of a focused beam are shown in fig. 2.2. Here, the half beam diameter $w(z)$ is given as

$$w(z) = w_0 \cdot \sqrt{1 + \left(\frac{z}{z_R}\right)^2} \tag{2.3}$$

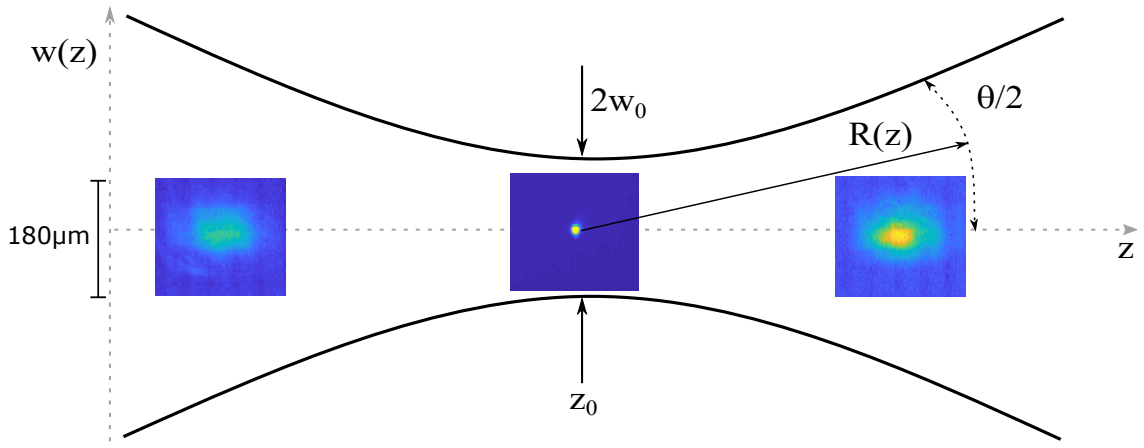

Figure 2.2: Representation of beam diameter dependence on position z behind the focussing mirror of a Gaussian laser beam. Here, the beam profile measurements of the Ti:Sa laser with an initial beam diameter $4w = 25\,\text{mm}$ focussed by a 90°-off axis parabolic mirror with 127 mm focal length at three different positions are shown. Here, the profiler positions (left) $z - z_0 = -960\,\mu\text{m}$, (middle) $z = z_0$ and (right) $z - z_0 = 990\,\mu\text{m}$ are used.

including the beam waist parameter w_0 and the Rayleigh-length z_R. The beam waist parameter of a diffraction-limited Gaussian beam depends on the focal length f, wavelength λ and the size of the incoming beam $A = 4w$ as

$$w_0 \geq \frac{4\lambda f}{\pi A}. \tag{2.4}$$

The Rayleigh-length

$$z_R = \frac{\pi \cdot w_0^2}{\lambda} \tag{2.5}$$

is the distance between the focal spot and the position where the beam radius is given as $\sqrt{2}w_0$.
At focal distances of $z \gg z_R$, equation (2.3) approaches linearly and the divergence of the beam can be defined by the angle $\Theta = 2 \cdot \lambda/(\pi w_0)$. The parallel phase front in the focal spot is curved at this distances by the radius of curvature

$$R(z) = z \cdot \left[1 + \left(\frac{\pi w_0^2}{\lambda z}\right)^2\right]. \tag{2.6}$$

Important laser parameters that can be extracted from the used beam profile are fluence and intensity as these are indicators of e.g. ablation and damage thresholds and are used to set limits in descriptions of absorption and acceleration processes. It is crucial to be defined properly to interpret the upcoming experimental results. The fluence is given as pulse energy E per area $\pi(D/2)^2$.

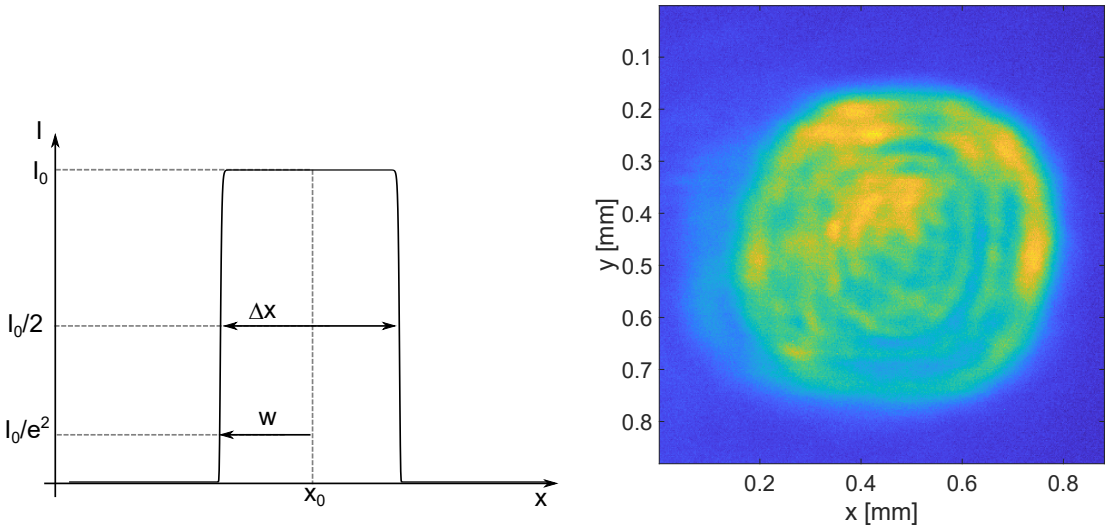

(a) (b)

Figure 2.3: (a) Schematic super-Gaussian beam profile declared as flat-top beam. (b) Beam profile of a picosecond laser (*EKSPLA PL2241*) used in various experiments in this work. The close to flat-top beam is focussed by a N-BK7 plano-convex lens of $f = 50\,\text{cm}$ focal length and the measurement is made $z - z_0 = 2\,\text{cm}$ out of focal plane.

In general, the laser fluence F is driven from an integral over the whole beam area and is approximately given as

$$F = \frac{8E}{\pi D^2} \cdot \cos\theta, \tag{2.7}$$

where $D = 2 \cdot w$ is the beam diameter at $1/e^2$ of the maximum intensity in the interaction plane and θ the angle of incidence, which increases the beam profile in one dimension. A factor 2 is included here to take into account that a Gaussian shaped beam profile covers a smaller effective area than a flat-top beam. The laser intensity I is then given as the fluence per pulse duration $\Delta\tau$. An important note is that the fluence is an integrated quantity, which gives a measure of the total effect induced by one laser pulse, while the intensity describes momentary effects as it is a temporal quantity.

Flat-Top Beam Profile

A flat-top or top-hat beam profile exhibits a flat intensity profile over most of the profile area. Usually the flat-top beam profile can be approximated by a super-Gaussian distribution of the order $n > 2$ as

$$I = I_0 \cdot \exp\left[-2\left(\frac{x - x_0}{w}\right)^n\right]. \tag{2.8}$$

Here, the pulse energy is equally distributed over the whole interaction region, which decreases the heat affection zone. Also different cutting processes can be more efficient with a flat-top beam due to steeper edges of the formed craters. A disadvantage is the dependence of the beam quality factor M^2 on the super-Gaussian order n. Meaning, the more rectangular

shaped the profile is, the worse is the beam quality in the focal spot. One laser in the described experiments uses a flat-top profile, which is shown in fig. 2.3. As mentioned before, the corresponding fluence is given by dividing equation (2.7) by the factor 2.

2.1.2 Pulse Propagation

In general the linear polarized electric field E of an ultra-short wave package is described as its real part

$$E(t) = E_A(t) \cdot \cos\left(\omega_0 t + \phi(t)\right) \tag{2.9}$$

that consists of the envelope electric field E_A and the oscillating carrier wave at central angular frequency ω_0 and the time dependent phase $\phi(t)$. The envelope can be Gaussian like, described by its amplitude E_0 and pulse duration $\Delta\tau$ as

$$E_A(t) = E_0 \cdot e^{-2\ln 2(t/\Delta\tau)^2}. \tag{2.10}$$

The pulse duration $\Delta\tau$ is defined as the FWHM of the intensity profile in the time domain. Note that the intensity is proportional to $E(t)^2$. As an ultra-short laser pulse is composed of many spectral components, the electric field in the frequency domain can be calculated by an inverse fourier transformation of the complex electric field $\tilde{E}(t)$ according to

$$\tilde{E}(\omega) = \frac{1}{\sqrt{2\pi}} \int_{-\infty}^{\infty} \tilde{E}(t) \cdot e^{-i\omega t} \mathrm{d}t. \tag{2.11}$$

Here $\tilde{E}(\omega)$ is the complex spectral electric field which is described by the spectral phase $\phi(\omega)$ as

$$\tilde{E}(\omega) = E_A(\omega) \cdot e^{i\phi(\omega)}. \tag{2.12}$$

Observing ideal Gaussian shaped laser pulses with a constant phase, the time bandwidth product is given as $\Delta\tau \cdot \Delta\nu = 0.441$ where $\Delta\nu$ is the angular frequency bandwidth $\Delta\omega$ divided by 2π. The addition of any non-linear phase component increases this product and pulse duration and shape are changing.

Dispersion-Effects

The description of pulse propagation is given by the rise of the spectral phase

$$\phi(\omega) = \frac{x}{c} \cdot \omega \cdot n(\omega). \tag{2.13}$$

A Taylor-Expansion of the spectral phase

$$\phi(\omega) = \sum_{m=0}^{\infty} \frac{(\omega - \omega_0)^2}{m!} \cdot D_m, \tag{2.14}$$

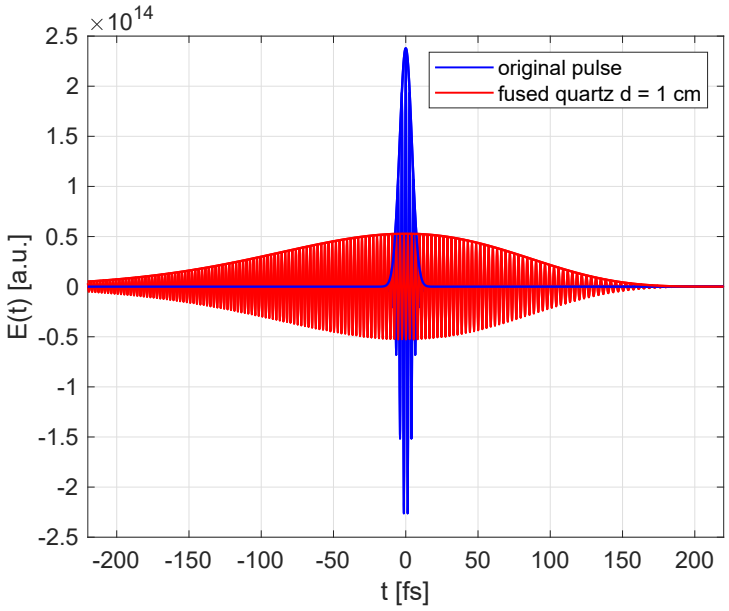

Figure 2.4: Comparison of the original (blue) 7 fs laser pulse and a pulse after a 1 cm thick fused quartz window (red). Here, the envelope and the carrier wave are shown.

with

$$D_m = \left(\frac{\partial^m \phi(\omega)}{\partial \omega^m} \right)_{\omega=\omega_0}, \tag{2.15}$$

provides dispersion coefficients D_m that gives an idea of the temporal pulse shape after the dispersion. Here, D_0 describes the linear progression of the phase, D_1 of the pulse itself and D_2 is a measure for the pulse duration extension. Higher order dispersions ($m > 2$) describe asymmetric pulse deformations and higher order effects that compensation is limited by common optical compressor configuration.

To get an idea of the actual temporal pulse shape, the spectral phase calculated from equation (2.13) is added using (2.10) to the spectrum. Afterwards a fourier transformation is performed. In fig. 2.4 the resulting pulse broadening for a 7 fs pulse is shown after propagation through 1 cm of fused quartz. As an approximation for perfectly Gaussian shaped pulses

$$\Delta\tau = \Delta\tau(0) \cdot \sqrt{1 + \left(4 \cdot \ln 2 \cdot \frac{D_2}{(\Delta\tau(0))^2} \right)^2} \tag{2.16}$$

can be consulted to calculate the broadened duration $\Delta\tau$ for an initial duration $\Delta\tau(0)$. With $D_2 = 361\,\text{fs}^2$ for 1 cm of fused quartz the pulse is broadened to $\Delta\tau = 143\,\text{fs}$. During laser operation in praxis, the spectral phase changes due to reflectance and transmission on different optical elements like chirped mirrors and beamsplitters that need to be considered. To overcome and control all spectral changes it is necessary to have a look at the provided Group Delay Dispersion (GDD) data determined for the purchased optic. The influence of a given GDD is discussed with respect to the Phaser-stabilized Heine Laser (PHASER) spectrum in the following section.

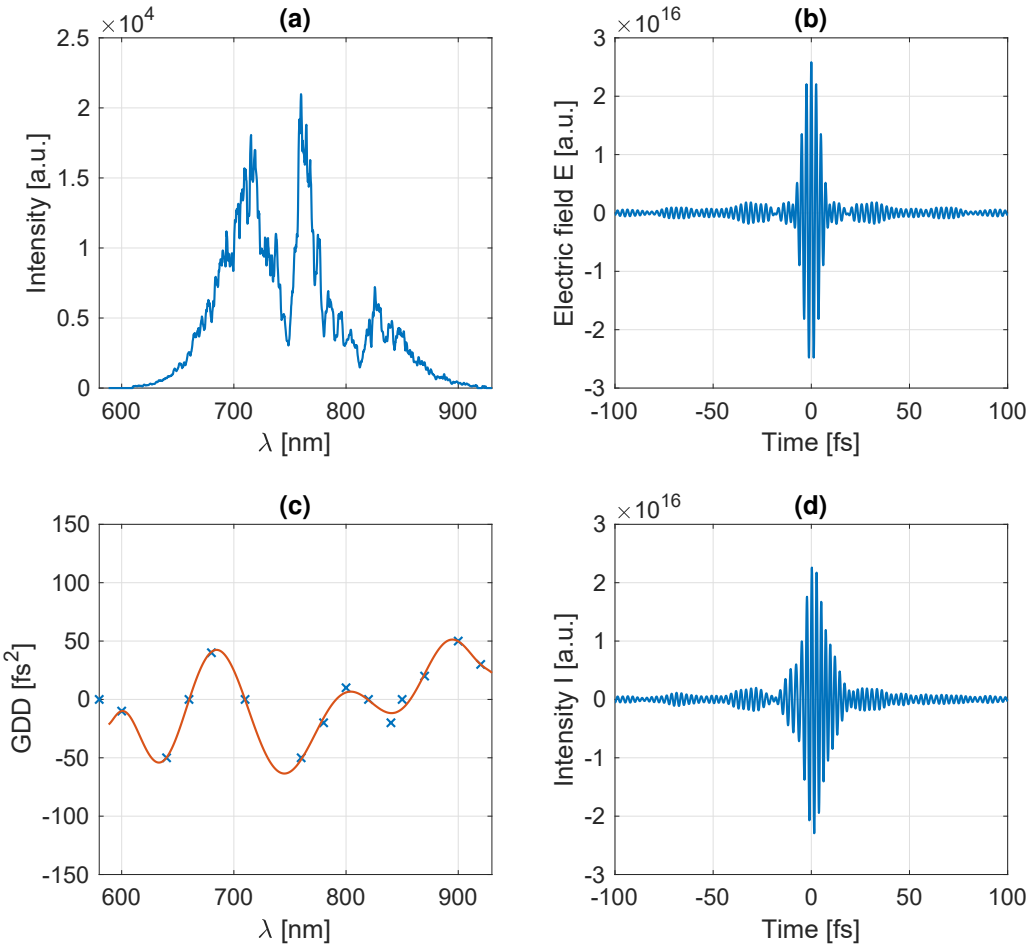

Figure 2.5: (a): Measurement of broadband femtosecond lasers fundamental spectrum. (b): Calculated electric field in the time domain. (c): Fitted GDD curve on discrete data points of a *Layertec* beamsplitter for s-polarized lasers. (d): The effect on the electric field in the time domain.

Influence on Broadband Spectrum

From the measured fundamental spectrum of the PHASER, described in chapter 3.1.1, a spectral bandwidth of 300 nm can be observed. In fig. 2.5 (a) and (b) the measured spectrum and the calculated electric field in the time domain are shown. The pulse shape is given under the condition of an initial spectral phase of $\phi(\omega) = 0$. From the mentioned GDD data the new pulse shape can be calculated. To demonstrate this an example GDD curve is given for the reflected part of a beamsplitter in fig. 2.5 (c) and (d). The shown GDD graph is integrated two times to see the effect on the spectral phase. Phase modulations of different orders can be observed. D_0 and D_1 components that are responsible for phase and pulse propagation can be ignored while the impact of D_2 can be compensated. The shape of the pulse in the early part ($t < 0$) results from higher order dispersion coefficients are harder to compensate.

It has been shown that ultra-short laser pulses have to be treated with care, when the high intensity obtained by the short pulse duration needs to be conserved. Moreover, shaping the laser pulse by optics of well identified dispersion relations is possible and can be used to study physical effects depending on pulse duration by constant spatial and spectral pulse properties for example in the context of LIBS.

2.2 Laser-Induced Breakdown Spectroscopy (LIBS)

This section gives an overview of processes that are involved in LIBS. These are mainly the laser-induced ablation, plasma expansion into the environment, and the optical breakdown. The main concept of LIBS makes use of the de-excitation of atoms and ions in a laser-induced plasma phase. Resulting spectra can be detected with optical spectrometers and high speed cameras (see chapter 3.3). The observed de-excitation can then be projected to the material and impurity composition and therefore used to analyze the Plasma-Facing Components (PFCs) of a fusion reactor that are observed in this work. The methods to extract physical properties of the expanding plasma from the measured spectra are discussed in chapter 3.4. Hereafter, the depicted fundamental processes in fig. 2.6 of laser surface interaction are described from the laser absorption and ablation process (a) to (c), plasma expansion characteristics (d), (e) and typical post plasma cluster production and re-solidification (f). Note that typical timescales are given here, when it comes to femtosecond laser irradiation.

2.2.1 Ultra-fast Laser Ablation

In literature on laser solid ablation one finds approaches to describe the interaction in different laser pulse intensity regimes. With the lasers used in this work intensities up to $10^{18}\,\mathrm{Wcm^{-2}}$ are possible. Anyway, the most important observations in LIBS applications are made with intensities I that are way lower (10^{12} to $10^{14}\,\mathrm{Wcm^{-2}}$) on the way to achieve a low ablation rate resulting in a high depth resolution. Below, this regime is referred to as the moderate intensity regime, while $I < 10^{12}\,\mathrm{Wcm^{-2}}$ is assigned as the low- and $I > 10^{14}\,\mathrm{Wcm^{-2}}$ as high regime respectively. Note that in all described processes and concepts there are no such strict boundaries as this classification might imply, in particular when characteristics of laser ablation on materials with different conductive properties are observed. In the following text, the description is divided into intensity dependent absorption mechanisms and the ablation process itself.

Laser Absorption

Absorption of the laser energy, depicted in fig. 2.6 (a) and (b), is the first step of the laser-induced plasma diagnostic LIBS. Ramping up the laser intensity changes the characteristics of the absorption process. Here, the description is limited to conductive materials like copper, aluminum and other metals. In the low intensity regime absorption is dominated by electron-phonon collisions, while in the moderate and high intensity regime the interaction

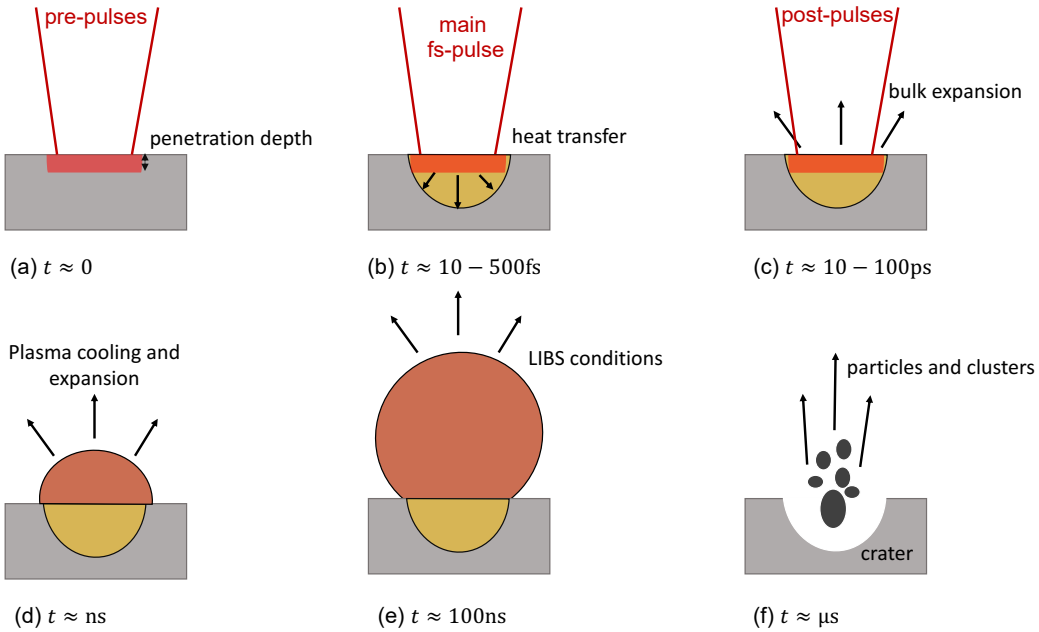

Figure 2.6: Schematic view on the plasma formation induced by femtosecond laser on conductive samples including typical timescales and basic descriptions of the fundamental processes.

with a pre-plasma is getting more relevant. Some publications like ref. [23] are mentioning this as the Coulomb dominated plasma collision regime. In general, there is always a mix of different absorption processes, as the laser intensity can vary temporally and spatially. The absorption efficiency depends on the material properties or the surface near plasma characteristics. Whether a plasma is created and which parameters are crucial for the absorption mechanism depends on the laser intensity.
In the moderate intensity regime, most likely collisional effects dominate the absorption process. In this context, the concepts of the skin-effect and inverse Bremsstrahlung need to be discussed.

Skin-Effect: The unperturbed electron-lattice subsystem of the metal can be described as a step-like plasma of overcritical density. Here, the electric field amplitude in this plasma declines exponentially from the surface into the bulk according to the Lambert-Beer law with a skin depth at $1/e$ of the amplitude of $L = \lambda(2\pi k)^{-1}$. Here, λ is the laser wavelength and k the imaginary part of the refractive index. The absorption of the laser energy in the bulk can be described by the Drude-Lorentz formalism and reflectivity and absorption fraction are calculated consulting the Fresnel equations (see appendix A). With a higher laser intensity and resulting higher electron temperature given, the normal skin-effect evolves to the anomalous skin-effect, while conductivity of the material changes and the mean free path of electrons rise. The energy can be transported farther into the material and the skin-depth rises.

Inverse Bremsstrahlung: One of the first description of this absorption process is given in ref. [24]. This three-body concept involves a photon, an electron and a third part, for example another bound electron or a surrounding atom and is the inverse process to Bremsstrahlung, where a decelerated electron emits a photon perpendicular to the propagation direction. Electrons released from the surface start to oscillate and induce collisions with bound electrons due to the laser field influence. To release the electrons, the ionization threshold (e.g. 7.0 eV for copper) has to be overcome by multiphoton ionization (photon energy of near Infra-Red (IR) laser: 1.55 eV). Different theoretical and experimental studies like ref. [23], [25], and [26] show evidence for collisional absorption to be the dominant process for these intensities. In contrast to the normal skin-effect, for the process described a longer plasma gradient is necessary, which was created by a pre-pulse or the early weaker part of the laser pulse.

The electron-ion collision frequency ν_{ei} in the plasma is given for a total number N of free electrons, electron number density n_e [cm^{-3}], temperature T_e[eV] and the Coulomb logarithm $\log\Lambda$ as

$$\nu_{ei}\ [\mathrm{s}^{-1}] \approx 3 \times 10^{-6} N n_e T_e^{-3/2} \log\Lambda. \tag{2.17}$$

With a higher electron temperature, the collision frequency decreases and collisional absorption processes does no longer influence the laser plasma interaction. In conclusion, at higher intensities the influence of collisional absorption gets weaker and direct (collisionless) absorption becomes the dominant process. Gibbon and Förster (1996, ref. [27]) give an overview of possible processes that are involved in the absorption at high laser intensities. In this regime the absorption is governed by the scale length of the pre-plasma, which had limited time to expand, because it was created by the early pulse edge. Note that lasers of pulse duration in the femtosecond region and especially sub-10-fs laser pulses with a high contrast ratio exhibit early stage expansions that lead to plasma scale lengths of $\sim 0.01\lambda$ as shown by Cerchez et al. (2008, ref. [28]). In this regime, Resonance Absorption and Brunel-Heating might be the best described and approved concepts of laser-plasma coupling.

Resonance Absorption is the process mainly discussed in this context. A p-polarized light wave can tunnel through the critical surface in the pre-plasma in front of the target where $n_e = n_c$. The critical density n_c is given dependent on the laser frequency ω, permittivity ϵ_0, electron mass m_e and charge e as

$$n_c = \frac{\omega^2 \epsilon_0 m_e}{e^2}. \tag{2.18}$$

The penetrating light drives a plasma wave that is either damped or even breaks at high laser intensities. During the damping induced by collisions or particle trapping, energy is transferred to the electron subsystem in the overcritical part. It can be shown that for a long scale length L, the absorption rate depends on the wavevector $k_0 = 2\pi/\lambda$ and the angle of incidence θ as $(k_0 L)^{2/3} \sin^2\theta$, which is independent of the mechanism that forces the wave damping.
In another description the resonance breaks down under the condition that the driven wave

amplitude exceeds the plasma scale length. In this case, the description by Brunel (1987, ref. [29]) can be followed.

Brunel-Heating: In the proposed process, the electrons in the plasma are pulled away from the surface and accelerated back to it with weakly relativistic velocities in half a cycle of the laser field. The absorbed fraction of the incoming laser pulse energy is proportional to the gained velocity of the electrons in the aforementioned sub-cycle. Brunel refers to this as the quiver velocity.

Summing up, collisionless processes would be more efficient then collisional absorption. This and further effects during the ablation process can be the reason for different fluence dependent ablation regimes with varying ablation rates as for example observed in ref. [30]. The absorbed energy in the solid or plasma leads to disintegration of the former solid lattice structure and transfers into an adiabatic expanding plasma due to high pressure inside of the bulk. All in all, the material is ablated from the surface and a crater is formed. In the following section, different ablation processes are described that characteristics depend on the absorbed laser energy.

Laser Ablation

Different numerical and experimental studies showed the impact of laser pulse intensity on the laser ablation process in metals (among others ref. [30]–[32]). Following those, in the moderate intensity regime, the energy absorbed can be expressed by the initial laser intensity acting on the surface $I(t)$, the reflectivity R and the material dependent optical absorption coefficient α as

$$S(r,z,t) = (1-R)\cdot\alpha\cdot I(r,t)\exp\left(-\alpha z\right) \tag{2.19}$$

on a spot with radius r and in depth z behind the surface. In general, the laser is able to heat the electron subsystem, which subsequently collides with the ensuing lattice system and transfers the heat to it. This transfer can be described in a Two-Temperature Model (TTM) of electron and lattice temperature T_e and T_l by the coupled differential equations

$$\begin{aligned} C_e\frac{\partial T_e}{\partial t} &= \nabla\left(\kappa_{el}\nabla T_e\right) - G\cdot(T_e - T_l) + S(r,z,t), \\ C_l\frac{\partial T_l}{\partial t} &= G\cdot(T_e - T_l), \end{aligned} \tag{2.20}$$

including the electron and lattice heat capacity C_e and C_l, electron thermal conductivity κ_{el} and the coupling parameter G. Note that these thermophysical quantities depend on T_e and T_l as described in the appendix A. Here, the basic algorithm of such a simulation is described as well. In the case of laser ablation with a laser of pulse duration $\Delta\tau$ longer than picoseconds, the duration is on the order of the typical electron-phonon interaction time τ_{eph}. In this case the classical heat diffusion equation is sufficient and the thermal penetration depth $L_{th} = 2\left(\kappa\Delta\tau\right)^{1/2}$ is the dominant value to evaluate the excited volume. Here, κ is

the heat conductivity. Apparently this concept fails when the heating process is over, way before the electron and lattice subsystems are balanced. This occurs when the heating is executed by a femtosecond laser. With a moderate intensity, the affected zone behind the surface can be reduced to the volume of the wavelength dependent optical penetration depth $L_{opt} = \alpha(\lambda)^{-1}$, which is the same value as the skin depth of the normal skin-effect. This can lead to a higher depth resolution, as the Heat Affected Zone (HAZ) is reduced or even avoided with femtosecond lasers, because $L_{th} \gg L_{opt}$.

Heating the lattice causes a phase transition that shows different characteristics depending on the laser fluence and pulse duration. With high laser intensities above the ablation threshold for solids, it is likely that a huge amount of electrons in the skin depth is removed and a large space charge zone arises. Also in conductors or metals this zone can not be completely filled by conduction band electrons, which results in a high electrostatic force that accelerates the leftover ions from the lattice. This process is called Coulomb explosion and is assumed in many publications as the dominant ablation mechanism (see ref. [33] or [34]). In ref. [35] the authors emphasize that Coulomb explosion can be observed for metals under extreme intensities around $10^{19}\,\mathrm{Wcm}^{-2}$, while for semiconductors a way lower intensity limit can be possible as $I \geq 10^{14}\,\mathrm{Wcm}^{-2}$. This implies that Coulomb explosion might not be the main ablation process to be observe in the experiments presented, as the intensity remains below the limit for metals almost all the time. As a short side note to this: Interesting results from Tamaki et al. (2022, ref. [36]) gave evidence for the influence of Coulomb explosion using Carrier-Envelope Phase (CEP) change diagnostic of THz-emission in a pump-probe experiment. It might be interesting to give these findings some thoughts in observations made with the PHASER system.

Another model that is used is the phase transition as a thermal process. Here, the lattice literally melts under the high temperature gained, which has to happen on a picosecond timescale, according to ref. [37]. The limiting process is the electron-lattice relaxation time. Moreover, it is also possible that the high energetic electrons are able to change the potential of the lattice structure, which initiates bond breaking due to the resulting forces. This melting process can even be observed when the lattice is still at room temperature and is called non-thermal melting (see ref. [38]). Recent simulation studies from 2021 by Ye et al. (ref. [39]) show a decreasing melting point for tungsten under high electron temperature influence. The phase transition might not be homogeneous in the whole heated region behind the surface, and a mixture of liquid and vapor is created. This can lead to internal stresses followed by a phase-explosion, also called explosive boiling, resulting in a collective ablation of clusters and liquid droplets. See the numerical approach in ref. [40] for fluences close to the ablation threshold of metals.

As a last remark to this, the ablation process in the moderate intensity regime defined here, can be explained by Critical-Point Phase Separation (CPPS). Hydrodynamic models, as used in ref. [41], suggest this to be the dominant process for intensities around $10^{14}\,\mathrm{Wcm}^{-2}$. Wu et al. (2007, ref. [42]) presented a simple model based on this process to evaluate the ablation threshold fluence from a commonly used TTM simulation. As described here, and in other

references like ref. [43], the thermodynamic trajectory in the phase diagram $\rho - T$ is observed. A fast temperature gain way beyond the critical point without a significant material density ρ change can be assumed, while the separation temperature T_{sep} might be estimated from the following adiabatic trajectory where $T \propto \rho^{2/3}$. With this assumption ablation occurs when the lattice subsystem reaches a temperature of

$$T_{sep} = T_c \cdot \left(\frac{\rho_0}{\rho_c}\right)^{2/3}. \tag{2.21}$$

Here the critical temperature and density are given as T_c and ρ_c respectively and the initial density as ρ_0.
To close this section, I want to come back to the schematic view of the whole LIBS process in fig. 2.6. After the laser absorption in (a) and (b) and the ablation (c), the plasma expands to the ambient environment (d), which can be described by hydrodynamic approaches. In many cases, like in ref. [44], an adiabatic cooling is assumed. All this might happen in the first nanoseconds after the laser plasma interaction. In this description, the later stages of the plasma (e) are described in the next section. Another characteristic of femtosecond laser ablation is the separation of clusters (f), mainly observed in isolators or semi-conductors, but also in metals of high atomic number Z. It results from the creation of overheated vapor bubbles in the material. These clusters and other heavy particles usually turn up later after the LIBS conditions are fulfilled. In the end the remaining particles re-solidify and a crater is formed.

2.2.2 Plasma Expansion

The central point of LIBS is to observe the characteristic spectrum of the expanding plasma. The following section gives an overview of the basic description of this state of matter and shows which physical parameters can be extracted from the optical observation.
In a laser-induced plasma, ions, electrons and neutrals form a plume that expands perpendicularly from the solid surface into the ambient atmosphere (or vacuum). According to the varying temperature and number density of the different species in this plume, different processes occur that lead to radiation. Simultaneously characteristic processes like photoionization, collisional ionization, radiative and three-body recombination, collisional excitation and de-excitation, photoexcitation and de-excitation, and Bremsstrahlung take place in a small volume. In accordance with this, the description of such a plasma can be complex without some assumptions to the thermodynamic conditions. In the following paragraphs a thermodynamic description of a plasma in general is given including assumptions that are necessary to apply to a Laser-Induced Plasma (LIP).

Thermodynamic Equlibrium (TE)

If a plasma appears to be in a Thermodynamic Equilibrium (TE), all the processes of excitation and de-excitation mentioned are balanced equally and the description by one over-

all temperature is given by the well-known distribution laws from Planck, Boltzmann and Maxwell. For two atomic or ionic energy levels the population of upper (N_2) and lower (N_1) state, the Boltzmann distribution

$$N_2 = N_1 \frac{g_2}{g_1} \exp\left(-\frac{\Delta E}{k_B T_{exc}}\right) \tag{2.22}$$

including the statistical weights g_1, and g_2, excitation temperature T_{exc}, Boltzmann constant k_B and energy difference ΔE is given. Moreover, the velocity of a species with mass m, kinetic temperature T and average velocity v in the plasma is described by the Maxwellian velocity distribution depending on population density n as

$$f(v) = n \left(\frac{m}{2\pi k_B T}\right)^{3/2} \exp\left(-\frac{m v^2}{2 k_B T}\right). \tag{2.23}$$

While this temperature is equal for all species in a TE, a more complex description is necessary for a laser-induced plasma with varying temperature of electrons T_e and heavy particles like atoms and ions. Note that even the temperature of different atoms and ions can vary in such a case. The population density of atoms and ions in a TE is basically described by the Saha equation. As a simple example in a system of a neutral atom and an ion of first ionization degree it is given as

$$\frac{n_e n_{A+}}{n_A} = \frac{2 U_{A+}(T)}{U_A(T)} \left(\frac{m_e k_B T_i}{2\pi\hbar^2}\right)^{3/2} \exp\left(-\frac{E_\infty - \Delta E}{k_B T_i}\right) \tag{2.24}$$

with population densities of the electron n_e, ion n_{A+} and neutral atom n_A and ionization energy E_∞ with a plasma correction factor ΔE depending on among others the number density according to micro-field fluctuations on the scale of the Debye length λ_D. According to ref. [45], it can be approximated (in eV) by the Debye shielding effect as

$$\Delta E = 3 \times 10^{-8} Z \left(\frac{n_e\,[\mathrm{cm}^{-3}]}{T\,[\mathrm{K}]}\right)^{1/2}. \tag{2.25}$$

Moreover, for this description the partition function $U(T) = \sum_m g_m \cdot \exp\left(-\frac{E_m}{k_B T}\right)$ for atom and ion, electron mass m_e, ion temperature T_i and reduced Planck constant $\hbar$ are needed. At last the Planck function can be used in a TE to describe the energy density of photon excitation from a plasma that can be considered as a black body radiator and is given as

$$W(\nu) = \frac{8\pi h \nu^3}{c^3} \left(\exp\left(\frac{h\nu}{k_B T_{ph}}\right) - 1\right)^{-1}, \tag{2.26}$$

using the photon temperature T_{ph}, speed of light c and photon frequency ν.

Local Thermodynamic Equlibrium (LTE)

Due to its transient and non-homogeneous character, a laser-induced plasma can not be considered to be in a TE. Cristoforetti et al. (2010) [46] gave a good critical overview on how to describe a LIP. A Local Thermodynamic Equilibrium (LTE) in small fractions of the plasma can be used as a first assumption to describe the system. The deviation from the TE occurs in the Planck function. Here, it is required that the plasma is optically thick for all frequencies. It does not hold in LIP, because photons are able to escape from it, which leads to an imbalance between emission and absorption. But, as long as the collisional energy transfer is greater than the losses from the escaping photons, Boltzmann distribution of the population, Maxwell velocity distribution and Saha equation are still applicable in an LTE plasma. In this context $T_{exc} = T_e = T_H \neq T_{ph}$ holds. Considering the plasma in a stationary and homogeneous configuration, LTE conditions can be verified by the McWhirter criterion [47]. Here, the decay rate of a level n to m is at least 10 times higher than the rate of collision-induced transitions, which ends up in the expression for the electron number density n_e as

$$n_e \left[\mathrm{cm}^{-3}\right] > 1.6 \times 10^{12} \left(T \ \ [\mathrm{K}]\right)^{1/2} \left(\Delta E_{nm} \ \ [\mathrm{eV}]\right)^3 . \tag{2.27}$$

According to this approximation, the plasma is assumed to be optically thin. Apparently it does not take into account the process of self-absorption. This occurs, when the population of the ground state is reduced by the emission of a photon of the resonance transition respectively from another part of the plasma. As a LIP is spatially and temporally in-homogeneous, this conditions can change locally, where parts of the expanding plasma can be optically thick and others thin for several photon frequencies. Moreover, it appears in certain parts of this plasma that the electron and heavy particle temperature deviate. Especially in a vacuum or low pressure environment, where the expansion is too fast and atoms, ions and electrons are not able to reach the thermodynamic equilibrium. Indeed it is possible that the McWhirter criterion, expressed in equation (2.27), can be fulfilled, even though the time of variation of the thermodynamic parameters is much longer than the relaxation time τ_{rel}, which is basically the re-equilibration time of the ground state. This can be expressed by the relations for time dependent temperature and number density

$$\frac{T(t+\tau_{rel}) - T(t)}{T(t)} << 1 \quad \text{and} \quad \frac{n_e(t+\tau_{rel}) - n_e(t)}{n_e(t)} << 1. \tag{2.28}$$

This shows that the McWhirter criterion is a necessary but not sufficient criterion that needs to be fulfilled to characterize a plasma of transient properties like a LIP. Note that therefore equation (2.28) is a second criterion to verify the LTE character of the observed plasma. For this purpose the relaxation time can be estimated by the collision cross section σ_{mn} of inelastic collisions and electron incident velocity v to

$$\tau_{rel} \approx \frac{1}{n_e \langle \sigma_{12} v \rangle} = \frac{6.3 \cdot 10^4}{n_e f_{mn} \langle \bar{g} \rangle} \Delta E_{mn} (k_B T)^{1/2} \exp\left(\frac{\Delta E_{mn}}{k_B T}\right). \tag{2.29}$$

To estimate this, the transition energy ΔE_{mn} and oscillator strength f_{mn} between level m and n and effective gaunt factor $\bar{g}$ have to be known. This time has to be on the order of the expansion time τ_{exp} of the LIP. For instance, for this time, the lifetime of the observed plasma spectrum of a fs-plasma generated in argon environment is measured as $\tau_{rel} \sim 10^{-6}s$. The relaxation time can be estimated for different species in the plasma of typical values $n_e \sim 10^{16}\,\mathrm{cm}^{-3}$ and $k_B T_e \sim 1\,\mathrm{eV}$ for copper as $\tau_{rel} \sim 10^{-9}\,\mathrm{s}$ and for hydrogen $\tau_{rel} \sim 10^{-4}\,\mathrm{s}$. The fact that these values deviate for different species in the same plasma makes it critical to apply a LTE to a LIP (again also with a remark on vacuum environments where expansion times can be much shorter) and it needs to be estimated before it is used to describe the plasma. As Cristoforetti's review points out there is a third criterion to be fulfilled to be able to apply the LTE to the LIP. The non-homogenity of the plasma also needs to be considered, arises from the significant spatial temperature and electron number density gradient, which can lead to diffusion processes of atoms and ions within the plasma. The proposed third criterion says that the diffusion length $\lambda = (D \cdot \tau_{rel})^{1/2}$ during the relaxation time must be shorter than the variation length of the plasma properties. This is expressed as

$$\frac{T(x+\lambda) - T(x)}{T(x)} << 1 \quad \text{and} \quad \frac{n_e(x+\lambda) - n_e(x)}{n_e(x)} << 1. \tag{2.30}$$

An estimation of the diffusion coefficient is given as

$$D \approx 3 \cdot 10^{19} (\mathrm{cm}^2 \mathrm{s}^{-1}) \frac{k_B T\ [\mathrm{eV}]}{N_{ion} M_A} \tag{2.31}$$

with the number density of ions N_{ion} in the plasma and the relative mass of the considered species M_A. Defining it for the condition $N_{ion} = n_e$ and $M_A = 1$, this length is usually on the order of $10^{-5}\,\mathrm{m}$. This diffusion length has to be compared to the plasma diameter d, which can be estimated as $10^{-3}\,\mathrm{m}$ and is claimed to be 10 times larger than $\lambda(\tau_{rel})$ to fulfill the LTE conditions.

Taking all these criteria into account only a few LIP fulfill the LTE condition and the observation of plasma parameters has to be treated cautiously. The experimental conditions examined in this thesis often does not explicitly indicate that these conditions are fulfilled, due to plasma persistence in air or vacuum environment and plasma generation by short laser pulses.

Chapter 3

Instruments and Methods

The experimental results presented in the subsequent chapters are based on a couple of methods and systems that are explained in this chapter. Below, all used laser systems and spectrometers used are described in detail. Moreover, methods and concepts to estimate plasma parameters from the LIBS results are presented. The chapter closes by introducing a couple of techniques that are used to make predictions on material composition and hydrogen isotope retention of the PFCs used.

3.1 Laser Systems

Short and ultra-short laser pulses of pulse durations in the femtosecond regime were possible after the discovery of self-mode-locking in Ti:Sa lasers in 1991 by Sibbett et al. ref. [48]. Here, an overview of the basic concept of these systems is given including the description of the four laser systems that were used for the experiments described in this thesis.
Starting with the basic concept of a laser, the concept of an optical oscillator needs to be explained. In general, this is necessary in combination with a module to enhance the generated light for a pulsed laser system. To build such an optical oscillator at least three components are needed: An active medium that is able to radiate in a given spectral range when it is optically excited, a pump mechanism to initiate the emission from the active medium and a cavity (or laser resonator) consisting of at least two mirrors. As the active medium gas mixtures, semiconductors or crystals are used were it is possible to generate a population inversion. For this, atoms that provide at least two different excitation stages or mixtures of atoms are needed. Depending on the used active medium, the optical excitation can be made by pulsed high voltage discharge currents or other light sources like diodes or another laser. The photons released from the active medium tends to be captured in the optical cavity and are able to initiate stimulated emission of more photons in the same mode. One of the two mirrors in the cavity is working as an output coupler that is semitransparent for the photon wavelength. The photons released from the cavity are then coherent to each other and can be further manipulated in different variants of modules.

The basic mode of operation described here is used both for Continuous-Wave (CW) and pulsed laser. At least for short and ultra-short laser pulses the generated modes in the laser resonator need to have a fixed phase relationship. This can be achieved by a process called mode locking, which is initiated by an non-linear element inside the cavity. Here, active methods using a periodic modulation, for example, an Acousto-Optical Modulator (AOM), and passive methods initiated by saturable absorbers can be distinguished. In a saturable absorber the transmittivity depends on the incident intensity, which is why the cavity releases the light only when the generated modes in the laser resonator are in phase and a short pulse is present at the output coupler. The pulses released from the cavity have a high repetition rate, but low pulse energy. In the next step most systems make use of Chirped Pulse Amplification (CPA) discovered by Strickland and Mourou [18]. Here, the seed pulses from the oscillator will be stretched by, for example, a defined amount of glass with a known second order dispersion or a grating setup that ensures a spectral chirp where the high frequency part of the spectrum ("blue") is delayed compared to the low frequency part ("red"). These stretched pulses have the same pulse energy but a significant lower intensity, which is necessary for the amplification step. Here, the pulses are guided several times through another pumped active medium to enhance the photon number per pulse. A following compressor module is able to readjust the path lengths of the different frequencies in the spectrum to restore the initial pulse duration. This is solved by gratings, prism, or multi-layer mirrors to achieve the compression.
In addition to this basic generation process, different systems are equipped with a variety of modules to manipulate pulse duration and energy, wavelength and profile. In the following sections the used setups are described, including special features that are used in the experiments in this thesis.

3.1.1 PHASER

The Phase-stabilized Heine lASER (PHASER) in the experimental group for Laser- and Plasma physics at Heinrich Heine University Düsseldorf (HHU) is a customized system from *Femtolasers GmbH* that delivers near infrared (bandwidth 650 nm - 950 nm) ultra-short pulses of < 10 fs pulse duration and 1 mJ pulse energy at a repetition rate of 1 kHz. In the oscillator (*FEMTOSOURCE*^{TM} *rainbow*^{TM}) a Ti:Sa (titanium sapphire crystal) is pumped by a Diode Pumped Solid State (DPSS) Nd:YAG (neodym-doped yttrium aluminum garnet crystal) laser. The mode locking is initiated by a rapid change of laser resonator length that starts a Kerr lens effect inside the Ti:Sa crystal. This passive mode locking makes use of an artificial saturable absorber induced by the Kerr lens effect inside the gain medium, which is why it is also called self-mode-locking. The Kerr lens effect is basically a non-linear self focusing of the carrier wave that can increase the overlap of laser and pump beam, leading to a higher gain in every round-trip, where the phase relationship between the different modes matches perfectly. The pulse train of 6 nJ, 7 fs pulses is released with a repetition rate of 75 MHz and then enters the *CEP4*^{TM} module. Here, the Carrier-Envelope Phase (CEP) is

stabilized with an Acousto-Optical Frequency Shifter (AOFS). The CEP indicates a phase difference between the carrier wave and the envelope of the intensity and becomes important in the observation of extreme non-linear optical effects.
With a decreased pulse energy of 2 nJ, the laser seeds a multi-pass amplifier with another Ti:Sa crystal pumped by a green 120 ns laser as the gain medium. The stretched pulses are enhanced in ten passes, while in the first four the MHz pulse train is used, it is chopped by a Pockels cell to 1 kHz for the remaining six passes. A Pockels cell uses an electro-optical effect to change the polarization via a voltage controlled waveplate. A programmable acousto-optical filter (DAZZLER) is used to manipulate the amplitude and phase-shape for the optimization of the remaining amplification steps. The DAZZLER compensates higher order dispersion effects and the so called gain-narrowing of the spectrum. The diverging output beam (bandwidth 775 nm - 825 nm) is collimated and sent to a grating compressor resulting in the bandwidth-limited pulse duration of 25 fs and pulse energy of 3 mJ.
Shorter pulse durations can be achieved using a hollow fiber filled with a noble gas. Here, the effect of self-phase modulation is used that causes an increase in optical bandwidth when the initial pulse is un-chirped or slightly up-chirped. This increase in bandwidth to the spectrum in the beginning results in a time bandwidth product where a pulse duration below 7 fs is possible. This is also referred to as few-cycle pulses, meaning few cycles of the electric field fit into one pulse. In this setup the spectral broadening is realized using a 2 m long glass fiber in an evacuated vessel refilled with neon gas at a pressure around 600 to 1200 mbar. The entrance and exit windows are tilted to the Brewster's angle to ensure maximal throughput of the s-polarized laser beam.
The diverging beam escaping from the hollow fiber is collimated and guided over the optical table to the vacuum vessel that connects the laser to the three different experimental chambers. A mirror compressor inside this vessel compensates the second order dispersion the beam undergoes on its path from the hollow fiber to the optical table and the entrance window. As a result, the usable pulses at the experiments have a duration of less than 10 fs and a pulse energy of around 600 µJ. A telescope is able to extend the beam profile beamdiameter to $D_0 = 55\,\mathrm{mm}$.
It is critical to work with such short laser pulses to reach intensities of up to $10^{17}\,\mathrm{Wcm}^{-2}$. It is necessary to keep track of beam profile and pulse duration for each experiment. A camera keeps track of the Gaussian beam profile, while a SPIDER (Spectral Phase Interferometry for Direct Electric-field Reconstruction) diagnostic can measure the spectral phase of the spectrum directly, which leads to a prediction of the pulse duration. A SPIDER is basically a third order autocorrelator in the frequency domain where the interference of two slightly frequency shifted pulses is observed to detect the spectral phase. The principle goes back to C. Iaconis and I. Walmsley (1999) (see Ref.[49]), and was expanded to a single shot option in 2003 as described in Ref. [50].
Moreover, on the optical table a fully reflective attenuator is installed that can be used to change the pulse energy in a range of four orders of magnitude without changing any optical parameter of the laser pulses. The theory, design and characterization of this module is given

in the dissertation of Julian Wegner (2020, ref. [51]). This module is important to be able to change the pulse energy in ablation studies on different materials that are described in this thesis. Furthermore, when it comes to the observation of ignited plasmas, it turns out that a controlled pre-pulse in a defined time frame can be useful to enhance for example, the emission of K-α radiation or the plasma radiations discovered here. In section 3.1 the design of the used pre-pulse generator is described fully.

3.1.2 Amplitude s-Pulse

The compact high power femtosecond laser *Amplitude s-Pulse HP* is frequently used in medical applications, laser processing and LIBS setups. Its typical output are 500 fs laser pulses at $\lambda = 1030$nm with pulse energy of 600 µJ and up to 300 kHz repetition rate in the TEM_{00} Gaussian mode. At the Laser technologies group at Lawrence Berkeley National Laboratory (LBNL), this laser is used for high resolution LIBS applications and surface processing. The fundamental laser wavelength is used to generate the second and third harmonic at 515 nm and 343 nm in a non linear element. Typical pulse energies of the third harmonic used are in the 100 µJ regime.
The laser itself consists of a laser oscillator with a Ytterbium doped crystal that has absorption bands in the near infrared regime (940 nm to 980 nm), which are excited by direct diode-pumping. A non-linear mirror with reflectivity depending on the incident pulse energy ensures the pulse generation and a SEmiconductor Saturable Absorber Mirror (SESAM) is used to initiate the mode-locking. From this femtosecond low pulse energy ($\sim$ 20 nJ) high repetition rate (40 MHz) pulse train generated, a single pulse is picked by a Pockels cell. This pulse is given a spectral chirp in a stretcher module to be seeded into the amplifier module. During a necessary amount of round-trips through a CW laser pumped crystal, a unit including a Faraday rotator sends the pulse to the compressor. Due to the pumping option with the CW laser, a high stability can be achieved in this setup. By having the option to use the third harmonic frequency, a high resolution LIBS setup can be achieved, where ablation depths of ≤ 10 nm are possible.

3.1.3 Quantel Brilliant EaZy

In typical LIBS applications, nanosecond pulses are generated in Q-switched solid-state setups. The Quantel Brilliant EaZy and similar systems are used at Dalian University of Technology. These systems have a Nd:YAG crystal as the active medium being pumped by a flash lamp to generate Gaussian like infrared (1064 nm) pulses of $5 - 10$ ns pulse duration, 300 mJ pulse energy at a repetition rate of 10 Hz. The Q-switch is an AOM that makes use of the effect that the refractive index depends on a sound wave coupled to a crystal. This wave is generated by a Radio-Frequency (RF) power to control the permeability of the laser cavity. By switching the RF power off, a single pulse escapes the cavity. The pulse duration of which depends on the optical opening time of the AOM. By changing the delay between the flash-lamp excitation and the Q-switched RF power, the output pulse energy is tuned.

3.1.4 EKSPLA PL2241

As a middle ground between the "long" nanosecond pulses and ultra-short pulses in the femtosecond regime, a picosecond laser is used at Forschungszentrum Jülich for LIBS experiments with a good depth resolution. The EKSPLA PL2241 laser is a high energy picosecond laser using Nd:YAG rods as the active medium in the cavity, providing pulses of 35 ps, 46 mJ and a repetition rate of 1 Hz. The DPSS oscillator seeds pulses are enhanced by a regenerative flash lamp pumped amplifier and a harmonics module gives the opportunity to use the second and third harmonic. In the studies shown, the third harmonic at 355 nm is mostly used and the laser profile is close to a flat top or super-Gaussian shape. Similar to the nanosecond laser, it is possible to manipulate the timing between flash lamp pumping and Q-switch output signal of the amplifier to change the pulse energy.

3.2 Design of the Pre-Pulse Module

In this section, the opportunity to create defined collinear ultrashort pre-pulses is discussed. Various experiments on laser matter interaction made it necessary to provide known plasma conditions before the main laser pulse enters the target. Here, one might think of high harmonic generation on solid surfaces or the enhancement of K-α x-ray flashes as presented, among others, in ref. [52] and [53]. One possible way to manipulate the material is to generate a pre-pulse of known pulse duration and energy that heats the target surface. The expansion and with it the scale length of the plasma created can be controlled by the time delay between the two pulses. If needed, a pre-pulse generator can be applied to the beam path after the reflective attenuator on the table by an adjustable optical breadboard. A schematic look on the realization of it is provided in fig. 3.1 (left) and a technical description of the alignment and accuracy of this module is given in appendix D. The incoming pulse is split by a 10:90 beamsplitter, while the main pulse is transmitted and guided over the high-precision linear stage that can be adjusted with a 1 µm step size. This complies with a pulse delay of ~ 3 fs. The delay-stage is controlled by an DC motor and encoder that enables a maximum pulse delay of 800 ps. The second beamsplitter reunites the two parts and guides them to the experiments in the vacuum chambers. This "Mach-Zehnder-like" setup developed in Jonah Book's bachelor thesis (2021) [54] is chosen to ensure the least possible dispersion in the two arms using the same amount of transmitted glass. The beamsplitters are made of a 3.05 mm thin fused quartz substrate with antireflective rear sides, while the second one has a gold coating on the front side that reflects 90 % of the incoming broadband laser pulse. Without the gold coating, the first beamsplitter has a reflectivity for s-polarized light of roughly 10 % over the complete spectral range. In fig. 3.1 (right), SPIDER measurements of the 8 fs laser pulse with and without the second beamsplitter are shown. There are no relevant spectral break-ins observed that could lead to a lower spectral width. By adjusting the amount of glass in the beam paths, the dispersion can be controlled to end up with the same pulse duration with and without the beamsplitters. First experiments on the emission of K-α

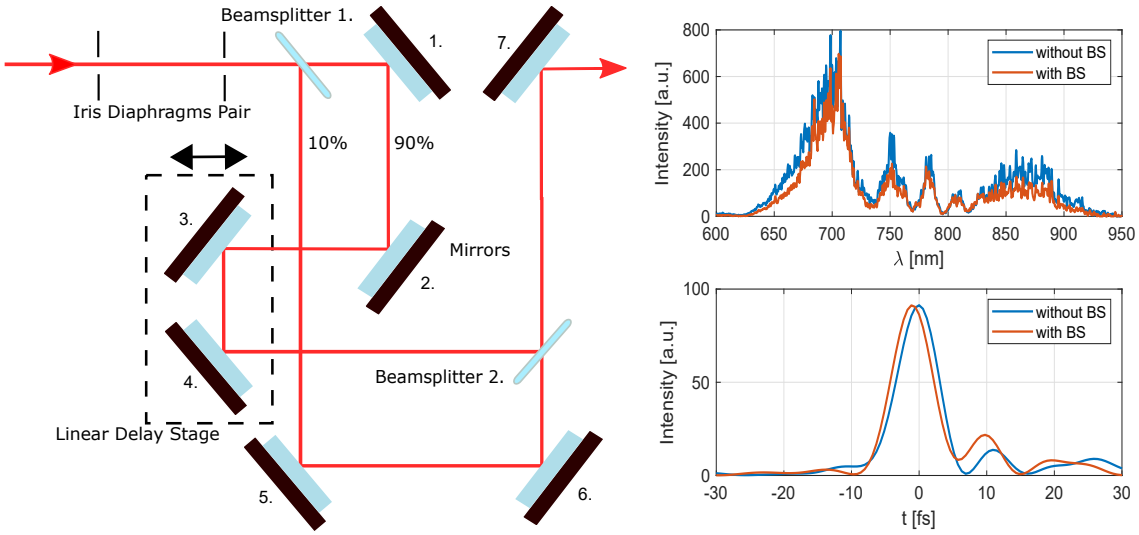

Figure 3.1: (left): Schematic view on the beam path of the laser pulses (red) in the pre-pulse generator. To ensure parity of reflection the number of mirrors is even for both arms. (right): Measurement of the spectrum (top) and the corresponding temporal intensity profile provided by the SPIDER (bottom) with and without the coated beamsplitter (BS), compare ref. [54].

radiation from copper targets displayed in a signal enhancement by the factor three. The use of a double-pulse or pre-pulse system is also interesting in the context of LIBS experiments, where a pre-pulse can change the coupling characteristic of the main pulse to enhance the amount of energy absorbed in the created plasma. It has been shown in ref. [55] that it is possible to enhance selected spectral lines in the expanding plasma by the factor five with a reasonable delay and pulse energy ratio. Optionally the beamsplitters can be changed to the 50:50 splitting variant to acquire the pre- and main pulse ratio necessary for these experiments.

3.3 Spectroscopy

Optical spectrometers are the most important diagnostic tools used in LIBS. Typical temperatures of a laser-induced plasma after the breakdown of $T_e \approx 20,000\,\mathrm{K}$ emphasizes that the emitted spectrum can be expected to be in the near Ultra-Violet (UV) and VISible (VIS) wavelength region. Due to deviating transparency of optical glasses used for lenses and windows in all experimental setups, the spectral region of interest can be covered from $\sim 200\,\mathrm{nm}$ to $\sim 800\,\mathrm{nm}$. In this region typical transitions of atoms and ions present in the plasma observed are detectable. In the experiments presented reflective spectrometers are used, as they are the most convenient method to detect the VIS and near UV emission.
The basic design of such a spectrometer is explained and limitations of resolution and spectral range values are discussed in this section. Moreover, all instruments, including the detector type used in the experiments are covered here. Refer to appendix B for detailed information.

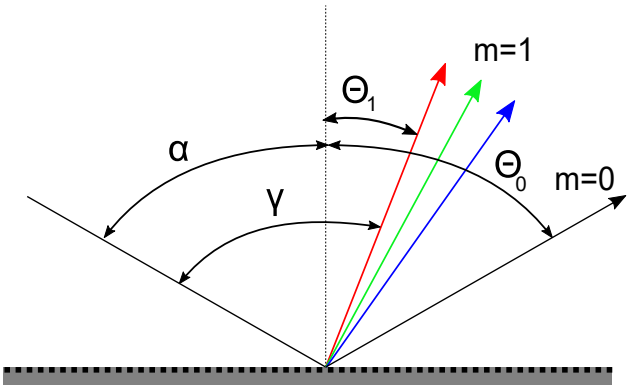

Figure 3.2: Schematic depiction of the spectral decomposition of light with an angle of incidence α, reflected angle Θ_m of diffraction order $m = 1$ and $m = 0$, and total angle γ. According to the definition in equation (3.1) it holds that $\alpha = -\Theta_0$.

3.3.1 Spectrometer Design

The fundamental theoretical parameters presented that are necessary to design a grating spectrometer are taken from common literature about spectroscopy and basic optics. Reflective optical gratings with UV-enhanced aluminum coatings are used for the ultra-violet and emission in the visible spectral range (UV, VIS) from 200 nm to 800 nm. This is the typical range that is analyzed in LIBS experiments. The gratings equation for reflective gratings is given as

$$\sin\alpha + \sin\Theta_m = \frac{m\lambda}{g} \tag{3.1}$$

with the lattice constant g, the exit angle Θ_m of diffraction order m and entrance angle α of light with wavelength λ. All measured angles are defined from the gratings normal in the same direction as shown in fig. 3.2. Here, the 0th order is reflected at $\Theta_0 = -\alpha$ by definition, and the total angle $\gamma = \alpha - \Theta_m$ between the incoming and exit light is fixed.
By variation of the angle α, the wavelength observed in the detector plane can be chosen. With the use of equation (3.1), an addition theorem, and the fixed total angle γ, α can be calculated by

$$\sin\left(\alpha - \frac{\gamma}{2}\right) = \frac{\pm\, m \cdot \lambda \cdot g}{2 \cdot \cos\left(\frac{\gamma}{2}\right)}. \tag{3.2}$$

However, from the angular dispersion

$$D = \frac{\mathrm{d}\Theta}{\mathrm{d}\lambda} \quad \left[\frac{\mathrm{rad}}{\mathrm{nm}}\right] \tag{3.3}$$

that can be received for a fixed incidence angle as

$$\frac{\mathrm{d}}{\mathrm{d}\lambda}\left(g(\sin\alpha + \sin\Theta)\right) = \frac{\mathrm{d}}{\mathrm{d}\lambda}\left(m\lambda\right) \quad \Leftrightarrow \quad \frac{\mathrm{d}\Theta}{\mathrm{d}\lambda} = \frac{g \cdot \cos\Theta}{m} \tag{3.4}$$

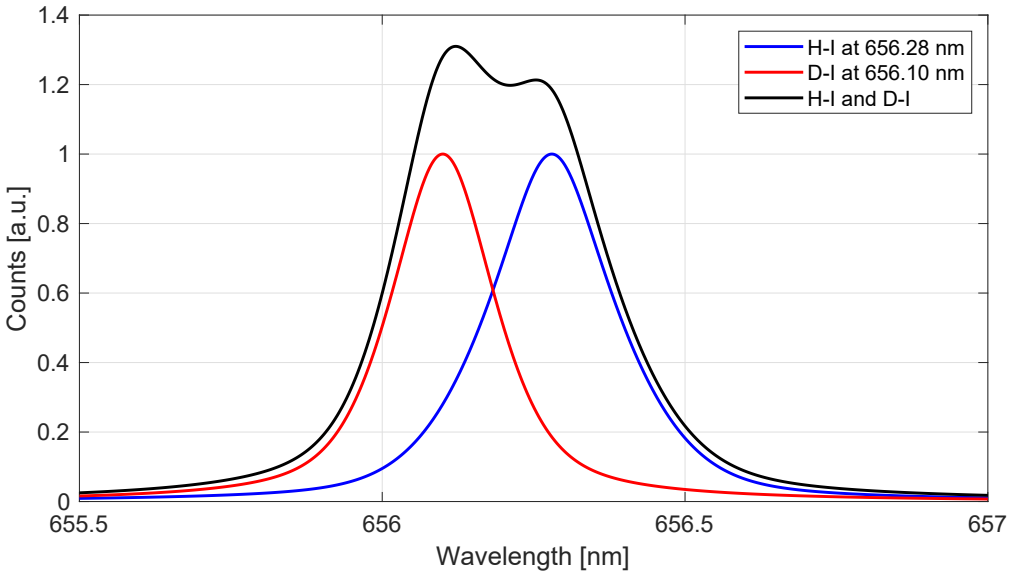

Figure 3.3: Balmer-α lines of hydrogen (blue) and deuterium (red) shaped as Voigt profiles separated by wavelength distance $\Delta\lambda = 180\,\mathrm{pm}$ and the combination of both lines by addition in black are shown. Width of the lines are approximated for expected plasma parameters $T_e = 15,000\,\mathrm{K}$ and $n_e = 10^{16}\,\mathrm{cm}^{-3}$

the covered spectral range and spectral resolution can be derived. To describe this, the reciprocal linear dispersion of a spectrometer with focal length f is given as

$$P = \frac{1}{D \cdot f} = \frac{\cos\Theta \cdot g}{m \cdot f}. \tag{3.5}$$

When the dimension (number of pixels N_{pixel}) and pixel size p of the detector is known, the covered spectral range for a fixed entrance angle is calculated as

$$\lambda_{1,2} = \lambda \pm \frac{p \cdot N_{pixel} \cdot P}{2}. \tag{3.6}$$

From this it can be passed over to the possible smallest resolvable spectral element $\Delta\lambda$ defined for the spectrometers in use. In this context, literature somehow refers to a synthetic "resolving power"

$$R = \frac{\lambda}{\Delta\lambda}. \tag{3.7}$$

The maximal resolution possible for the optical system can be obtained by the Rayleigh criterion from John W. Strutt, III Lord Rayleigh (1879) [56]. It gives an idea, how to obtain the minimum distance of two lines of the same intensity in the focal plane of the objective mirror. It says that two adjacent light points can be perceived separately, if the main maximum of the first line is located in the plane of the first minimum of the second line. This distance corresponds to the Full Width at Half Maximum (FWHM) of one spectral line. In fig. 3.3 two spectral lines from transitions in hydrogen and deuterium shaped by Voigt profiles are shown separated by $\Delta\lambda = 180\,\mathrm{pm}$. The Voigt profile arises from the convolution

of a Lorentzian and a Gaussian profile. The involved line broadening effects are discussed in chapter 3.4. Beyond this, the minimal angle between two spectral lines are given as

$$\Delta\Theta = \frac{\lambda}{N_{grooves} \cdot g \cos\Theta}, \tag{3.8}$$

which is the FWHM angle difference, where $N_{grooves}$ is the number of grating grooves lighted. This is the same angle difference as the angle between the diffraction maximum of a spectral line and its first minimum, which is the closest distance of two separately perceptible lines according to Rayleigh. The minimum distance of two adjoined signals still distinguishable according to Rayleigh criterion in the detector plane are limited by the FWHM of the entrance slit image in the detector plane FWHM_t. The smallest resolvable spectral element is then calculated using the reciprocal linear dispersion as

$$\Delta\lambda = \Delta x \cdot P. \tag{3.9}$$

With the size of the slit image in the detector plane defined by $\Delta x = \mathrm{FWHM}_t$ and the grating equation (3.2), it is given as

$$\Delta\lambda = \frac{\mathrm{FWHM}_t \cdot \cos\Theta}{m \cdot f} \frac{\lambda}{\sin\alpha + \sin\Theta}. \tag{3.10}$$

A way to estimate the "resolving power" for a classical grating spectrometer is then given by converting this equation into the form of (3.7) to

$$R = \frac{m \cdot f}{\mathrm{FWHM}_t} \cdot \left(\frac{\sin\alpha}{\cos\Theta} + \tan\Theta \right). \tag{3.11}$$

Note that the entrance slit image results from a convolution of broadening effects by the used optics in the spectrometer and the detector pixel size p. Assuming Gaussian line shapes here, the total image size can be calculated from the entrance slit size d as

$$\mathrm{FWHM}_t^2 = \left(\frac{\cos\alpha}{\cos\Theta} \right)^2 \cdot d^2 + \mathrm{FWHM}_c^2 + \mathrm{FWHM}_0^2 + \mathrm{FWHM}_d^2 + p^2. \tag{3.12}$$

From the Point Spread Function (PSF), which is an optical transfer function from a point source to the spatial domain, the size of the images of the collimating optics FWHM_c and imaging optics FWHM_0 are calculated. The diffraction limit of the grating FWHM_d can be estimated as

$$\mathrm{FWHM}_d = \lambda \cdot \frac{f}{d_2}, \tag{3.13}$$

where the diffracted ray diameter d_2 is governed by the so called f-number $F\#$, and distance of grating and imaging optic plane X as

$$d_2 = \frac{\cos\Theta}{\cos\alpha} \cdot \frac{f}{F\#} + \frac{X \cdot p \cdot N}{f}. \tag{3.14}$$

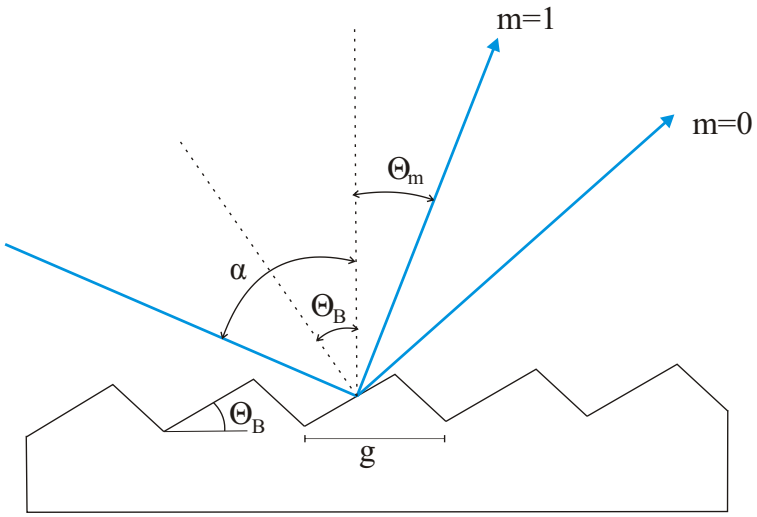

Figure 3.4: Reflective grating with lattice constant g blazed at an angle of Θ_B. The angle α between the incoming light and the grating normal are given as well as the exit angle Θ_m of the first diffraction order $m = 1$ as an example.

The f-number is given as the quotient of focal length and aperture diameter of the collimating optic. In the unintended case of a detector pixel size $p > \mathrm{FWHM}_t/2$ the resolution of the setup is limited by the detector itself. This is the reason why it is referred to as a synthetic "resolving power".
Finally a short annotation to the use of the Rayleigh criterion needs to be given. It seems that this criterion fulfills a limitation rule to the resolution, which is a misleading interpretation. Here, only the possibility to distinguish two adjacent points with the human eye is limited. Another limitation of it is given by Ernst Abbe (1873) who analyzed the maximal resolution in microscopy and found that the minimal distance of two points is given by

$$b_{min} = \frac{\lambda}{2n \sin \alpha}, \tag{3.15}$$

where n is the refractive index between the object and microscope. Moreover, it is also possible to go below this limit using the right detector and evaluation routine. In most cases the limiting factor of the resolution is the pixel size of the detector of 26 µm for typical used detectors in LIBS applications. That is why the Rayleigh criterion is a good approximation to estimate the maximal "resolving power".
The used reflective gratings in the presented spectrometers are produced to improve spectral sensitivity for particular wavelength regions. In fig. 3.4 the diffraction on a reflective grating due to the grating equation is illustrated. Angles that are sketched to the right of the grating normal are defined. Here, a special configuration of the lattice, called blaze grating, is shown. A blazed grating has grids that are tilted by an angle Θ_B to the gratings surface. Due to this tilt the intensity in one chosen diffraction order or wavelength can be maximized. The

blaze angle is calculated as

$$\Theta_B = \arcsin \frac{m\lambda}{2g} \tag{3.16}$$

using the Littrow-configuration where an incoming beam is reflected in itself. The opportunity to optimize the reflectivity of chosen wavelengths and diffraction orders is used to modify the observed spectral range or gaining the resolution in an Échelle spectrometer. Another modification is the use of a holographic grating. Here, the grating is formed by two interfering laser beams that process a sinusoidal surface structure. With this technique it is possible to generate gratings with a high number of lines per millimeter, which leads to higher possible resolutions. Moreover, on holographic gratings the diffused light from the surface is minimized.
In the end the main issue in spectroscopy is to find a suitable configuration that offers a high resolution, reasonable bandwidth, and enough light throughput to deal with low light sources like plasma breakdowns induced by femtosecond lasers.

3.3.2 Instruments

In general, a spectrometer consists of an entrance slit, a collecting optic, a diffraction grating or an optical prism, an objective optic, and a detector. The following summary will concentrate on reflective plane gratings. Concave gratings used for example in a Rowland cycle spectrometer, have advantages for sub 100 nm wavelengths, because one avoids having to use a second imaging optic. In the experiments presented only spectrometers of the Czerny-Turner type are used, because they bring a good balance between possible resolution and light throughput. Moreover, the camera solution used to catch the quickly expanding laser-induced plasma is introduced.

Czerny-Turner Spectrometer

With the Czerny-Turner configuration the collected light from the entrance slit is collimated onto the blazed or holographic grating. The diffracted light is imaged onto the detector by the objective mirror. Refer to fig. 3.5 for the principle application. It can quickly be recognized that the used concave mirrors and possible steep incoming angles onto the grating can lead to different optical aberrations like astigmatism, coma, spherical aberrations and defocusing. Dealing with these issues and how to overcome a few of them has been explained by Shafer et al. (1964, ref. [57]). The Czerny-Turner configuration itself is a correction of a so called Ebert system, where only one huge concave mirror is used instead of two. With two mirrors it is possible to correct some aberrations by tilting the second mirror.
To reach a high resolution with an Czerny-Turner spectrometer a big grating with a small lattice constant in combination with a long focal length of the objective mirror needs to be used. For example a $f = 750\,\text{mm}$ spectrometer with a grating of 1200 l/mm can generate a minimal resolvable spectral element of $\Delta\lambda = 0.05\,\text{nm}$ for a wavelength of 600 nm. This corresponds to a "resolving power" of $R = 12,000$. The whole bandwidth that can be

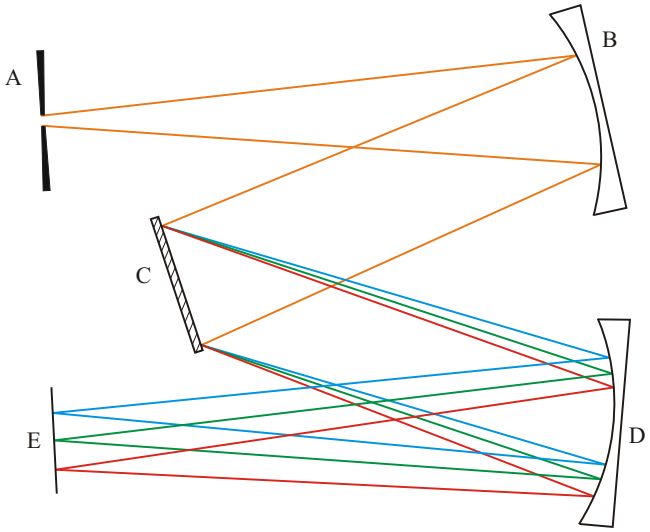

Figure 3.5: Czerny-Turner spectrograph is shown with an entrance slit A, collecting mirror B, rotatable reflective grating C, objective mirror D, and a detector E. Principle of the illustration taken from ref. [57].

covered during one operation is given as $\Delta\lambda_{bw} = 26\,\text{nm}$. Note that the diffraction order $m = 1$ is imaged on the detector in the Czerny-Turner configuration. In some cases it is possible to detect spectral lines that correspond to higher diffraction orders. To avoid those, it is advisable to use spectral filters in front of the entrance slit. In the experiments described in this thesis the spectrometers used are the models *IsoPlane320* from *Princeton Instruments*, *Kymera 328i* and *Shamrock750* from *Andor*, and the *Horiba Jobin-Yvon1250M*. These models are based on the Czerny-Turner setup with a focal length assigned by the number included in their name. In appendix B more details on the used setups are given. Note that all spectrometers have to be calibrated to adapt the internal dispersion and spectral sensitivity. This is executed by hollow cathode-, mercury-, and halogen- calibration lamps, where necessary.

Detector Solutions

For the covered spectral region discussed in this section, the most convenient and fastest way to detect the emission would be a Charge-Ccouple Device (CCD) or an active sensor realized by Complementary Metal-Oxide-Semiconductors (CMOS). Those sensors are used to detect the spectral resolved emission from the induced plasma. However, this radiation usually has a very low intensity and can barely be covered by one of those sensors with adequate sensitivity. For this reason the sensor is combined with an intensifier stage. By attaching one of those image intensifiers in front of the sensor, a high speed camera for spectroscopic or imaging applications can be constructed. In general, an intensifier consists of a photocathode, a Micro-Channel Plate (MCP), and a phosphor screen. Photoelectrons generated at the photcathode are multiplied in the MCP and accelerated towards the phosphor screen. These accelerated

electrons are converted back to photons that are then guided by lenses or optical fibers to the detector. In addition to the high amplification of the detected signal, this kind of intensifiers can be used to control the exposure time of the camera. This electronic shutter function can be controlled via the voltage between the photocathode and the MCP. By reversing this voltage, the electrons generated can not be multiplied by the MCP and the phosphor screen stays dark. This process is called gating and can be used to detect the time resolved optical emission of the laser-induced plasma or other fast processes. In general it is possible to control the gate delay between the observed event and the camera, and the gate width defining the exposure time. With the used iCCD (intensified CCD) models typical gate delays $\geq$ 100ps and gate widths of < 5 ns are possible. Hoess et al. (1999, ref. [58]) expect a theoretical limit for the gate delay of 40 ps caused by the propagation speed of electrical field strength variations. This technology makes it possible to separately detect the characteristic and continuum radiation of the expanding plasma, and to examine the temporally changing plasma parameters.

3.4 Determination of Plasma Parameters

With the techniques described, the spectral characteristics of a laser-induced plasma can be observed with the temporal accuracy given by the iCCD optical gate width and the spectral resolution of the chosen spectrometer option. As pointed out in chapter 2.2.2 about the thermal character of the expanding plasma it is possible to describe it under certain conditions in a LTE. This approximation is necessary for the methods that are to be described in the following sections in order to determine the plasma temperature T_e and electron number density n_e from the observed spectrum. These parameters are necessary to be able to choose correct laser parameters for the purposes presented and furthermore to discover concentration variations of the observed material and isotopes in, for example, CF (Calibration Free) LIBS applications.

3.4.1 Spectral Line Profile

The real spectral lines that can be measured with the optical spectrometer are broadened due to a couple of reasons. First of all, the natural line broadening that is caused by the quantum mechanical uncertainty of the energy transition between the upper and lower level ΔE, and the lifetime Δt given as $\Delta E \Delta t \sim h$ is in generally very small compared to other line broadening effects. The line profile is dominated by collisional and thermal broadening. These two processes are described by the Stark- and the Doppler effect respectively. The description starts with the broadening caused by collisions that randomize the phase of the electromagnetic waves emitted from the energy transition of the bounded electron. This phase change leads to a shorter lifetime, which consequently results in a broader spectral line. From this follows a dependency of the line width on the number density n_e, as collisions are more likely in a plasma of higher density. The resulting spectral line shape can be described by a

Lorentz profile,

$$L(\lambda, w_{stark}) = \frac{w_{stark}}{\pi \cdot (\lambda^2 + w_{stark}^2)}, \tag{3.17}$$

with the Half Width at Half Maximum (HWHM) w_{stark} that can be determined from the Stark broadening equation

$$n_e = \frac{w_{stark}}{w_0} \cdot 10^{16}\mathrm{cm}^{-3}. \tag{3.18}$$

Note that the Stark broadening parameter w_0 of the chosen spectral line depends on the plasma temperature and can be found in literature. If these parameters are unknown, it is possible to estimate the electron number density by the hydrogen Balmer lines as described by Gigosos et al. (2003, ref. [59]), e.g. for H_α by the Full Width at Half Area (FWHA) as

$$\mathrm{FWHA[nm]} = 0.549 \cdot \left(\frac{n_e[\mathrm{cm}^{-3}]}{10^{17}}\right)^{0.67965} \tag{3.19}$$

using a linear fitting to filter the temperature dependence.
Moreover, the line shape is influenced by thermal effects. Considering the temperature dependent random motion of atoms and Ions in the plasma, described by the Maxwell velocity distribution, the Doppler-shifted line shape around the central wavelength λ_0 is determined by a Gaussian function of full width at half maximum (FWHM) $\Delta\lambda_G$ as

$$G(\lambda, \Delta\lambda_G) = \frac{2\sqrt{\ln 2}}{\Delta\lambda_G\sqrt{\pi}} \exp\left(-4\ln 2 \frac{(\lambda - \lambda_0)^2}{\Delta\lambda_G^2}\right) \tag{3.20}$$

with the Doppler width $w_{doppler} = \Delta\lambda_G(2\sqrt{2\ln 2})^{-1}$ determined for the element of mass m by

$$w_{doppler} = \frac{\lambda_0}{c}\sqrt{2\ln 2 \frac{k_B T_e}{m}}. \tag{3.21}$$

In addition, the spectral line is shaped by the instrumental width w_{inst} that can be determined for the different used spectrometers with a reference lamp of known spectral broadening. Often used are low pressure discharge lamps of atomic gas like mercury (Hg) or argon (Ar), or Hollow Cathode Lamps (HCL) with heavy metals for this purpose. The spectral line shape is influenced by Gaussian profiles from the instrumental and Doppler broadening and by a Lorentz shape from the Stark- and natural- (negligible) broadening. A convolution of these two shapes describes the spectral line shape and is given as by the Voigt function. To be able to use this function as a numerical fit on data points, a so called pseudo-Voigt function is generated that is basically given as a linear combination of the Gauss $G(\lambda, \Delta\lambda_G)$ and the Lorentz $L(\lambda, \Delta\lambda_L)$ part as

$$V(\Delta\lambda_G, \Delta\lambda_L, \lambda) = \eta(\Delta\lambda_G, \Delta\lambda_L) \cdot L(\lambda, \Delta\lambda_L) + (1 - \eta(\Delta\lambda_G, \Delta\lambda_L)) \cdot G(\lambda, \Delta\lambda_G) \tag{3.22}$$

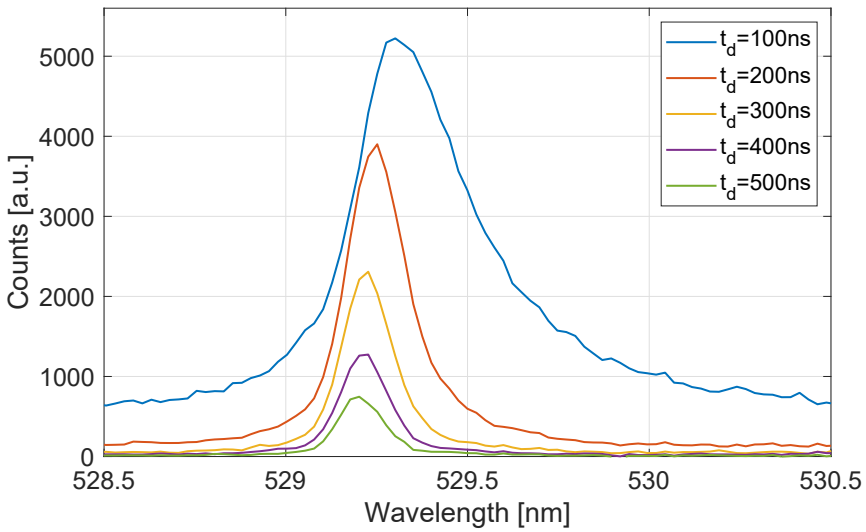

Figure 3.6: Spectral line Cu-I generated in fs-LIBS experiment using a 500 fs, 343 nm laser in Argon atmosphere. Here, five measurements are shown with gate delay t_d from 100 ns to 500 ns and a gate width of 100 ns.

using a numerical estimation for η taken from [60] and described in appendix C. The FWHM $\Delta\lambda_V$ of the Voigt-shaped spectral line is given as

$$\Delta\lambda_V \approx 1.0692\Delta\lambda_L + \sqrt{0.8664\Delta\lambda_L^2 + 4\Delta\lambda_G^2}. \tag{3.23}$$

It is important to consider that the line shape observed is also changed by the fact that it is not possible to record it in an infinitesimal time frame, as the plasma parameters of the LIP are usually changing exponentially in time. To visualize this effect, see fig. 3.6 that shows the changing line shape for a transient plasma generated with a 500 fs laser on copper. Here, the total line width of the atomic copper line at 529.25 nm decreases with a longer gate delay of the iCCD, which corresponds to the decreasing plasma temperature and density. Moreover, a red-shift of the central wavelength for shorter delays due to the higher temperature can be observed. As the observation time frame is 100 ns and the plasma parameters are changing exponentially, the spectral line detected is a superposition of differently shaped lines and it is problematic to talk about average plasma parameters calculated from these lines.
However, spectral lines of the expanding plasma observed are used to estimate the number density and temperature. A popular method to estimate the temperature is the usage of a Boltzmann plot, which will be described in the next section.

3.4.2 Boltzmann Plot

The spectra observed from the laser-induced plasma contain atomic and ionic spectral lines from all different species of the sample matrix. The methods described in this section are commonly used in different evaluations of LIBS data like in ref. [61] and [62]. If a LTE is assumed, the temperature of all these species in the plasma plume has to be the same.

As this is not given in general, the observation of the plasma is executed separately for the different species. A solid and quick method to estimate the plasma temperature is the so-called two-line approach using the ratio of two spectral lines with a sufficient gap between their upper energy levels. If the spectrometer is calibrated and the wavelength sensitivity of the detector is adapted, the intensity ratio I_1/I_2 is given by the transition probability A_i, statistical weight g_i, wavelength λ_i, and excited energy level E_i respectively as

$$\frac{I_1}{I_2} = \frac{\lambda_1 A_1 g_1}{\lambda_2 A_2 g_2} \exp\left(\frac{E_2 - E_1}{k_B T}\right). \tag{3.24}$$

Typical parameters for used materials in the experiments described are given in the appendix B in table B.2. Taking into account more than two spectral lines, it is possible to express the integrated line intensities $\bar{I}_{ki}$ of the optical thin plasma according to the concentration of the species C_s and an experimental factor F as

$$\bar{I}_{ki} = F C_s A_{ki} \frac{hc}{\lambda_{ki}} \frac{g_k}{U_s(T)} \exp\left(-\frac{E_k}{k_B T}\right). \tag{3.25}$$

Executing the logarithmic on both sides of the equation, a linear form is obtained as

$$\ln\left(\frac{\lambda_{ki}\bar{I}_{ki}}{hcA_{ki}g_k}\right) = -\frac{E_k}{k_B T} + \ln\left(\frac{FC_s}{U_s(T)}\right), \tag{3.26}$$

where the left side is a linear function ($y = mx + q_s$) of the upper energy level E_k of slope

$$m = -\frac{1}{k_B T} \tag{3.27}$$

and intercept

$$q_s = \ln\left(\frac{FC_s}{U_s(T)}\right). \tag{3.28}$$

With this method it is possible to estimate temperature and concentration of a given species in the laser-induced plasma. This is the basis of the CF-LIBS method, which can be used to estimate matrix conditions of the observed sample, where the concentration of the species is then calculated as

$$C_s = \frac{U_s(T)}{F} \exp\left(q_s\right) \tag{3.29}$$

and the factor F by determination of normalized sum of all observed species

$$\sum_i C_{s,i} = 1. \tag{3.30}$$

Other approaches, which are not further discussed here, are the determination of plasma temperature using a Saha-Boltzmann plot, which takes into account the relative spectral intensities of atomic and ionic lines, and a multi-element Boltzmann method that is using the spectral emission of different elements from the used sample.
This should give a necessary overview of methods to determine and estimate relevant plasma

parameters. As already mentioned, the usage of all those approaches is limited to the application of a LTE, which has to be treated with caution, especially in a plasma induced by a femtosecond laser. Moreover, in any case, self-absorption has an influence on the line shape and intensity. Self-absorption happens to be the effect that emitted photons from the inner part of the plasma are absorbed by particles in an outer shell. In the extreme case, where the plasma can be seen as a two layer system of high density and temperature in the core and low density and moderate temperature in the outer sphere, even self-reversal lines can be observed. Detected spectral lines then exhibit a dip of intensity in the center. Due to spectral shifts and broadening effects, this absorption line might have a narrower appearance then the original line from the plasma core. In the methods presented to determine plasma parameters, lines have to be chosen carefully by avoiding self-reversal ans self-absorption lines. Line asymmetry might be an indication for self-absorption in this context. To get an overview, the authors in ref. [63] describe the effects in more detail and point out the influence of those lines to CF-LIBS approaches.

3.5 Plasma-Facing Components (PFC)

In the experiments presented, the objective is to analyze metal tiles (often high Z metals like tungsten and tantalum) that were exposed to a pre-defined deuterium plasma. Plasma-facing components from a fusion device like ITER have to resist high particle irradiation defined by fluences (exceeding $10^{26}\,\mathrm{m}^{-2}$ ref. [64]) and flux ($10^{19} - 10^{23}\,\mathrm{m}^{-2}\mathrm{s}^{-1}$ ref. [10]) depending on the location observed and the plasma confinement mode. The targets used are exposed in similar conditions using the linear plasma device PSI-2 at IEK-4, Forschungszentrum Jülich. This device mimics the conditions in a fusion plasma as measured by Kreter et al. (2019, ref. [65]. A ring like pure deuterium plasma of $3 \times 10^{25}\,\mathrm{m}^{-2}$ total fluence and $2.9 \times 10^{21}\,\mathrm{m}^{-2}\mathrm{s}^{-1}$ maximum deuterium flux is interacting with the tiles that are arranged in a circle on a molybdenum mask (see fig. 3.7). The setup ensures that the polished and outgassed tiles are not sputtered with deuterium, but loaded by a reasonable deuterium amount in the bulk. Hereafter, a few concepts of deposition processes in these circumstances are explained and the techniques used to verify the total deuterium amount, besides LIBS, are described. Moreover, the microscopes used to analyze the laser-induced crater morphology are introduced.

3.5.1 Hydrogen-Isotope Inventory

As described above the lifetime of any upcoming magnetic confinement fusion experiment or reactor respectively depends on the resistance of all PFCs to the inevitable and sometimes required Plasma-Wall Interactions (PWI). According to Roth et al. (2008, ref. [64]), the most crucial issue is the retention of tritium (T) to the inner vessel walls. In particular, the process during Edge-Localized Modes (ELM) at the divertor plates, where the highest load to the material is expected, is crucial. The trapped tritium can be removed and recovered from the vessel walls in an extensive and time-consuming process, which needs to be avoided

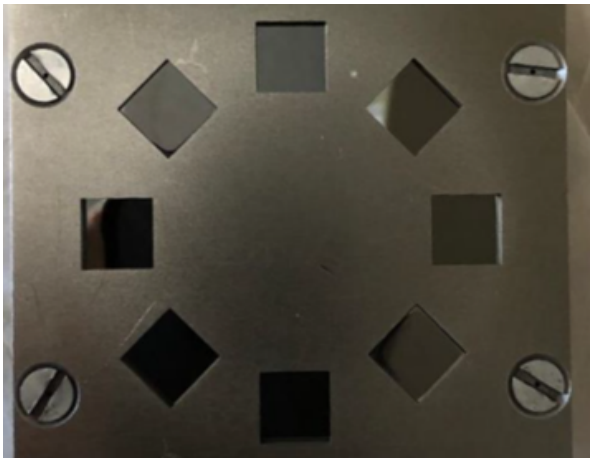

Figure 3.7: Eight tungsten tiles (9.9 mm × 9.9 mm × 5.1 mm) arranged in a circle on a molybdenum mask to be attached to the PSI-2 device at Forschungszentrum Jülich.

in a future operating power-plant.
Due to these difficulties tungsten and its alloys are proposed as PFC material. Its high melting point, high thermal conductivity coefficient and low ion sputtering yield make tungsten a suitable candidate for the inner vessel walls (see ref. [66]). Nevertheless, hydrogen isotope retention in those materials is still possible. Versatile studies using different plasma and particle sources, including some of the already mentioned fusion plasma experiments, give descriptions and predictions on the hydrogen-isotope inventory in those materials. A short collection of those are given in ref. [9]–[11], [66], [67]. This includes the implantation, trapping, diffusion and (co-)deposition. In high-Z materials like tungsten (Z=74) the dominant retention mechanism of hydrogen and its isotopes is trapping in lattice defects. Unfortunately, those defects are promoted by the high energetic particles and radiation from the fusion plasma. There are more effects to be considered: Co-deposition for instance is the option that the hydrogen isotopes are transported by a deposited layer to the wall, for example during deposition of Beryllium (Be) layers. Deposited tritium is then transported by a diffusion process to the whole PFC bulk, most likely with a decreasing concentration starting at the surface. A more detailed explanation of plasma wall interaction is left out at this point, as the thesis concentrates on the laser-induced diagnostic to detect those impurities. Anyway, one crucial point away is that the expected concentrations of hydrogen-isotopes in PFCs are on the order of a few at% (atomic percentage). Some other techniques to quantify these impurities apart from LIBS are described in the next paragraphs.

Nuclear Reaction Analysis (NRA)

Accelerated particles induce a nuclear reaction inside of the bulk material with the deposited hydrogen or deuterium atoms as described in ref. [68]. Similar to the depth analysis of Mayer et al. (2009) [69], the non-resonance reaction

$$^3\mathrm{He} + \mathrm{D} \rightarrow \alpha + \mathrm{p} + 18.353\,\mathrm{eV} \tag{3.31}$$

with high energy (6 MeV) Helium-ions is applied to the tiles observed and the protons emitted are detected. Depth information can be traced from the emitted proton energy spectra, while depth resolution is limited to a few micrometers.

Thermal Desorption Spectroscopy (TDS)

In TDS, one makes use of the temperature depended desorption process of particle retention in the lattice of a bulk material that is initiated in a defined temperature program. Here, the tiles are placed in ultra-high vacuum and usually heated with a linear temperature gradient. The partial pressure of escaping atoms and molecules is measured by mass spectrometry (e.g. Quadrupol or Time-of-Flight). From the composition of H_2, HD and D_2 the total amount of hydrogen isotopes retention in the observed tiles can be measured. The tantalum tiles used exhibit a deuterium number of 3.4×10^{19} and W of 3.8×10^{16}. This huge difference in the two materials is also found in ref. [70], where tantalum and tungsten were tested in a tokamak environment.

Laser-Induced Ablation - Quadrupol Mass Spectrometry (LIA-QMS)

Jannis Oelmann introduced in ref. [71] the use of a QMS to analyze the residual gas in an ultra-high vacuum chamber after laser ablation. Here, the tiles are irradiated by the picosecond laser described in chapter 3.1.4 with ablation rates down to 30 nm. With this method, the hydrogen content in tiles from W7-X could be analyzed *ex-situ* as shown in ref. [72].

3.5.2 Analysis of Surface Morphology

The surface and crater morphology are analyzed using a variety of techniques. The surface roughness (S_a) of the samples is given as

$$S_a = \frac{1}{N} \sum_{k=1}^{N} |z_k - u| \tag{3.32}$$

with the mean height u over N microscope positions. For surface irritations in the micrometer regime, the profilometer *Dektak 6M* can be used. For more detailed 3d images of the surfaces and craters either a confocal microscope located at the *Mirror Lab* (Forschungszentrum Jülich) or a scanning white light interferometer available at Lawrence Berkeley National Laboratory are used in this context. In the following part of this chapter, these two techniques are explained and characterized.

Confocal Microscopy

The microscope *STIL - Micromeasure 2* uses a tungsten lamp as a white light source in front of a pinhole. This point source is focused to the surface plane. Reflected light can then be imaged by the same lens to the detector, which is attached behind a pinhole of the same

size as the one in front of the light source. This guarantees that light out of focus is blocked and only "confocal" parts are detected. As diffraction is wavelength dependent, a chromatic sensitive sensor is used to determine the corresponding height value. A three dimensional image is generated by moving the microscope head along the observed surface. With this technique, a height resolution in the sub-micrometer regime can be achieved. The lateral resolution depends on the focusing objective used and the corresponding focus size. Here, spot sizes of $< 3\,\mu m$ and lateral positioning accuracy of $0.1\,\mu m$ are possible.

Scanning White Light Interferometry

The white light source in this configuration is imaged on the whole observation region on the sample, while a mirror in a reference arm provides light that can interfere with the reflected light from the surface in the detector plane. Interference can be observed when the distance of reference arm and probe arm are matching. Scanning the height by moving the objective up and down makes it possible to find this interference, which can be translated into a height information. The optical profiler *Zygo NewView 6000* utilized at the Laser technology group in Berkeley makes use of this principle. Analysis made with this device of laser processed tiles are presented in this work. The manufacturer promises depth resolution on a nanometer scale ($< 20\,nm$) and lateral resolution down to micrometer scale ($> 0.64\,\mu m$).

Chapter 4

Laser-Induced Ablation Threshold of Tantalum

In the following chapters of this thesis, LIBS results using different pulsed laser systems from nanosecond to femtosecond pulse duration are presented. In this context, tantalum and tungsten tiles are used as test devices loaded by deuterium, similar like the PFCs in a magnetic confinement fusion experiment. To get a deeper understanding of the materials and the characteristics of the laser material interaction, experiments are carried out and presented in this chapter that show the deviating ablation characteristic of different laser systems. These findings build a step towards a depth resolved LIBS experiment on PFCs of similar properties as the high-Z metal tantalum.

The described experimental setup and results in this chapter are following the studies in the joint publication "Laser-induced ablation of tantalum in a wide range of pulse durations" ref. [73] with the *Insitut für Energie- und Klimaforschung - Plasmaphysik IEK-4 at Forschungszentrum Jülich*, Germany and the *Key Laboratory of Material Modification by Laser, Ion and Electron Beams at Dalian University of Technology*, China. The presented results are supplemented by a numerical study on the sub-10-fs laser pulses with a self-developed Two-Temperature Model.

Getting into detail, first the preparation of the experiments is described, followed by the description of the evaluation process and the experimental results. While the experimental setup section is modified, due to a longer description of the laser systems in the Instruments and Methods chapter 3 in this thesis, the evaluation and results are taken from the original manuscript published in Applied Physics A in august 2020. In the summary and outlook part the comparison to a TTM simulation is added to give a more detailed view on the ablation process. These data are published in a contributed paper (ref. [74]) at the 47th Conference on Plasma Physics conference hosted by the European Plasma Society (EPS) 2020. All in all, this chapter gives an overview of the basic ablation processes using lasers of different pulse duration and wavelength in varying laser fluence and intensity regimes.

4.1 Experimental Setup

For the three experiments tantalum plates (2 mm × 50 mm × 50 mm) of 99.9% purity from the same charge made by *HMW Hauner GmbH & Co.KG* are used. The surface roughness is measured by confocal microscopy as $S_a = (0.7 \pm 0.3)\,\mu\text{m}$. The roughness is calculated as $S_a = \frac{1}{N}\sum_{k=1}^{N} |z_k - u|$ with the mean height u over N microscope positions. The tantalum tiles are attached in vacuum chambers of comparable pressure from 10^{-5} to 10^{-6} mbar. The ns- and ps-laser can easily be focused on the sample using a dispersive quartz lens. For the few cycle fs-laser a dispersive medium would change the pulse duration drastically due to the frequency dependent dispersion in the medium. For this reason, an off-axis parabolic mirror is used to focus the fs-laser instead. To lower the risk of damaging the laser system, the incident angle of the fs-pulse is 45° whereas the incident angle of the ns- and ps-laser is 0°, due to a lower damaging risk. Moreover, the crater size on the surface depends on the sample position with respect to the focal spot in the chamber. With different lens positions the crater size of the ns- and ps-laser is adjusted. In the chamber for the fs-laser, the sample table position can be adjusted. For all experiments three different sample positions are used to get a wide scan of laser pulse fluences. For this experiments, a reproducible laser pulse energy change is needed. Again a different proceeding is needed for the ns- and ps-laser compared to the fs-laser. For the ns-lasers *Brilliant EaZy* from *Quantel Laser* it is possible to change the timing of the flash lamp that pumps the active laser medium and the Q-switch that releases the pulse from the cavity. In a similar way one can choose different amplification steps in the amplifier of the ps-laser *EKSPLA PL2241*, where Nd:YAG rods are pumped by a flash lamp. A more detailed description is given in chaper 3.1. The energy of the ns-laser decreases nearly linear with the time delay Δt, while a higher amplification step of the ps-laser increases the pulse energy exponentially. To keep all the other pulse parameters like profile and pulse duration constant, a reflective attenuator consisting of different gold mirrors is used for the fs-laser to tune the pulse energy. For a good comparison of the different systems and to evaluate the ablation rate 200 shots at every position are used.

4.2 Evaluation Method

As described in detail in chapter 2.1.1, the different pulsed lasers need to be described by the same parameters. Here, a short recap of the laser fluence and intensity is given. For a flat-top beam profile the laser fluence, typically given in Jcm^{-2}, is calculated from the pulse energy E as

$$F = \frac{4E}{\pi D_0^2} \cdot \cos\Theta, \tag{4.1}$$

where D_0 is the beam diameter at $1/e^2$ of the maximum intensity in the interaction plane and Θ is the incidence angle. To compare this with a Gaussian shaped beam profile, a factor 2 is included to take the smaller effective area into account. The intensity is given as $I = F/\Delta\tau$, with the pulse duration $\Delta\tau$ (FWHM of laser intensity in time). Note that F is an integrated

quantity and therefore gives a measure for the total effect induced by a laser pulse, whereas I is a temporal quantity which describes momentary effects.
One aim of this investigation is to find the so called threshold fluence F_{th}, which is the minimum laser pulse energy per area required for material removal from the surface from a single laser pulse. Moreover, also the threshold intensity I_{th}, the minimum laser power per area needed for ablation, is of interest when observing the influence of high electromagnetic fields. Both parameters are examined, because they become important in different physical regimes. The laser fluence has its relevance in the case of thermal processing of the used samples. Here, it is referred to the process of ns-ablation or high repetition of ultra-short pulses on optical components. Intensity is consulted when the ablation process is dominated by the basic electro-magnetic field interaction with the used material. Here, single shot ablation with ultra-short laser pulses are of interest.
From the crater depth variation with laser pulse energy the threshold fluence can be retrieved by

$$L = \beta^{-1} \ln\left(\frac{F}{F_{th}}\right), \tag{4.2}$$

where L is the ablation depth per pulse called ablation rate introduced by ref. [22]. A similar dependence can be observed with respect to a threshold intensity I_{th} as

$$L = \beta^{-1} \ln\left(\frac{I}{I_{th}}\right). \tag{4.3}$$

Note that β^{-1} is a numerical fitting parameter that has the meaning of an effective penetration depth from the observed material. In the ps- to fs- pulse duration regime this parameter can be set to the optical penetration depth α^{-1} as carried out in ref. [75] for the case of a molybdenum target. The logarithmic dependence presented in (4.2) and (4.3) has its origin in the assumption of a laser source term in the heat diffusion equation that transfers its energy into the material with an exponential decay constant β^{-1}. For the tantalum sample, the optical penetration depth is calculated using

$$\alpha^{-1} = \frac{\lambda_0}{4\pi \cdot \kappa}, \tag{4.4}$$

with the extinction coefficient κ calculated in ref. [76]. For the ns-laser, β^{-1} can be seen as a combination of optical and thermal penetration depth.
The crater depth has been evaluated via white light confocal microscopy (*Micromeasure 2* from *STIL*) and the ablation rate is determined as the ratio of maximum crater depth and number of laser pulses at each position. Tani et al. (2018, ref. [77]) found a lower ablation rate for the early laser pulses on the polished surface at low fluences with a fs-laser on copper. The resulting offset is neglected here, due to the high surface roughness of the target in the first place.

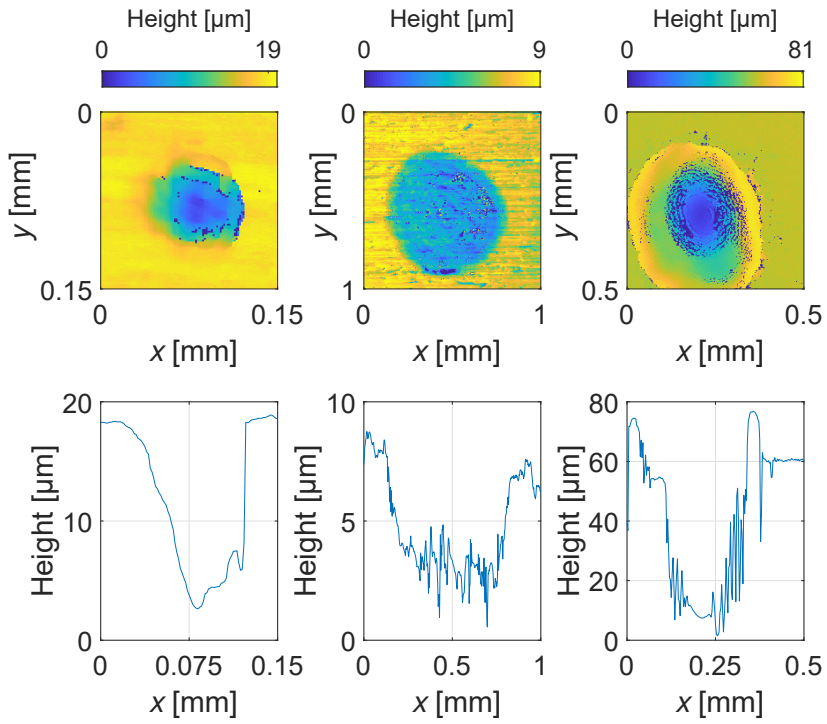

Figure 4.1: Comparison of raw data from the different craters after the interaction with 200 laser pulses of pulse duration and fluence (left) $\Delta\tau = 8.5\,\mathrm{fs}$, $F = 2.4\,\mathrm{J/cm^2}$, (middle) $\Delta\tau = 35\,\mathrm{ps}$, $F = 6.3\,\mathrm{J/cm^2}$ and (right) $\Delta\tau = 5\,\mathrm{ns}$, $F = 34\,\mathrm{J/cm^2}$ are shown. In the first row the confocal microscope data in a false color plot and in the second row cross sections from the craters center are given. The figure is taken from ref. [73] and licensed under CC BY 4.0.

4.3 Experimental Results

To compare the different crater morphologies that are generated by laser pulses of different pulse durations fig. 4.1 shows raw data from three craters in 2D false color plots and their cross section respectively (averages of 11 curves in the center of the crater). The morphology of these three craters reflects characteristic properties for the individual laser systems: The fs-crater on the left side exhibits an elliptical shape due to the 45° incident angle onto the target. Around the ns-crater on the right side a solidified corona of material can be observed. In all cases (relatively low fluences) the crater diameters are comparable to the laser beam diameters D_0.

From these raw data the crater depth is determined using some corrections beforehand. The signal from the confocal microscope exhibits defects where the recorded intensity from the reflected light from the surface is insufficient. These defects result in "unphysical" height values close to zero. For the depth analysis the mentioned defects were replaced by the mean value of the surrounding data points and the data was numerically leveled where it was necessary. The depth is calculated by the difference of the mean surface height and a value from the craters center. Here, 1000 to 20000 data points, depending on the resolution, are used. Due to the cone like depth shape of the fs- and ns- craters, this value is given as the minimum of

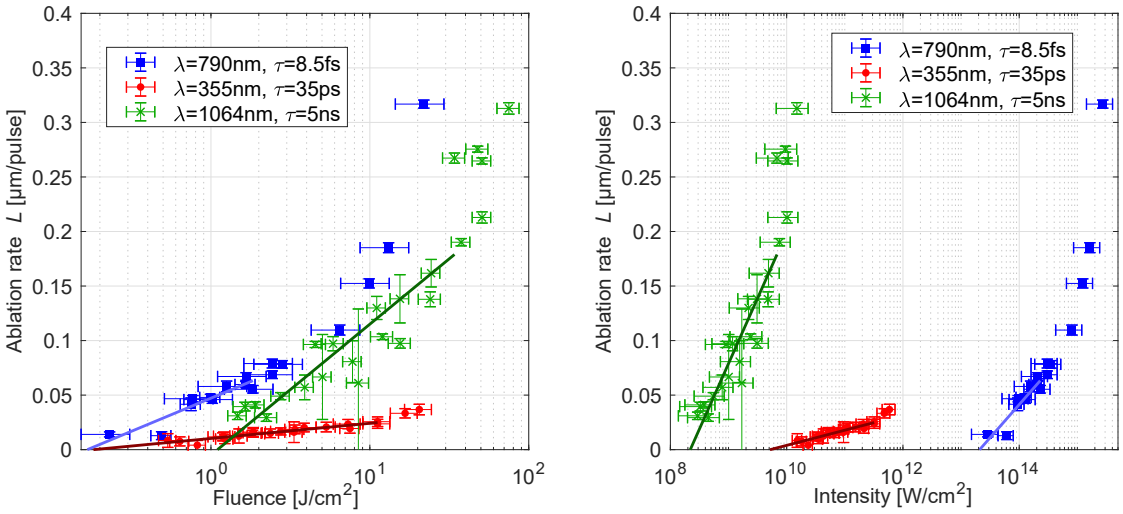

Figure 4.2: (left) Ablation rate L with respect to the used laser fluence F and (right) ablation rate with respect to intensity with logarithmic x-axis are shown for three different laser systems. Here, the ■ marker defines the femtosecond laser, • the picosecond laser and × the nanosecond laser measurement. The figure is taken from ref. [73] and licensed under CC BY 4.0.

$\Delta\tau[s]$	E [mJ]	λ_0[nm]	F_{th}[J/cm^2]	I_{th}[W/cm^2]	β^{-1}[nm]	α^{-1}[nm]
$5 \cdot 10^{-9}$	280	1064	1.1 ± 0.1	$(2.2 \pm 0.5) \cdot 10^8$	52 ± 2	13
$35 \cdot 10^{-12}$	46	355	0.18 ± 0.10	$(5.2 \pm 3.0) \cdot 10^9$	6.0 ± 0.3	11
$8.5 \cdot 10^{-15}$	1.0	790	0.17 ± 0.05	$(2.1 \pm 0.5) \cdot 10^{13}$	26 ± 1	16

Table 4.1: Laser parameters for the ablation experiments from the three different systems and determined ablation threshold fluence F_{th}, intensity I_{th} and effective penetration depth β^{-1} compared to calculated optical penetration depth α^{-1} depending on used laser pulse duration $\Delta\tau$ and wavelength λ_0 are shown. Content is taken from ref. [73] and licensed under CC BY 4.0.

the measured height profile. The ps-laser generates cylinder like shapes in the center of the craters. That is why the depth value is calculated as a mean value from the craters center. Figure 4.2 shows the measured ablation rate with respect to laser fluence and intensity. Table 4.1 gives the resulting threshold and effective penetration depth values from the numerical fitting process for the different laser systems with 17, 22 and 23 craters for the fs-, ps- and ns-laser respectively. Here, the ablation rate with respect to the laser fluence is plotted on a logarithmic x-axis shown in fig. 4.2 (left). Smaller ablation rates are observed with decreasing laser fluence. In fig. 4.2 (right) the ablation rate is plotted with respect to the laser intensity on a logarithmic x-axis. The errorbars correspond to the uncertainty of the laser pulse energy measurement caused by the powermeter of ±5%. This is linked to the uncertainty of the beam diameter in the interaction plane of ±3 µm. The uncertainty of the craters depth is caused by the surface roughness at each individual confocal microscope position. The pulse-to-pulse fluctuations of the laser pulse energy are ignored in each case, because of the high

number of pulse repetitions (200) used for one crater. Using fits (solid lines) on the data given by equation (4.2) and (4.3), threshold fluence and intensity result from the best fitting parameters. Graphically this values can be observed as the roots and β^{-1} as the slope of the fitting functions. Note that the used fitting function is only valid in a low fluence regime that depends on the pulse duration. For the fs-laser the fit was made at fluences below $1\,\mathrm{Jcm^{-2}}$, for the ps-laser the limit was $10\,\mathrm{Jcm^{-2}}$ and within the ns-interaction $35\,\mathrm{Jcm^{-2}}$ turns out to be a valid limit. At this point thermal penetration becomes more relevant and the slope of the logarithmic function rises.

To observe the influence of thermal and optical penetration during the interaction the effective penetration depth β^{-1} is compared to the optical penetration depth α^{-1} from equation (4.4). The wavelength dependent values are 16 nm for the fs-, 13 nm for the ns- and 11 nm for the ps-laser. Note that the wavelength dependence of the ablation process can be observed in the deviating slope of the ps-ablation and the fs-ablation curve. The resulting effective penetration depth of the ps- and fs-ablation differs by a factor less than 2 from the optical penetration depth α^{-1}. For the ns-ablation, however, this factor is 4, which indicates the high influence of thermal penetration that dominates this process. This result and the morphology comparison show the high thermal impact of ns-laser matter interaction. While the fs- and ps-laser pulses produce craters with smooth edges, the ns-craters exhibit a ring of solidified molten material higher than the surface around the hole. This expulsion of the melt lowers the precision, when the data from the ablation yield shell be used for information on the material content in the target as in the mentioned project on the plasma-facing components. The timescale of the energy transfer between free electrons and the lattice is significantly longer than the pulse duration of these ultra-short laser pulses, which results in a considerably lower HAZ [78].

From the threshold analysis decreasing threshold fluence from $1.10\,\mathrm{J/cm^2}$ for the ns-laser to $0.17\,\mathrm{J/cm^2}$ for the fs-laser can be observed. The threshold intensity increases from $2.2 \cdot 10^8\,\mathrm{W/cm^2}$ to $2.1 \cdot 10^{13}\,\mathrm{W/cm^2}$ with shorter pulse duration. Here, the characteristics of the different interaction regimes are observed. The process is dominated by the high electromagnetic field in the ultra-short case (fs- and ps-ablation) and the minimum energy needed for ablation decreases. For fs- and ps-ablation the same threshold fluence value is observed within the uncertainty. This can be related to the time scale of interaction that is in both cases before the breakdown in the material occurs. Note that the deviating laser wavelength might also have an influence here. This phenomenon was also investigated by Genieys et al. (2020, ref. [79]) where the ablation threshold fluence for aluminum and tungsten was observed to be equal for sufficiently short laser pulses. Another work on this phenomenon was made by Gamaly et al. (2002, ref. [80]). On the one hand, this observation can be expanded up to a ps-limit from the shown investigations on tantalum. On the other hand, significantly higher intensity is needed with the fs-laser, namely up to five orders of magnitude more compared to the ns-laser. Other studies from the last years on tantalum offer deviating results for 80 fs, in ref. [81] ($F_{th} = 0.31\,\mathrm{J/cm^2}$), and 3 ns in ref. [82] ($F_{th} = 0.71\,\mathrm{J/cm^2}$). Note that thin Ta films deposited onto fused quartz can have different optical properties compared to bulk Ta.

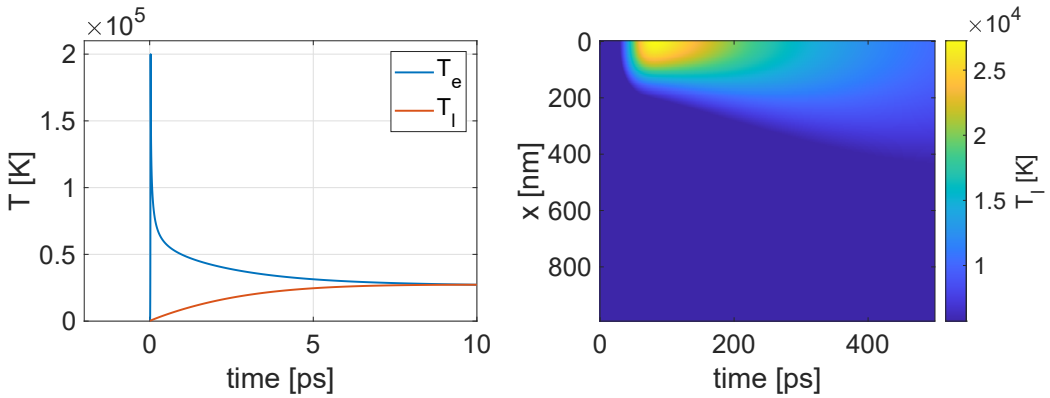

Figure 4.3: (left) Output of a TTM simulation on tantalum ($F = 6.12\,\mathrm{J/cm^2}, \Delta\tau = 8\,\mathrm{fs}, \lambda_0 = 790\,\mathrm{nm}$) with the maximum electron and lattice temperature (T_e and T_l) in the first 10 ps. (right) Contour plot of the lattice temperature on the x grid over the whole simulation time. Shown is the laser heating and ensuing cooling process including the thermalization of electron and lattice subsystem after $\sim 10\,\mathrm{ps}$.

4.4 Summary and Outlook

Before the experimental findings from this chapter are summarized, a numerical approach is presented that can be used to predict the ablated volume by given material and laser parameters. In this case the ablation threshold of the femtosecond laser used in this study is compared to values determined by the presented numerical model.

Predictions on the ablated volume by the used ultra-short laser pulses can be made by the Two-Temperature Model (TTM) that solves the coupled differential equation in (2.20) including the thermophysical properties described in appendix A. Figure 4.3 shows the typical output of an one dimensional TTM simulation on tantalum. The applied laser has similar parameters as the PHASER used in the shown ablation experiment. In the first few femtoseconds only the electron subsystem is heated. The energy transfer to the lattice happens on a timescale of up to 10 ps. Different approaches to estimate the ablation depth can be used on this data. The maximum lattice temperature depending on the used laser fluence can be calculated. When the boiling temperature ($T_{b,\mathrm{Ta}} = 5731\,\mathrm{K}$) or the temperature at the critical point ($T_{c,\mathrm{Ta}} = 13400\,\mathrm{K}$) are assumed as ablation limits, the maximum ablation depth can be calculated from the simulation data. Some publications like ref. [42] even suggest an even higher separation temperature T_{sep} defined by the adiabatic cooling of the heated system after rapid heating above the critical temperature as

$$T_{sep} = \left(\frac{\rho_0}{\rho_c}\right)^{3/2} T_c. \tag{4.5}$$

The critical density ($\rho_{c,\mathrm{Ta}} = 3.32\,\mathrm{g/cm^2}$) and temperature are taken from ref. [83]. Figure 4.4 (right) shows the maximal ablation depth assuming these temperatures to be sufficient to ablate the material. The left part of the figure gives the time evolution of the high temperature edge along the grid. With this approach the ablation threshold fluence can be estimated

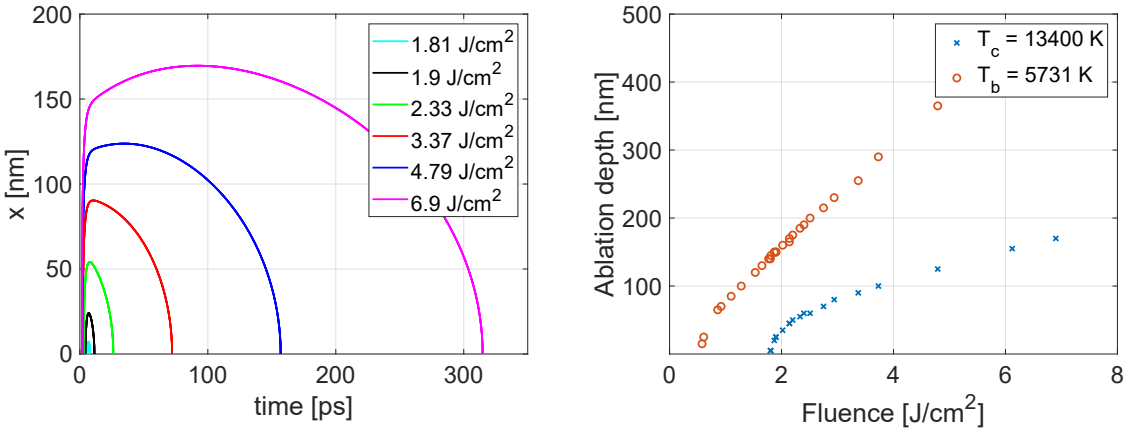

Figure 4.4: (left) Contour plot of the critical temperature T_c along the sample depth x with respect to simulation time for different laser fluences. (right) Ablation depth calculated by the depth of critical temperature and boiling temperature T_b. Figure content taken from ref. [74].

as $F_{th} \approx 0.58\,\mathrm{J/cm^2}$ for boiling or $F_{th} \approx 1.81\,\mathrm{J/cm^2}$ for reaching the critical point. As expected, these values are higher than the measured threshold of $0.17\,\mathrm{J/cm^2}$. This can be an indication for an ablation process that is governed by a non-thermal melting characteristic, because the separation temperature might decrease due to the high electron temperature that surrounds the lattice subsystem. Moreover, the reflectivity is a limiting factor of this theoretical approach, as the comparably rough surface structure could lead to completely different absorption mechanisms.

The described laser ablation on the high-Z material tantalum reveals the expected logarithmic dependence of ablation rate with respect to the laser pulse energy or power per area respectively for all used pulse durations and wavelengths. By observing the craters morphology and comparing the measured penetration depth to the optical penetration depth α^{-1} the high thermal impact of the ns-laser ablation is confirmed. By these concrete examples of laser ablation the necessity of distinction between threshold fluence and intensity is pointed out. Moreover, by presenting these three pulse duration regimes on the same material the best system for the diagnostic application can be assumed. This advantages can be used, when LIBS signals from first-wall material in the fusion plasma devices are generated. Here, a high depth resolution is a relevant factor. It is shown that lowering the pulse duration offers the opportunity for high resolution material analysis. With this evidenced knowledge, further steps towards a fs-laser based LIBS diagnostic for PFCs in fusion devices are describe in the ensuing chapters.

Chapter 5

LIBS using sub-10-fs Laser Pulses in Vacuum

In this chapter, the development of a LIBS setup with a laser of sub-10-fs pulse duration in a vacuum environment is described. In particular, time resolved measurements on the plasma expansion of different materials excited by these pulses are evaluated. Both plasma imaging, and optical emission spectroscopy are executed to display the characteristics of this state of matter under these circumstances. The evaluation of the experiments make a step towards the objective of this thesis, to give an assessment on the applicability of this kind of laser source as a detection system with high depth resolution on PFCs.
In the first section, the laser-induced plasma expansion dynamic of tantalum is detected by a time resolved imaging system for varying laser parameters. In the second section, a spectrometer is used to detect the temporal optical emission of copper, tantalum, and tungsten, and a technique to enhance the plasma "brightness" is introduced.

5.1 Laser-Induced Plasma Expansion Dynamics of Tantalum

One important step to establish a LIBS setup with the correct dimensions of the optical correction system is to determine the size of the emitting source. Here, the source is a fast expanding plasma plume that is induced by the ultra-short laser pulse provided by the PHASER system. Furthermore, the temporal evolution of those plasma plumes is of interest to be able to capture the total temporal and spatial dynamic of the process.
Below, a plasma plume of tantalum under these circumstances is detected to extract spatial and temporal information on the plasma formation in vacuum. The results presented were partially published in a paper contributed to the annual conference of the European Plasma Society (EPS) in 2020 (see ref. [74]). Parts of the experimental setup section are taken directly from this contribution. Subsequent content splits up into a description of the experimental setup, the presentation of some results including relevant information for a LIBS setup, and a conclusion.

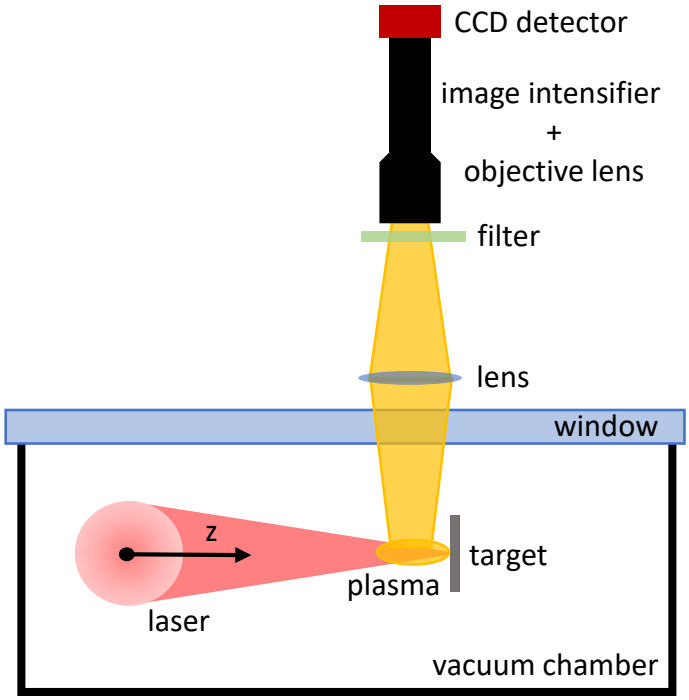

Figure 5.1: Schematic side view of the experimental setup in the vacuum chamber. The laser is focussed by a 90° off-axis parabolic mirror ($f = 127\,\text{mm}$) onto the target and the plasma emission is detected by an optical collection setup including an image intensifier and a CCD camera.

5.1.1 Experimental Setup

Figure 5.1 represents the experimental setup in a schematic side view on the vacuum chamber. The ultra-short laser pulse with pulse duration of 8 fs is focused onto the target, which is movable in three dimensions to be able to change the position with respect to the focal spot of the laser and to use unperturbed positions for each laser pulse. The induced plasma plume is detected through the glass window by an optical setup consisting of a lens ($f = 100\,\text{mm}$), image intensifier including an objective lens, and a CCD detector. Here, a gated optical system is realized by a CCD camera (*Allied Vision*) attached to a micro-channel plate image intensifier (type II18G, *Lambert Instruments*) equipped with an objective lens. The plasma plume is observed tangential to the sample surface. The sample used is the same tantalum tile that is used for the ablation experiment in chapter 4. The MCP gate delay of 100 ns to 30 µs are used to observe the temporal evolution of Ta-I spectral lines and continuum emission of nanopartincles. A bandpass filter (bandwidth 300 nm to 700 nm) to protect the camera from most of the scattered laser light when the delay is not yet adjusted properly.

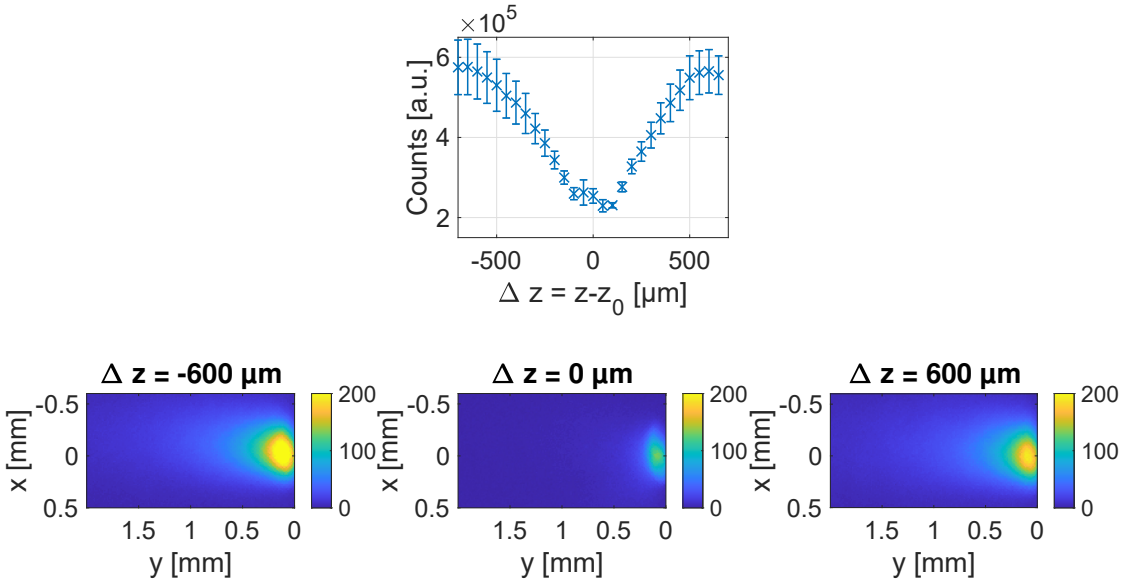

Figure 5.2: (top) Sum over all camera counts in the plume area plotted with respect to the distance to the focal position z_0. (bottom) Images with an intensifier gate width of 20 µs of tantalum plasma plume as an arbitrary unit pseudo-color plot.

5.1.2 Experimental Results

In the beginning, the optimal z-position (distance between focusing optic and target) has to be found. Here, positive values are positions behind the focal point (divergent part of the laser beam). In fig. 5.2 a scan along the z-axis from $-800\,\mu m$ to $650\,\mu m$ and images of three selected positions are given. Note that the pulse energy of the incoming laser is equal for each position, but the beam diameter is changing which results in a fluence change in the range of $5\,Jcm^{-2}$ to $4000\,Jcm^{-2}$. The counts detected are summed up over the whole area of detection for five averaged snapshots for each z-position. The setup operates with a gate width of 20 µs to capture the whole evolution of the plasma. It is notable that the plasma plume signal drops rapidly around the focal point and the optimal positions with the "brightest" plasma emission might be around 600 µm away from it. In the next step, the gate width is reduced and the temporal evolution of the plume is investigated to determine, if this "brightness" is a decent indicator for a strong LIBS signal.

Next, the temporal evolution of the plasma emission at this "optimal" z-position $\Delta z = 600\,\mu m$ from the expanding plume is detected with a reduced gate width of 100 ns using the same filter. Here, the laser exhibits a fluence of around $F = 11\,Jcm^{-2}$. Figure 5.3 depicts the detected plasma in five different time-frames. Apparently, the plasma plume is divided into two parts: A fast expanding plume persisting in the first two time-frames up to 200 ns after the laser plasma interaction and a slow plume following and detectable up to a few µs later. An analysis of these two stages shows that a distinct difference in velocity can be observed between $5 \times 10^3\,ms^{-1}$ and $5 \times 10^2\,ms^{-1}$. This finding can be compared to the work of Harilal et al. [84], who observed the expansion of tungsten plasma induced by femtosecond pulses

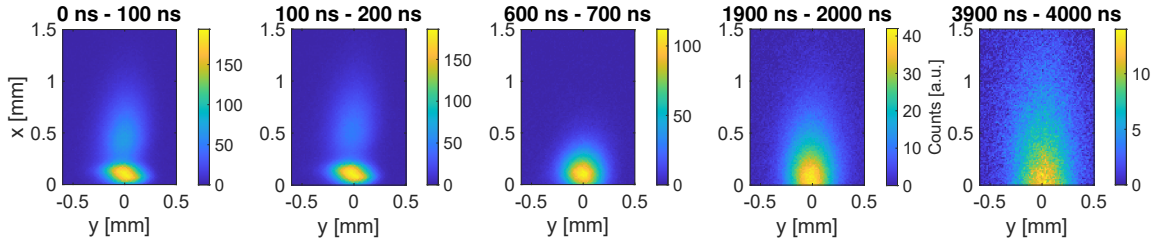

Figure 5.3: Selected snapshots of the temporal evolution of tantalum plasma plume induced by a 8 fs laser pulse detected by the image intensifier with gate width of 100 ns.

in more detail. The group observed two plumes, the first one persisting during 400 ns after the interaction with the $F = 8\,\mathrm{Jcm}^{-2}$, 40 fs laser pulse and the second one up to 40 µs longer. Spectral analysis of the two phases brought evidence to claim that the second plume contains continuum radiation of expanding nanoparticles and the first plume atoms and ions. Compared to their findings, the velocity of the two phases from the observations on the tantalum sample presented are on the same order of magnitude, which indicates that also on the tantalum target the expanding plasma is divided into a relevant time-frame for LIBS including atomic and ionic spectral lines, and a way slower nanoparticle time-frame. To prove this claim, the time resolved optical emission spectrum has to be detected. Even though observing this effect on two different materials with comparable atomic number Z seems to be reasonable and might be a characteristic for laser ablation of high-Z materials.

5.1.3 Discussion

For the application of a LIBS setup with a sub-10-fs laser it is essential to know the plasma expansion behavior after the interaction. With the gated plasma image experiment it is possible to predict a time frame in which to observe characteristic spectral lines of the expanding tantalum plasma in order to avoid the dominant continuum radiation caused by the emerging nanoparticles and the hot sample surface. The first prediction for a reasonable time-frame after the laser surface interaction are the first 200 ns.
In the next section the same laser pulses are used in a LIBS setup with the option to enhance the signal detected using the pre-pulse module introduced in chaper 3.2. Moreover, the temporal evolution of optical emission of a tungsten and tantalum plasma is presented that intends to prove the claims about plume dynamics presented in this section.

5.2 Sub-10-fs LIBS

Following the findings from the previous section, in the next step spectral information are added to the plasma plumes observed. The LIBS results presented are discussed directly with the intention of finding a way to enhance the spectral line intensity. For this, the pre-pulse module presented in chapter 3.2 is introduced as a possible way to increase the characteristic line persistence when being executed on different metals.

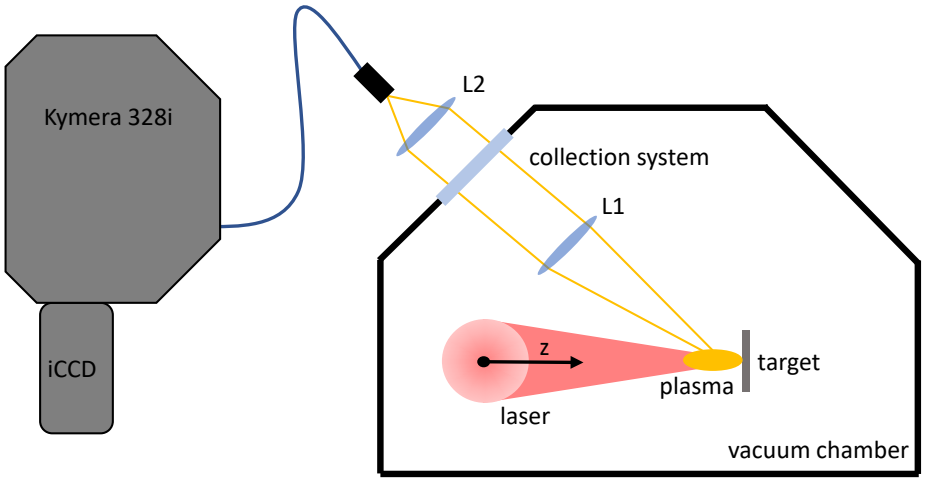

Figure 5.4: Side view of experimental setup for LIBS with the PHASER system in a vacuum chamber. The laser is focused by a parabolic mirror onto the target. The optical emission of the plasma expanding perpendicular to the targets surface is detected by an optical collection system using lens L1 and L2. The collected light is detected in a Czerny-Turner spectrometer and an iCCD camera.

The realization of a LIBS setup using the sub-10-fs laser pulses generated by the PHASER system operating at the Institute of Laser and Plasma Physics (ILPP), Heinrich Heine University (HHU) in Düsseldorf first became possible with the new optical spectrometer provided by the German Research Foundation (ger. Deutsche Forschungs-Gemeinschaft DFG). The spectrometer has to be a compromise between resolution and sufficient light throughput. However, a broader spectral range was necessary to finally observe time resolved spectral emission dynamics of plasma induced by these ultra-short laser pulses, which reveals interesting insights to the characteristics of the interaction mechanism.

5.2.1 Experimental Setup

As described before, the broadband Ti:Sa laser with compressed pulses of less than 8 fs pulse duration is used to drive the plasma generation on different metals. In this configuration, the pre-pulse stage is used to study the influence of a pre- ignited surface on the laser material coupling. From this, the resulting optical emission enhancement from the ensuing plasma is detected.
The target material is installed in a vacuum chamber of 5×10^{-6} mbar ambient pressure on a 3D translation stage. The broadband near infrared laser pulses are focused by an off-axis parabolic mirror of $f = 127$ mm focal length to the 45° tilted surface. With a constant pulse energy of 460 µJ in the main arm of the pre-pulse module, the laser fluence can be varied by moving the target along the propagation direction of the laser and is changed from 5 $\mathrm{Jcm^{-2}}$ to 4000 $\mathrm{Jcm^{-2}}$ in this study. Note that a pre-pulse is used with 1 % of the main pulse energy as described in Chapter 3.2. Operating the laser at different days includes slightly different

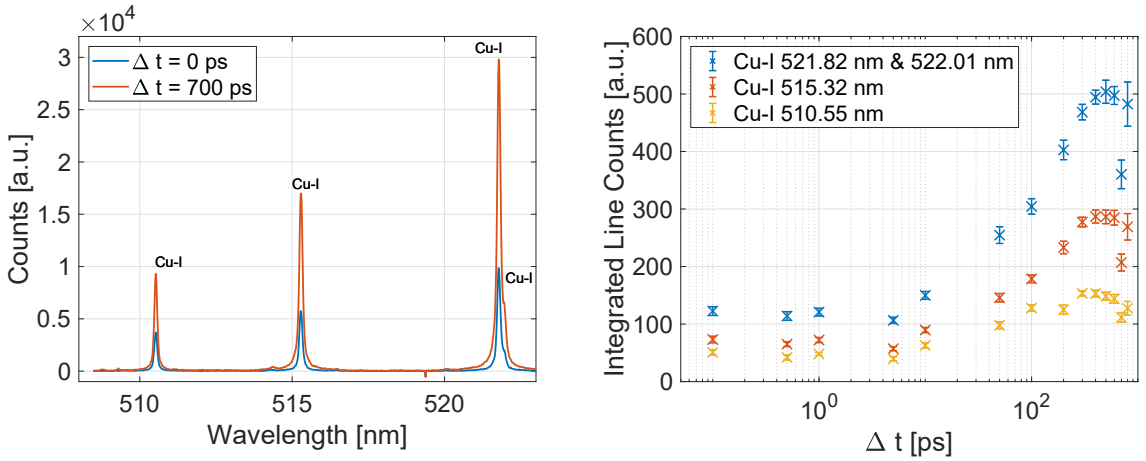

Figure 5.5: (left) Cu-I lines captured by the spectrometer with grating 2000 l/mm, gate width of 500 ns directly after the interaction with pre-pulse delay Δt. (right) integrated counts of the observed lines with respect to Δt. The laser fluence of the main pulse is given as $F_2 = 48\,\mathrm{Jcm^{-2}}$ and the pre-pulse $F_1 = 0.60\,\mathrm{Jcm^{-2}}$.

settings on the hollow fiber, which results in a pulse duration between 6.5 fs and 8 fs. It results in laser intensities in the range of 10^{14} to $10^{18}\,\mathrm{Wcm^{-2}}$ for the main- and 10^{12} to $10^{16}\,\mathrm{Wcm^{-2}}$ for the pre-pulse respectively.

For the LIBS experiment, the *Andor* intensified CCD *iStar340* is used to observe the collected time dependent plasma emission with 5 ns to 500 ns gate widths. Spectral information is gained by the *Andor Kymera328i* spectrograph with four different gratings optimized for the visible spectral range. The plasma emission is collected by two optical aligned $f = 100\,\mathrm{mm}$ fused quartz lenses. The system is arranged in a 45° angle to the interaction region and indicates to the early stage plasma close to the target surface. The experimental setup in the vacuum chamber is schematically shown in fig. 5.4. Here, the optical collection system consisting of two lenses L1 and L2 is tilted by 45° out of the interaction plane, parallel to the incoming laser pulse.

In the experiments presented different materials are used. For the beginning, an intensive study on polished copper is presented as the ionic and atomic lines are clearly visible with the setup shown. Furthermore, it is discovered, whether the findings are transferable to the high-Z materials tungsten and tantalum and the influence of a pre-pulse is used to enhance the hydrogen emission. The temporal dynamic of the expanding plasma plume from high-Z materials claimed in the previous chapter is investigated by the detection of the emitted characteristic spectra and its persistence.

5.2.2 Experimental Results

LIBS on Copper

First of all, the atomic and ionic lines of copper (Cu-I and Cu-II) are observed for different laser intensities. This study is focused on the four atomic lines Cu-I at 510.55 nm, 515.32 nm,

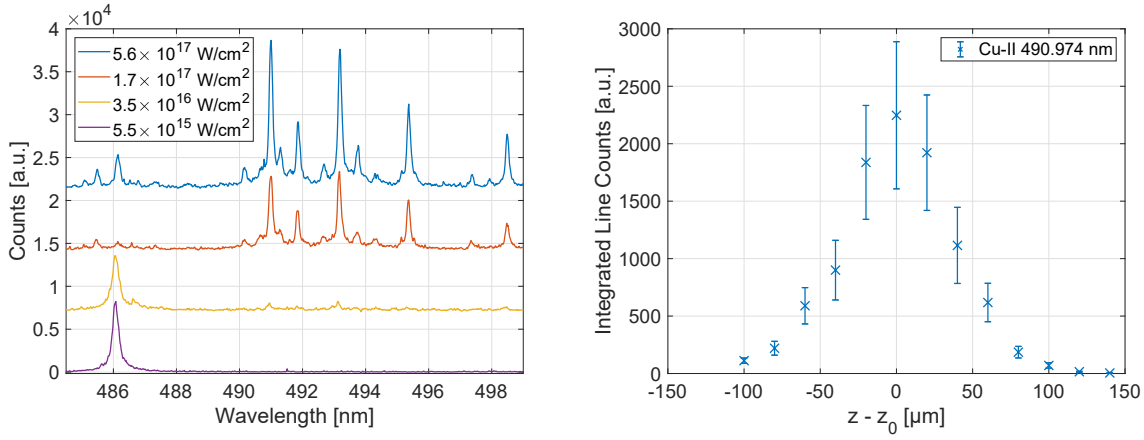

Figure 5.6: (left) Cu-II lines captured by the spectrometer with grating 2000 l/mm, gate width of 500 ns directly after the interaction without a pre-pulse for different laser intensities I. An offset of 6000 counts is added between the plots for a better overview. (right) Integrated counts of the Cu-II line with respect to the target position z along the beam-waist with focal position $z = z_0$. The laser intensity of $3.5 \times 10^{16}\,\mathrm{Wcm^{-2}}$ corresponds to a position 100 µm behind the focus.

521.82 nm and 522.01 nm and three ionic lines Cu-II at 490.97 nm, 493.17 nm and 495.37 nm. Note that all shown spectra in the study on copper are averaged over 20 detected signals from single pulse laser irradiation. For the observation, a relatively short gate delay between the interaction and the snapshot is chosen. A gate width of 500 ns captures the whole plasma emission process. In the experiments presented the pre-pulse delay Δt is changed and its influence is investigated for different laser fluences.

Initially the laser fluence of the pre-pulse is set close to the theoretical ablation threshold of copper $F_{th} \approx 0.64\,\mathrm{Jcm^{-2}}$. This threshold can be approximated by the equation following Lickschat et al. (2020, ref. [85]) as

$$F_{th} = \frac{H_v \cdot \rho}{(1 - R(\lambda)) \cdot M \cdot \alpha(\lambda)}. \tag{5.1}$$

The material parameters necessary for the bulk copper are given as: Evaporation enthalpy $H_v = 313\,\mathrm{kJ/mol}$, density $\rho = 8.92\,\mathrm{g/cm^3}$, molar mass $M = 63.55\,\mathrm{g/mol}$ and wavelength dependent values of reflectivity $R = 0.94$ and optical penetration depth $\alpha = 1.14 \times 10^6\,\mathrm{cm^{-1}}$ at central wavelength $\lambda = 790\,\mathrm{nm}$ [76].

Figure 5.5 shows the enhancement characteristics of four observed Cu-I lines in the visible spectral range for different pre-pulse delay stage positions. On the left side the spectrum is shown for no pre-pulse delay and almost the maximum delay possible, and the right side provides the integrated line intensity of the four lines with respect to the delay Δt used on a logarithmic axis. The errorbars result from statistical fluctuations of the 20 detected spectra for each data point. Note that the two lines at 521.82 nm and 522.01 nm are treated as one line due to the spectrometer resolution limit. The integrated intensity is evaluated by the embedded area within the FWHM of the corresponding peak. According to this measurement,

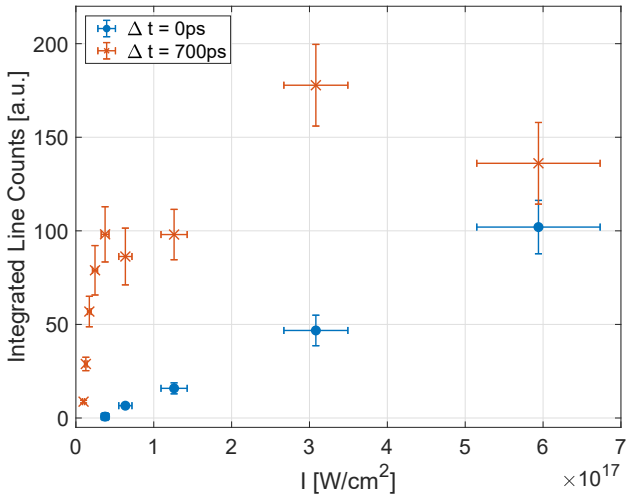

Figure 5.7: Line intensity of Cu-II line at 490.974 nm for two different inter-pulse delays of pre- and main pulse depending on main pulse intensity I.

the signal is enhanced by a factor of four when an inter pulse delay of more than 300 ps is chosen. Apparently, the enhancement factor starts to grow after 50 ps and saturates with the use of a 600 ps delay. The laser fluence of the pre-pulse in this setup ($F = 0.60\,\mathrm{Jcm^{-2}}$) is slightly below the theoretical ablation threshold calculated by equation (5.1); but still ablation and plasma creation can be possible as it is just a theoretical limitation and other studies revealed even lower ablation threshold fluences for comparable lasers (see for example ref. [86]: $F_{th} \approx 0.45\,\mathrm{Jcm^{-2}}$). Moreover, a temperature rise can be observed from approximately 9200 K without a pre-pulse and 10000 K when the signal is enhanced by a pre-pulse of $\Delta t = 700$ ps. The estimation of the electron temperature is executed by the Boltzmann Plot method using two atomic lines at 510.55 nm and 515.32 nm. The corresponding optical parameters like transition probability, statistical weight and upper energy level of the excited atomic state are taken from the National Institute of Standards and Technology (NIST) database ref. [87] and are shown in table B.2 in appendix B.

Before the influence of the pre-pulse is demonstrated, fig. 5.6 presents an laser intensity dependent study on excitation of ionic copper lines. Here, the laser intensity dependent ionic emission lines of copper are shown by adjusting the distance between the focusing optic and the target. The position $z - z_0$ indicates the position of the target with respect to the focal point. Compared to the work of Anoop et al. (2016, ref. [86]), it is likely that the shorter pulse duration in our case (8 fs compared to 40 fs) and the associated lower pulse energy necessitate a way higher intensity to initiate the ion excitation. The group found a detection limit for the ion signal as $F < 10\,\mathrm{Jcm^{-2}}$. This corresponds to an intensity of $2.5 \times 10^{14}\,\mathrm{Wcm^{-2}}$, which is two orders of magnitude lower than the intensity limit that the data presented provide, but only one order of magnitude in laser fluence difference. Figure 5.7 gives a view on the pre-pulse influence on the ionic lines. Here, the integrated counts of the Cu-II line at 490.974 nm are plotted with respect to the main pulse laser intensity used for two different inter-pulse

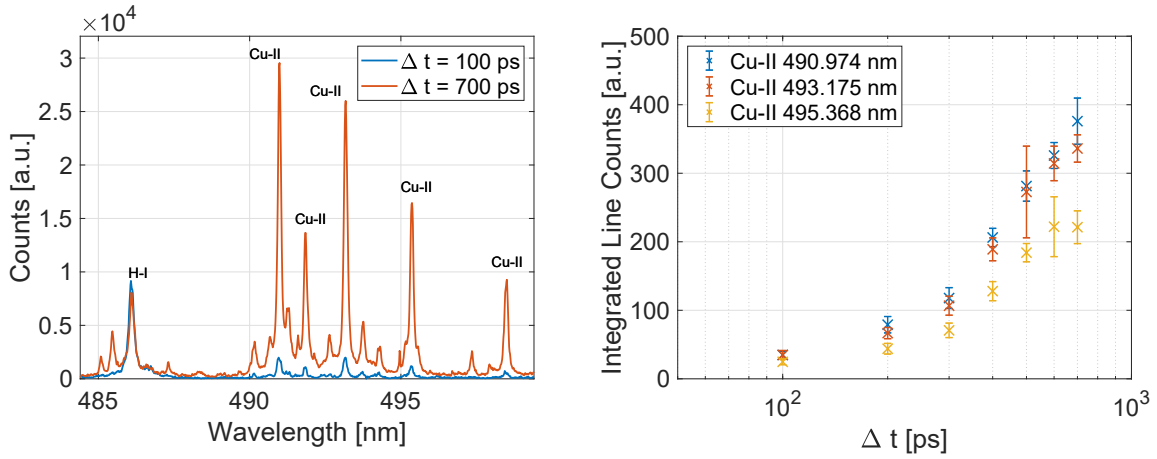

Figure 5.8: (left) Cu-II lines captured by the spectrometer with grating 2000 l/mm, gate width of 500 ns directly after the interaction with pre-pulse delay Δt. (right) Integrated counts of the observed lines with respect to Δt. The laser fluence of the main pulse is given as $F_2 = 537\,\mathrm{Jcm^{-2}}$ and the pre-pulse $F_1 = 6.6\,\mathrm{Jcm^{-2}}$.

delays. Note that in this configuration the pre-pulse intensity varies also. This observation shows a decreased laser intensity detection limit of almost one order of magnitude (from $\sim 10^{16}\,\mathrm{Wcm^{-2}}$ to $\sim 10^{15}\,\mathrm{Wcm^{-2}}$) when a pre-pulse is used. Moreover, these data contain the information that at high laser intensity the signal detected is not significantly influenced by the pre-pulse. Without the pre-pulse the observed signal grows almost linear with the intensity, while the signal with the pre-pulse of 700 ps seems to saturate in the focal spot. Here, typical uncertainties of the laser intensity are given in the horizontal errorbars and statistical variation of the line intensity detected on the vertical axis. Below, a laser fluence around the detection limit ($I = 6.7 \times 10^{16}\,\mathrm{Wcm^{-2}}$) is chosen and the pre-pulse delay Δt is varied. In fig. 5.8, the integrated line intensity of the observed Cu-II lines between a pre-pulse delay of 100 ps and 700 ps is given. In this range, an impressive enhancement factor of 28 can be observed. Take into account that the continuum radiation also rises in this observation. To reach a better signal-to-noise ratio, the gate delay needs to be adapted as the main pulse arm length is changed to setup the inter-pulse delay.

LIBS on Tantalum

With regard to applications concerning hydrogen storage and impurity in PCFs, LIBS experiments on high-Z material are executed. The material under investigation is tantalum (Ta, Z=73) in the form of a polished 9.9 mm × 9.9mm tile. First of all, the spectra shown in fig. 5.9 is discussed. Here, the influence of the same pre-pulse used in the previous section is shown in the focal spot of the laser $F_1 = 40\,\mathrm{Jcm^{-2}}$ (pre-pulse) $F_2 = 4000\,\mathrm{Jcm^{-2}}$ (main-pulse). Most of the spectral lines detected can be assigned to atomic tantalum. The remaining lines might be further impurities or more likely have their origin in the second order of the reflective grating. Here, it might be necessary to add spectral bandpass filter. It is worth mentioning that a reflective grating with 2000 l/mm, a camera gate delay of 30 ns and width of 100 ns is

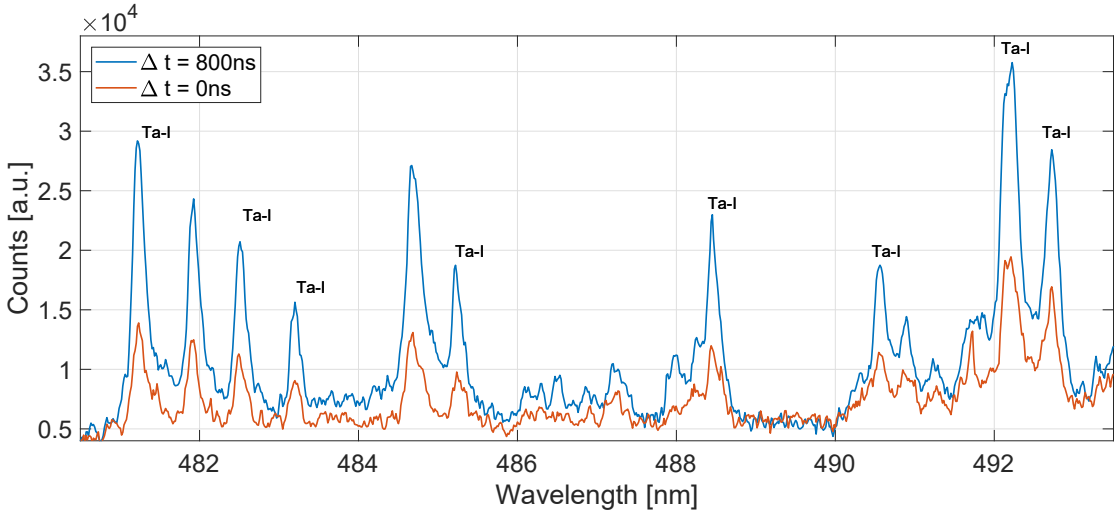

Figure 5.9: Laser-induced tantalum spectrum at the focal point ($F = 4000\,\mathrm{Jcm^{-2}}$) with two different pre-pulse delay Δt settings.

used. The pre-pulse of $\Delta t = 800\,\mathrm{ps}$ used is able to enhance the LIBS signals by at least a factor of two in this case.

To get a deeper understanding of the temporal emission dynamic of the expanding plasma on those high-Z materials, an investigation of the time resolved emission from the tantalum sample is shown in more detail in fig. 5.10 with the same laser conditions. Here, the spectrum around 656 nm is detected for two different pre-pulse configurations in the first 60 ns using the 1800 l/mm grating. It is possible to detect this early stage temporal emission dynamic with a gate width of 10 ns. In this spectral range, next to the Ta-I lines at 651.44 nm, 656.51 nm, 661.20 nm, and 662.13 nm, also the Balmer-α emission of hydrogen at 656.28 nm is detectable. For more details, the different spectral lines can be compared to table B.2. In the figure, the time resolved emission with a pre-pulse delayed by 700 ps (right) and without any delay (left) are compared. The gate delay used is denoted by different colors and offsets of 4000 counts are added between the measurements for a better overview. It turns out that the optical emission of hydrogen and the way heavier tantalum atoms are separated in time. This information is important,for the detection of fuel impurities in PFCs. All spectra presented are average signals of ten single laser pulses on unperturbed target positions. These measurements give evidence suggesting that the persistence of the hydrogen line is shorter without a pre-pulse, which leads to an enhancement of the observed line.

Up to this point, it has been shown that it is possible to enhance the spectral line intensity of atomic and ionic lines using a colinear pre-pulse configuration at the focal point. For comparison with the detected plasma expansion from section 5.1 the fluence is reduced to $F = 7.5\,\mathrm{Jcm^{-2}}$ by changing the relative z-position 400 µm in front of the focal point. Spectral analysis of the plasma shows that the atomic tantalum lines are detectable in the first $\sim 150\,\mathrm{ns}$ after the laser surface interaction. This investigation reveals that the time-frame claimed for optimal LIBS conditions in the previous section is confirmed and further substantiated. For later times the continuum background radiation rises again, which might be an

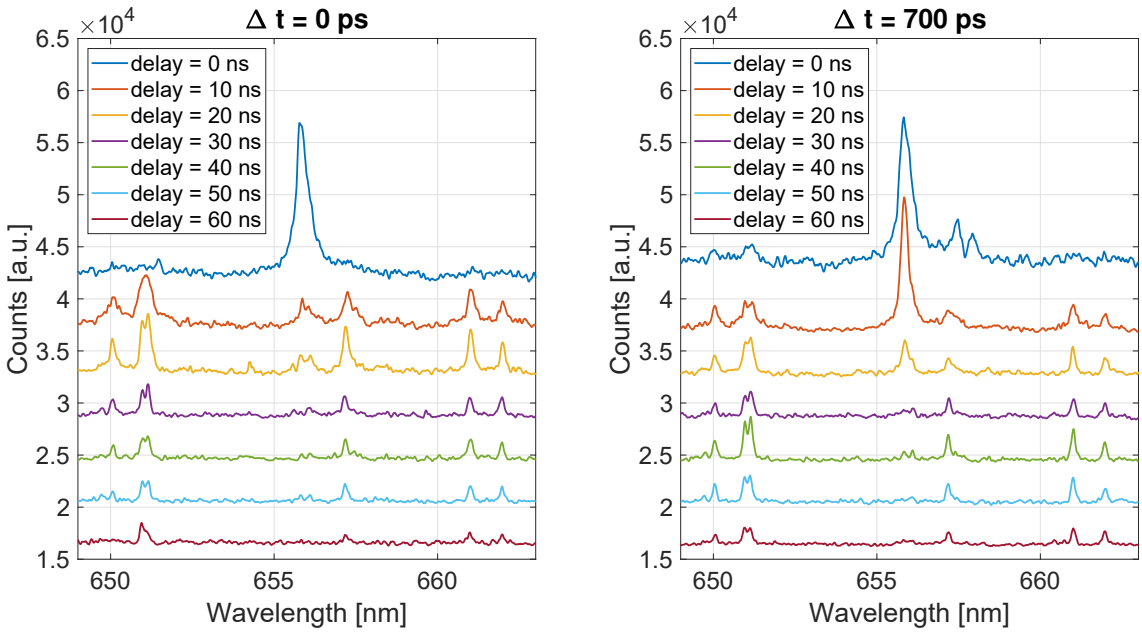

Figure 5.10: Persistence of atomic tantalum lines at 651.44 nm, 656.51 nm, 661.20 nm, and 662.13 nm, and hydrogen H_α at 656.28 nm emission under the influence of a pre-pulse of delay Δt. Added offset of 4000 counts between the spectra for a better overview.

indication for ablated clusters as discussed in the previous study in section 5.1.3. Figure 5.11 shows the influence of a $\Delta t = 800$ ps pre-pulse on the spectrum detected. The plotted spectra detected with a gate delay of 40 ns and gate width of 100 ns respectively are subtracted by the continuum radiation to better be able to compare the line intensities. Furthermore, the summed intensity of the two atomic tantalum lines investigated, indicated in red, is plotted with respect to the gate delay used. The spectrum initiated by the pre-pulse exhibits stronger emission lines in the early plasma stage, while the persistence is the same for both experimental setups.

5.2.3 Discussion

According to Noël et al. (2009, ref. [88]), who observed a similar situation as described here in a double-pulse experiment on copper, various processes will lead to the enhancement depending on the inter-pulse delay and the pre-pulse intensity. Early stage enhancement (meaning $\Delta t < 50$ ps), which is almost not observable in the results shown, can be related to different laser surface coupling characteristics. These results are compared to the output of a Two-Temperature Model (TTM) with the laser parameters of the weakest pre-pulse case ($I = 7.5 \times 10^{13}\,\mathrm{Wcm^{-2}}$), executed as described in appendix A. In this simulation, the lattice temperature exceeds the melting point in the first few picoseconds. The main pulse would interact with a liquid phase, which provides a lower electron heat conductivity κ_{el} than the solid phase. The authors of the article mentioned and others, like Mildner et al. (2014, ref. [55]), claim that this concentrates the laser energy absorbed on a smaller volume, as the reduced conductivity stops the heat transfer into the bulk. Higher energy

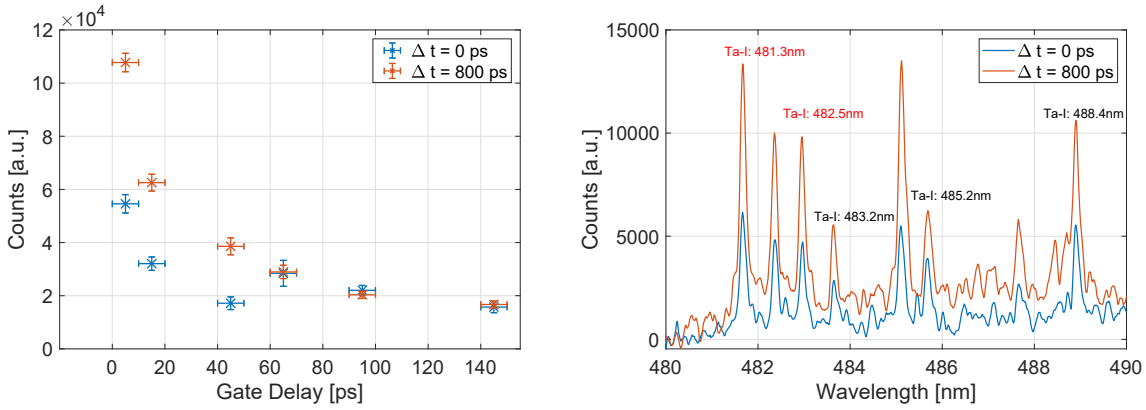

Figure 5.11: (left) Summed line Intensity of Ta-I lines (481.3 nm and 482.5 nm) with respect to the gate delay. (right) Laser-induced tantalum spectrum at $z = 400\,\mu\text{m}$ ($I = 10^{15}\,\text{Wcm}^{-2}$), gate delay of 40 ns and width of 100 ns, with two different pre-pulse delays Δt subtracted by the baseline continuum spectrum.

per unit volume would lead to an increased atomization degree, meaning a reduction of cluster creation. Ablated clusters, which are typically produced in femtosecond laser ablation, would contribute with continuum black-body radiation to the captured optical emission. A higher number of atoms can increase the brightness of the characteristic lines. Moreover, the reflectivity of the molten phase can be lower in metals, which would increase the laser energy absorption in the inter-pulse delay range from 1 ps to 50 ps. Assuming the two-temperature model is still valid in the liquid phase, the "lattice" temperature reaches energies up to 0.4 eV. Assuming this energy to accelerate single copper atoms and ions ($m_{\text{Cu}} \approx 1.06 \times 10^{-25}\,\text{kg}$) perpendicular to the surface, velocities of a around $1000\,\text{ms}^{-1}$ are reached. 50 ps after the pre-pulse interaction the plasma would have reached a distance of almost $0.1\lambda_0 \approx 80\,\text{nm}$ from the surface. In a plasma of this scale length, the absorption process of a laser pulse can be affected by collisional absorption in the form of inverse Bremsstrahlung or collisionless heating processes like Brunel- or "vacuum" heating, also referred to as resonance absorption, see chapter 2.2.1. Either one or the other process will dominate the laser energy absorption here. In conclusion the laser material coupling is much more efficient than the coupling to the solid or liquid phase and the particles in the plasma can be excited to higher ionization rate. Moreover, created clusters could be destructed, which again can enhance the atom number. At least one effect that might enhance the surface coupling can be precluded: Using the pre- and main pulse in isolation from each other (more than one second apart) to change the surface structure before the main pulse induced plasma is analyzed. A similar enhancement of the Cu-I lines as with $\Delta t = 700\,\text{ps}$ is not observed under these circumstances. Lastly, it has to be discussed whether a pre-pulse or double-pulse system would degrade the depth resolution of a material composition analysis. Regarding this question, an analysis of the ablation features on copper is a logical next step to extend this study. One investigation that might give a hint on this method was done by Semerok et al. (2004, ref. [89]). Here, the authors show that plasma shielding effects can even lead to a decrease of ablation depth in a

double-pulse configuration. Final predictions on this have to be postponed to further studies on the pre-pulse influence on the ablation characteristics.
In conclusion, the findings of this study reveal that an enhancement of atomic and ionic lines is possible with the use of a pre-pulse, in particular for the hydrogen Balmer-α line on the high-Z material used in this context. The experiments presented form the foundation for further studies on samples with deuterium retention. Here, it might be interesting to find the ideal pre- to main-pulse ratios for the strongest LIBS signal. Those findings can open a path to hydrogen isotope abundance analysis using femtosecond LIBS in vacuum environment.

5.3 Conclusion and Outlook

The experiments with the PHASER shown are more or less the essence of all plasma emission studies executed on the system influenced by different approaches to optimize the detection system. It has been shown that even with ultra-short laser pulses in the sub-10-fs regime it is possible to detect the plasma emission after the breakdown with reasonable magnitude, although it turned out that the persistence of the characteristic atomic and ionic lines is a lot shorter than when longer laser pulses are used. In particular, the plasma created on the heavier metals observed, like tantalum (Z=73) and tungsten (Z=74), reveal a high amount of clusters produced that are perturbing the brilliance of the lines observed and impede the application of LIBS as a diagnostic tool. In this case a pre-pulse can be useful minimize those distractions and leads to significant signal enhancement. Further studies on characteristics of expanding plasma with variations of the energy ratio of the two pulses in the pre-pulse module can be useful to optimize the LIBS system. In this context, it might be more reasonable to refer to it as double-pulse module. It is of high academic interest to find the origin of the enhancement process using a second laser pulse. For this, a few experiments on cluster production and early stage plasma expansion are useful. It has to be figured out how the crater morphology changes with the use of a second pulse. Moreover, it might be interesting to collect ablated nanoparticles deposited on a substrate placed perpendicular to the plasma expansion similar to ref. [90]. Such a study might figure out if number and size of those nanoparticles are changing with the pre-pulse influence. Another approach would be to get a deeper knowledge of the plasma coupling. Here, the interferometric pump-probe measurement presented in the of Michael Stumpf's master thesis (ref. [91]) can be used to figure out the plasma gradient induced by the pre-pulse. This information can give further hints to the absorption mechanism involved.
Another aspect that should be investigated further is the possibility to detect the hydrogen isotopes that can be stored in PFCs of confinement-fusion vacuum vessel walls. In general the PHASER system is ready to investigate this more deeply, if the Balmer emission is enhanced by a pre-pulse. The theoretical resolution of the spectrometer used is sufficient to be able to detect them when a plasma of low temperature and density is observed and line broadening effects have minor influence. A sample with the possibility of storing a high amount of deuterium like for example the Zircaloy-4 tiles used in ref. [92] can be a good alternative for a

proof-of-principle experiment. The group used an ultra-short laser ($\sim 5\,\mathrm{mJ}, 800\,\mathrm{nm}, 35\,\mathrm{fs}$) in an argon and helium environment to investigate the deuterium content in those samples and were able to detect stored deuterium with a concentration of 38 at%. Comparable samples used in this thesis do not surpass an amount of 1 at% of stored deuterium. It can be claimed that, with the LIBS setup presented on the PHASER system, it is possible to detect higher amount of deuterium even without the argon or helium environment, which is usually used to enhance the spectral line intensity. In the ensuing chapter, two successful experiments using different laser systems and environments for the detection of deuterium impurity in tantalum and tungsten tiles are presented in the next chapter.

Chapter 6

Analysis of Hydrogen Isotopes in W and Ta using LIBS

The main outcome of the studies presented on pulsed laser-based diagnostics is the comparison of LIBS experiments with a variety of laser systems. Due to this, the following chapter is devoted to different approaches towards a LIBS diagnostic for deuterium impurities in plasma-facing materials from fusion experiments. Pay attention to a brief disclaimer to this chapter concerning the use of the term "comparison". As the laser parameters and environmental conditions described for the produced plasma are deviating strongly from each other, a quantitative comparison is not possible at this point. With the experiments presented an overview of state-of-the-art LIBS techniques using lasers in a wide range of pulse duration and wavelengths is given with a focus on the different physical behavior of the plasma produced. As the most important outcome of the entire thesis, the use of one or a combination of some of the techniques presented as the best choice for an *in-situ* approach on upcoming fusion devices is discussed. To reach this point, the next sections are split to two different experiments including the use of an IR nanosecond laser and a near UV femtosecond laser. Approaches with the ultra-short near IR laser PHASER have been presented in the previous chapter. All laser models used are described in chapter 3.1.

6.1 IR ns-LIBS on Tantalum exposed to Deuterium

Below, the experimental results from the joint project executed at the Key Laboratory of Material Modification by Laser, Ion and Electron Beams at Dalian University of Technology in China are presented. The analyzed tantalum tiles were prepared and exposed to a deuterium plasma as described in chapter 3.5. The LIBS setup operates with a pulsed nanosecond laser on the sample that is attached to a vacuum chamber. For more details on the laser used and the spectrometer setup, please refer to chapter 3.1.3, 3.3.2 and appendix B. Initially the experimental setup will be described in detail, followed by the evaluation of the spectra generated. Here, the focus is on the proof-of-principle that a deuterium content can be detected under the circumstances described, without any quantification. Furthermore, this

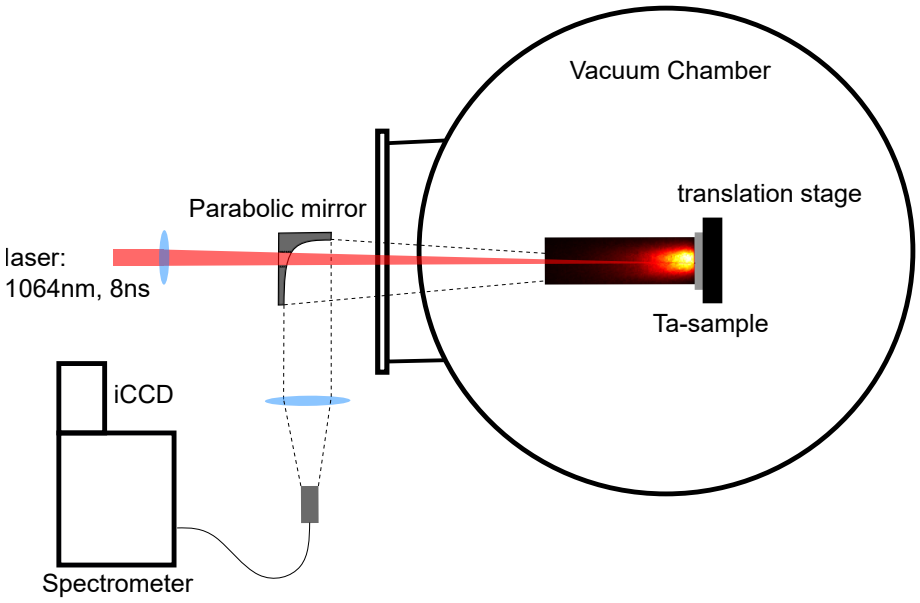

Figure 6.1: Experimental setup of a ns-LIBS experiment in a vacuum chamber. The laser assigned in red is focused by a lens through a hole in the parabolic mirror into the vacuum chamber to the sample surface. The mirror is collecting the emitted light from the plasma and a second lens images it on the entrance of a spectrometer with high spectral resolution.

experiment serves as a surrogate setup to find and evaluate a couple of difficulties facing the detection of isotopic shifts with other systems in the subsequent sections as well.

6.1.1 Experimental Setup

To begin, the experimental setup is shown schematically in fig. 6.1. The pulsed ($\tau = 8\,\mathrm{ns}$) infrared ($\lambda = 1064\,\mathrm{nm}$) laser pulses are focused by a $f = 250\,\mathrm{mm}$ lens through a hole in a parabolic mirror into the vacuum chamber to the sample holder placed on a one dimensional translation stage that is movable perpendicular to the incoming laser pulse. The $f = 152\,\mathrm{mm}$ parabolic mirror is used to collect the laser-induced plasma emission and guides it to a $f = 60\,\mathrm{mm}$ lens and a fiber coupled to a high resolution Czerny-Turner spectrometer (*Shamrock750*). The ambient pressure in the chamber is given by $\sim 10^{-7}\,\mathrm{mbar}$. The plasma emission is detected by an iCCD camera using a gate delay of 100 ns and 10 µs exposition. Ten consecutive laser pulses are applied to each position along the tantalum surface and the signals of eight positions are averaged. In the next section the detected spectra from two different tantalum samples are shown. The two samples are both polished and heated before they are applied to the diagnostic without the distinction that one is exposed to a deuterium plasma in the PSI-2 facility as described before. For comparison and as a practical example the Boltzmann method is used to estimate the plasma temperature for the status detected.

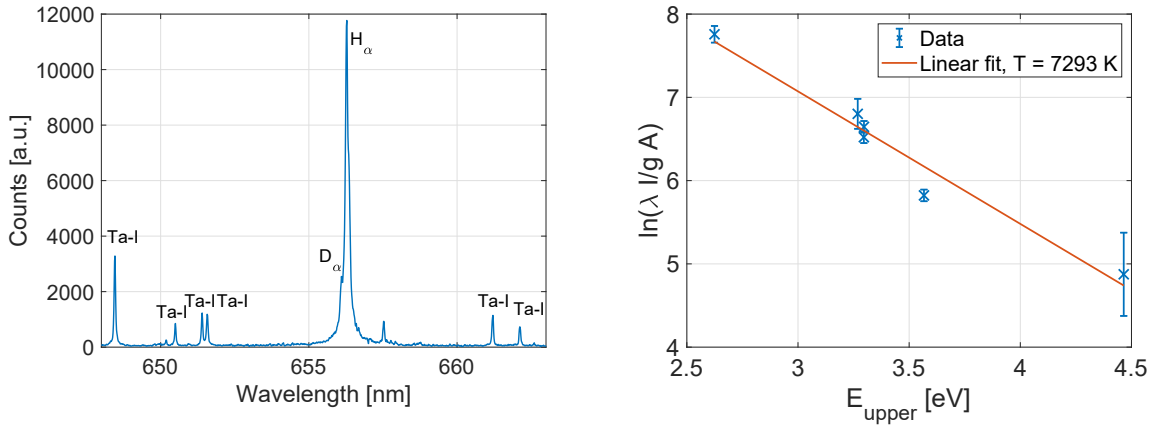

Figure 6.2: (left) Laser-induced tantalum spectrum with IR ns-laser of pulse energy 30 mJ at the sample close to the focal position ($D_0 \approx 1$ mm) detected by *Shamrock750* with a 1200 l/mm grating and 50 µm slit width. (right) Boltzmann plot with detected atomic tantalum lines.

6.1.2 Results and Discussion

The spectrum detected with the LIBS setup described is shown on the left in fig. 6.2. The spectrum presented is an average of seven signals from laser interaction with the fresh surface. This explains the high hydrogen Balmer-α ($\lambda = 656.28$ nm) signal, as moisture consisting of water and organic compositions might be deposited on the surface. Moreover, the atomic tantalum lines observed are indicated here. Using the corresponding spectroscopic parameters for those lines given in table B.2, the plasma temperature can be estimated using the Boltzmann plot method from equation (3.26). The corresponding logarithmic relation for the line intensity I is plotted with respect to the upper energy level of the transition and a linear fit provides the temperature of 7293 K. For detailed information on this methodology refer to chapter 3.4.2. The errorbars shown correspond to the accuracy of the optical strength value A_{ki}. Note that this method depends strongly on a correct calibration of the detector, selected emission lines and a few assumptions to the plasma conditions like the presence of an LTE, temporal and spatial homogeneity and the optical thickness of the lines detected. With this disclaimer, the estimated plasma temperature can be seen as a rough benchmark of possible values expected from the laser system used.

With a closer look on the spectral range around the Balmer-α transition line of hydrogen, the spectrum detected reveals an interesting feature at 656.1 nm, which might be an indication for the emission of deuterium atoms. In fig. 6.3, a zoom into the spectrum presented is plotted together with the same spectrum from a pure tantalum sample that was not exposed to the deuterium plasma. Both spectra are normalized to make the difference visible. This was necessary, because the measurement from the exposed sample indicates a slightly lower spectral intensity. The estimated temperature of 7241 K is similar to the exposed tile, which is necessary to be able to make the comparison here. The two spectral lines of the hydrogen isotopes separated by ~ 180 pm are clearly distinguishable with the setup used. Note that

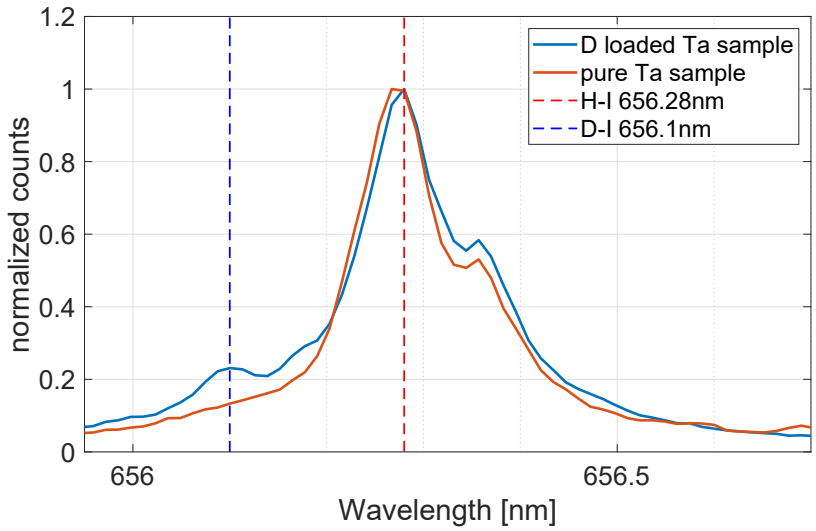

Figure 6.3: Comparison of normalized atomic hydrogen (H-I) signal from tantalum tiles with and without the deuterium exposition.

the de-convolution of the two lines by a fitting function is not trivial, as the spectral range of interest overlaps with two atomic tantalum lines at 656.16 nm and 656.43 nm. It has to be mentioned, but not explicitly shown here, that consecutive laser irradiation on the same position does not bring a detectable deuterium or hydrogen signal, which might indicate that the deuterium only penetrates into the first few layers of the target. Typical ablation rates of the nanosecond laser used with the fluence of around 7.6 Jcm^{-2} are in the range of 100 nm per pulse and the heat affected volume is even larger.
All in all, it has been shown with this experiment that it is possible to detect hydrogen isotopes loaded to the high-Z metal tantalum using ns-LIBS in a vacuum environment. Most likely, the low ambient pressure is conducive in this context, because collisional line broadening effects are limited. In further studies on tantalum, it might be necessary to detect the hydrogen Balmer-β transition at 486.135 nm, as it does not interfere with atomic tantalum lines, although the expected line intensity of this line is significantly lower. After this proof-of-principle experiment on tantalum an approach to determine the deuterium amount stored in exposed tungsten tiles is presented in the next section.

6.2 Near UV fs-LIBS on Metal Tiles Exposed to Deuterium

The described experiment in this section follows the content of the article “Hydrogen Isotope Analysis in W-Tiles using fs-LIBS” (2023, ref. [93]) published in Scientific Reports, with a few additions. The experiments were conceived and conducted at Lawrence Berkeley National Laboratory. Here, a near UV femtosecond laser is used in an approach to analyze the isotopic abundance or concentration of deuterium in tiles of relevant plasma-facing materials that were exposed to a deuterium plasma. It is expected that the chosen wavelength and pulse duration can be used to analyze the deuterium content with a high depth resolution. Note

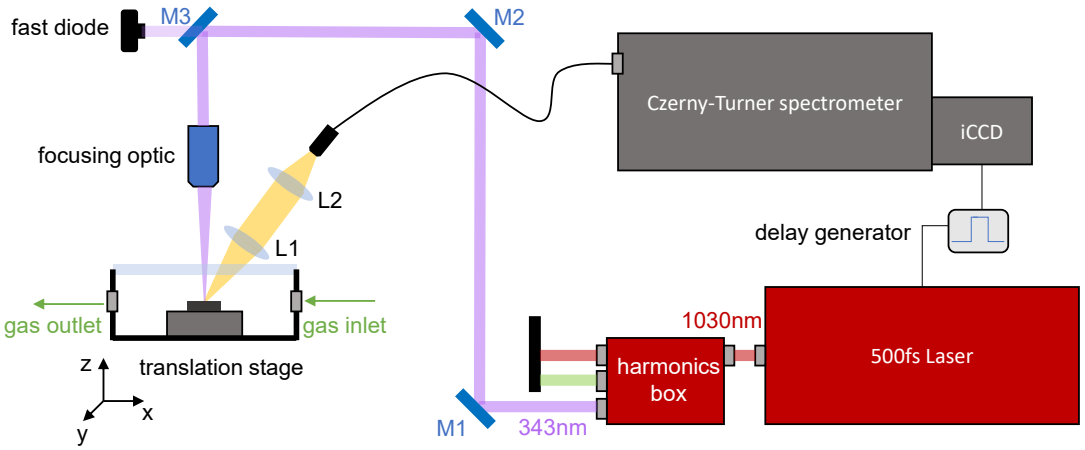

Figure 6.4: Experimental Setup of femtosecond UV LIBS experiment with gas compositions at atmospheric pressure. The third harmonic of the fundamental laser wavelength (assigned in purple) is guided by a set of mirrors (blue blocks) and focused to the experimental cell. A spectrometer triggered by the laser signal detects the plasma emission collected by the two applied lenses of focal length $f_1 = 50\,\text{mm}$ and $f_2 = 100\,\text{mm}$. Figure is taken from ref. [93] and licensed under CC BY 4.0.

that it is necessary to reduce the laser pulse fluence to reach the point of low ablation rate. Here, the observed plasma parameters for different laser fluences are determined and the feasibility of this method is discussed. In particular, a study on quantitative detection of deuterium impurities in tungsten is presented. In addition, the high depth resolution of material composition measurement is demonstrated on a tantalum sample, and the results are compared to an experiment on organic material with varying deuterium content as an approach towards a method to predict the total deuterium amount in the created laser plasma. In the next paragraphs the experimental setup and used materials are introduced followed by an evaluation of the results.

6.2.1 Experimental Setup

The basic setup of the LIBS experiment is shown in fig. 6.4. The laser consists of the $\lambda = 1030\,\text{nm}$, $500\,\text{fs}$ *Amplitude s-Pulse* laser in the $1\,\text{kHz}$ mode and a setup for second and third harmonic generation described in chapter 3.1. In this set of experiments, the third harmonic of the fundamental laser frequency was used at 343 nm. Figure 6.4 gives a schematic overview of the experimental setup. The pulses generated with an output pulse energy of up to $100\,\mu\text{J}$ are focused by a 3x objective lens (50 mm working distance) to the target placed in an experimental cell ($10\,\text{cm} \times 10\,\text{cm} \times 5\,\text{cm}$) that can be filled with different gas compositions from an external inlet. By choosing a smaller outlet than inlet diameter and a gas flow of two liter per minute, a sufficient concentration of the used Ar gas at atmospheric pressure is applied to the cell. The whole cell is placed on motorized stages to control the distance between the focusing lens and the target and to irradiate different positions on the surface. A collection

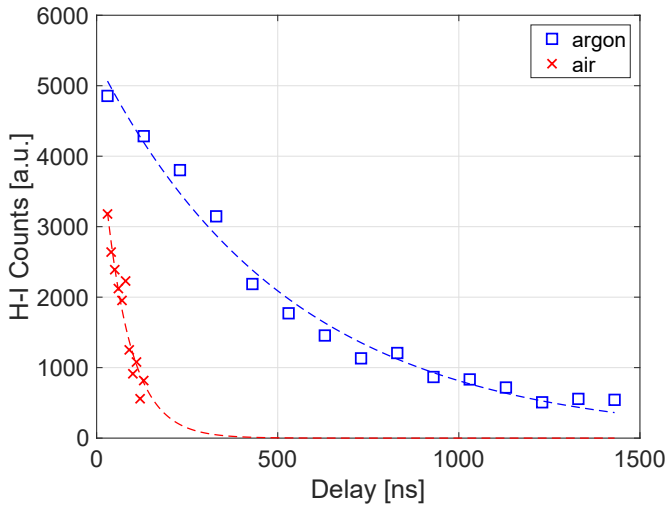

Figure 6.5: Detected integrated counts (gate width 100 ns) of hydrogen Balmer-α spectral line on untreated tungsten (W) tile using the same setup with ambient argon (blue squares) and air (red crosses) at atmospheric pressure. Exponential fits are indicated with dashed lines. The content is published in ref. [93].

system consisting of two plano-convex fused silica lenses ($f_1 = 50\,\text{mm}$ and $f_2 = 100\,\text{mm}$) and an optical fiber that is coupled to the setup to collect the plasma radiation and imaged to the entrance slit of one of the two Czerny-Turner spectrometers *IsoPlane-320* (lower resolution for broader spectral range) or *Horiba Jobin-Yvon1250M* (high resolution setup to resolve isotopic shifts). The plasma emission signal is enhanced and detected by an iCCD camera that is triggered by the laser shutter. This trigger signal is controlled by a digital delay generator.

Preparation of W- and Ta- Tiles

The material under investigation is pure polished tungsten (W, Z=74) and tantalum (Ta, Z=73) with a surface roughness of $S_a = 60\,\text{nm}$. in form of squared tiles (9.9 mm × 9.9 mm × 5.1 mm), which are outgassed under 1000 °C for three hours and exposed to deuterium in the linear plasma device PSI-2 at Forschungszentrum Jülich. The tiles are arranged in a circle on a molybdenum mask while the ring shaped plasma interacts with it. Plasma parameters are detected by a Langmuir probe frequently during the four hour process. The maximum deuterium flux is measured as $2.9 \times 10^{21}\,\text{m}^{-2}\text{s}^{-1}$ with a total fluence of $3 \times 10^{25}\,\text{m}^{-2}$ onto the tile surface heated to a temperature of 230 °C. The plasma parameters in the PSI-2 to mimic the fusion plasma are described by Kreter et al. (2019, ref. [65]). From this overview, a deuterium concentration of up to 2 at% in the first 1 µm behind the surface is reasonable with the used settings. According to a Thermal Desorption Spectroscopy (TDS) measurement applied *ex-situ* after the exposure, the total number of detected deuterium atoms deposited per area in the bulk are given as $N_D = (3.9 \pm 0.8) \times 10^{20}\,\text{m}^{-2}$, and $N_H = (4.1 \pm 1.1) \times 10^{21}\,\text{m}^{-2}$ hydrogen atoms.

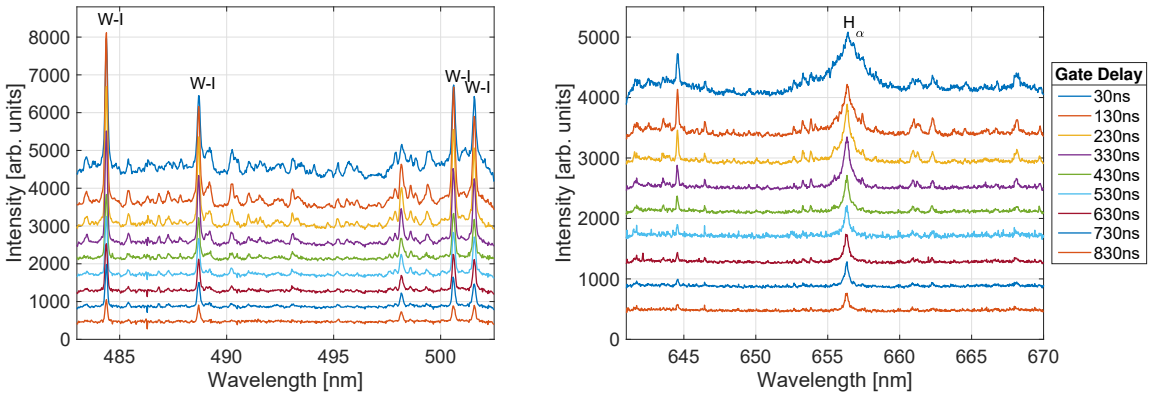

Figure 6.6: Time resolved emission from the tungsten sample under fs laser irradiation in Argon. For these experiments the *IsoPlane320* spectrometer with a 1800 lines/mm at two different central wavelengths is used. The gate width was set to 100 ns. For visibility 400 counts are added across two distinct spectral ranges for each given gate delay. Figure is taken from ref. [93] and licensed under CC BY 4.0.

6.2.2 Results and Discussion

In the following experiments, an argon gas flow, according to similar findings as in ref. [94], is used to enhance the plasma emission observed. The heavier Ar atoms in the ambient gas (compared to nitrogen atoms in pure air) around the expanding plasma lead to more elastic collisions resulting in a longer plasma persistence of the plasma expanding. This and a higher plasma temperature as described by ref. [95] lead to stronger line emission. Figure 6.5 presents the temporal evolution of the hydrogen Balmer-α emission from the tungsten tile surface using air and an argon flow in the ambient atmosphere. An increase in half-life of more than a factor two can be observed. This results in a significant signal enhancement and the possibility to apply a LTE to the expanding plasma, because the plasma has enough time to thermalize. The electron number density n_e and temperature T_e in the plasma are determined by observing the H_α (Balmer-α) peak. The FWHA line broadening contains the information on n_e using equation (3.19) and the Doppler width (3.21) is used to determine T_e.

Before the experimental requirements to observe the deuterium impact on the tungsten tiles exposed are discussed, the temporal optical emission of the plasma in this experiment is presented using a laser fluence of $31\,\mathrm{J/cm^2}$. This value is way above the ablation threshold determined as $F_{th} = (0.07 \pm 0.06)\,\mathrm{J/cm^2}$, discussed in the next section consulting ref. [22], [73], [76], [85]. Figure 6.6 shows the temporal evolution of the observed spectra in this configuration with the *IsoPlane320* spectrometer (instrumental broadening $w_{inst} = 52\,\mathrm{pm}$ at a slit width of 100 µm). The used spectral lines for the Boltzmann plot method are given in table B.2. Moreover, a couple of more atomic tungsten lines can be observed as assigned in the plots with varying accuracy together with the hydrogen Balmer-α transition (H_α). The plasma temperature, evaluated using the Boltzmann plot method and the Doppler broadening are given in fig. 6.7 (left). The electron number density is evaluated by observing the FWHA of

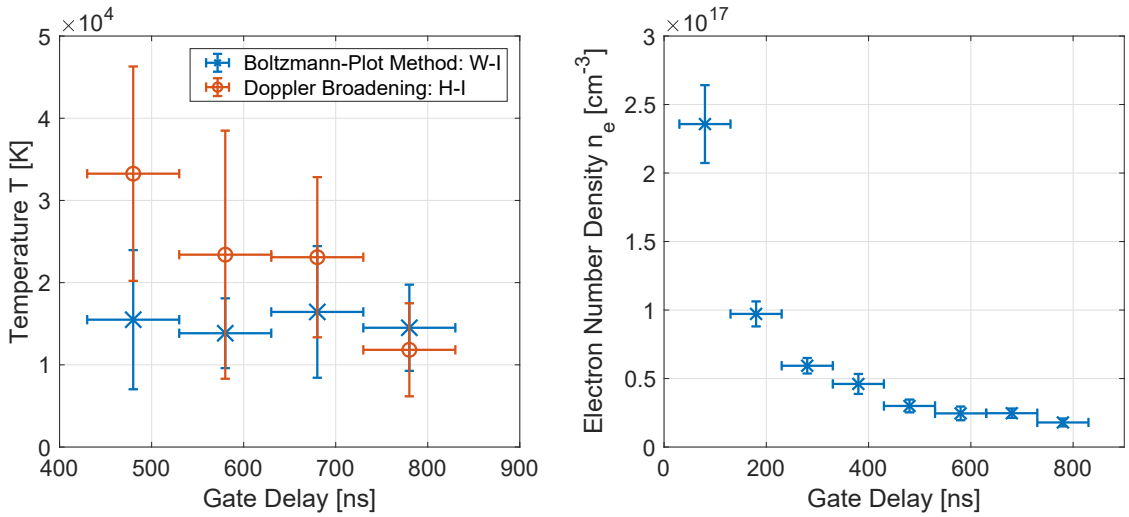

Figure 6.7: (left) Plasma temperature T_e evaluated from the observed tungsten (W) spectrum by using the Bolzmann-plot method including atomic W-I lines with blue crosses and the Doppler Broadening of the H_α line with orange circles. (right) Electron number density n_e evaluated by Stark broadening of the same line. Error-bars indicate statistical deviations from the measured values on the y-axis and the used gate width on the x-axis. Figure is taken from ref. [93] and licensed under CC BY 4.0.

the H_α line and is exponentially decreasing from $5 \times 10^{17}\,\mathrm{cm}^{-3}$ by one order of magnitude in the first 800 ns as shown in fig. 6.7 (right). Note that the observed hydrogen Balmer-α line interferes with a tungsten line at 656.32 nm and the weak signal from the deuterium impurity D_α at 656.1 nm. Most likely, the pseudo-Voigt fit is influenced by these disturbances and the calculated temperature and density values can be overestimated.

Summing up the result of the plasma observation from the given material, the plasma temperature and number density decreases as expected. The parameters are in the range of $T_e \approx 15,000\,\mathrm{K}$ to $T_e \approx 10,000\,\mathrm{K}$ and $n_e \approx 2.5 \times 10^{17}\,\mathrm{cm}^{-3}$ to $n_e \approx 10^{16}\,\mathrm{cm}^{-3}$. Note that the evaluated temperatures for delays lower then 400 ns are strongly deviating with the two presented methods. One reason for this is the high plasma density in the early expansion phase that brings a higher self-absorption leading to an overestimation of the spectral width of the hydrogen emission. Another explanation might be given by the deviating first ionization potential of tungsten (7.86 eV) and hydrogen (13.598 eV) that influences the atom to ion proportion in the hot part of the plasma. Hence, the plasma parameters observed after 400 ns are typical values for laser-induced plasmas in an argon environment (compare ref. [96]). One important takeaway from the presented measurement is the transient character of the plasma observed by the exponential decrease of the number density. This is also the critical point that has to be considered, when a LTE is applied to the observed plasma. The question, analogue to ref. [46], is whether the relaxation time τ_{rel} and corresponding diffusion length $\lambda = (D_h \cdot \tau_{rel})^{1/2}$ can be covered within the plasma expansion process. Here, D_h is the material dependent diffusion coefficient. Typical values for metals are on the order of $\tau_{rel} \sim 10^{-9}\,\mathrm{s}$ and $\lambda \sim 10^{-5}\,\mathrm{m}$. The lifetime (about a few micro seconds) and plasma size

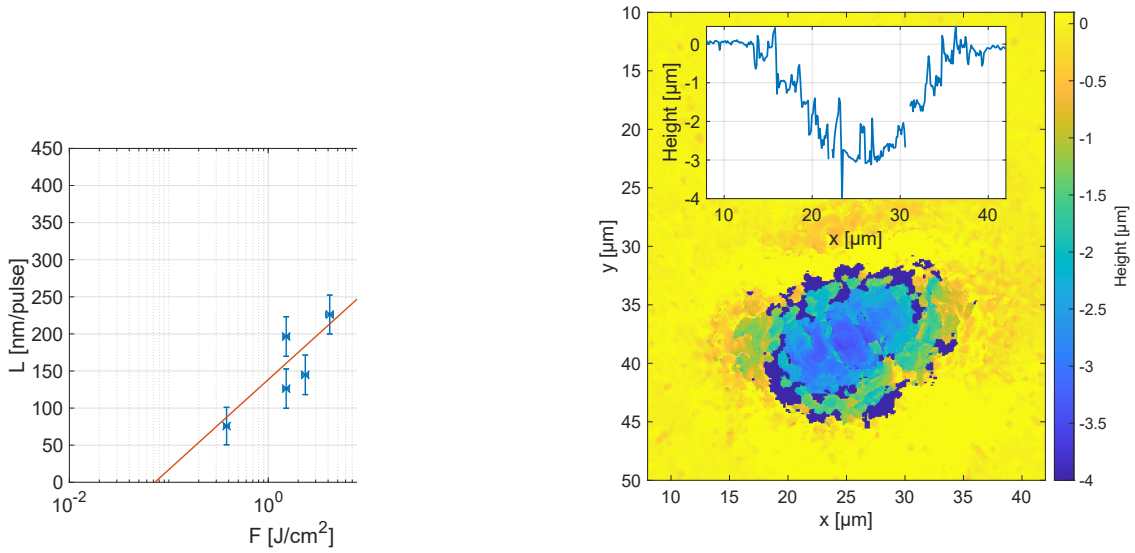

(a) (b)

Figure 6.8: (a) Ablation rate L with respect to laser fluence F on logarithmic scale. (b) Height map of crater induced by five consecutive laser irradiations on the same position on the W tile. Vertical lineout in the center of the crater is given in the inlet. Results are published in ref. [93].

(even larger than the beam diameter $\sim 20\,\mu m$) of the observed expansion suggests that a LTE is reasonable in the recombination part of the process. Moreover, the McWhirter criterion in equation (2.27) is a necessary condition to be fulfilled. As an example it is calculated for the tungsten plasma observed with a delay of 830 ns: $T_e \approx 10,000\,K, n_e \approx 4.7 \times 10^{16}\,cm^{-3}$ and $\Delta E_{mn} \approx 3\,eV$ fulfills the condition as $n_e > 4.3 \times 10^{15}\,cm^{-3}$.

Laser Ablation of W

In addition to the optical emission experiments on the expanding plasma, a classification of the used laser fluence is given. For this, an ablation experiment is presented to estimate the threshold fluence of the used laser on polished tungsten samples. Moreover, a definition of the used laser fluence is given.
Analogous to ref. [73] the used laser peak fluence of the almost top-hat beam profile can be described by the pulse energy E and beam diameter D_0 at $1/e^2$ of the maximum intensity as

$$F = \frac{4E}{\pi D_0^2}. \tag{6.1}$$

The diameter is estimated by observing the produced crater morphology. Moreover, following the theory of Chichkov et al. (1996, ref. [22]) the threshold fluence F_{th} can be estimated by applying the formula

$$L = \alpha^{-1} \ln\left(\frac{F}{F_{th}}\right) \tag{6.2}$$

as a fit to the ablation rate L (depth per pulse) depending on the varying laser fluence. Here, α^{-1} is a numerical fitting parameter that can be interpreted as the optical penetration depth. Similar to the analysis of Lickschat et al. (2020, ref. [85]) the threshold fluence of ultra-short laser pulses is calculated by the equation (5.1). The necessary material parameters for the bulk tungsten (W) are given as: Evaporation enthalpy $H_v = 774\,\mathrm{kJ/mol}$, density $\rho = 19.25\,\mathrm{g/cm^3}$, molar mass $M = 183.84\,\mathrm{g/mol}$ and wavelength dependent values of reflectivity $R(343\,\mathrm{nm}) = 0.34$ and optical penetration depth $\alpha(343\,\mathrm{nm}) = 9.26 \times 10^5\,\mathrm{cm^{-1}}$ [76]. The resulting theoretical threshold fluence is calculated as $F_{th} = 0.13\,\mathrm{J/cm^2}$.
The laser-induced craters by multiple laser irradiations on the same position are observed by the white light interferometer *Zygo NewView 6000 3D* that is also used to determine the surface roughness of the used tiles. The surface roughness is given as $S_a = \frac{1}{N}\sum_{k=1}^{N}|z_k - u|$ with mean height u over N positions. This results in $S_a = 60\,\mathrm{nm}$, which is similar for all used tiles. In fig. 6.8 (a) the fluence dependent ablation rate is given for the low laser fluence regime on a bulk tungsten sample. Here, craters are formed by ten consecutive laser pulses on the same position and ablation rate is estimated by crater depth divided by the number of pulses. The output power is reduced to $30\,\mu\mathrm{J}$ by a half wave plate and a beamsplitter. Moreover the fluence is controlled by variation of objective lens and surface distance that changes the beam diameter. The presented errorbars on the measurement (blue crosses) result from statistical uncertainties measuring nine craters for each fluence and systematical uncertainties by the knowledge of pulse energy by approximately $\pm 5\,\%$, beam diameter by $\pm 1\,\mu\mathrm{m}$ and crater depth by $\pm 50\,\mathrm{nm}$. Applying equation (6.2) as a fit function using F_{th} and α as fitting parameters, the resulting threshold fluence is given as $F_{th} = (0.07 \pm 0.06)\,\mathrm{J/cm^2}$. This value is more or less consistent with the overestimated calculated value of $0.13\,\mathrm{J/cm^2}$ from equation (5.1). Note that the surface roughness might have an impact on the used reflectivity value in this estimation.

CF-LIBS Approach

Below, the observation of the hydrogen Balmer-α transition from the tungsten tile with the *Horiba Jobin-Yvon1250M* spectrometer with a higher "resolving power" (instrumental broadening $w_{inst} = 12.7\,\mathrm{pm}$ at slit width of $120\,\mu\mathrm{m}$) is described. It turns out that the temperature and number density values presented in the LTE validation are typical parameters that are needed for the upcoming investigation. In Fig. 6.9 the detected LIBS signals of a tungsten tile exposed to the deuterium plasma in PSI-2 as in Jiang et al. (2021, ref. [97]) is compared to an unexposed tile. In blue, the accumulated data from 80 independent single pulse interactions on the unperturbed sample surfaces are plotted and in orange the sum of all measurements from irradiation number 2 to 5 on the same positions. First of all, a distinct deuterium line at 656.1 nm can be observed in the exposed tile (left), while in the unexposed tile (right) only the hydrogen line at 656.28 nm is detectable. The presence of the hydrogen line in both tiles is most likely attributed to adsorbed moisture on the surface and hydrogen remaining in the bulk. Moreover, it should be pointed out that after the first laser irradiation no Balmer-α

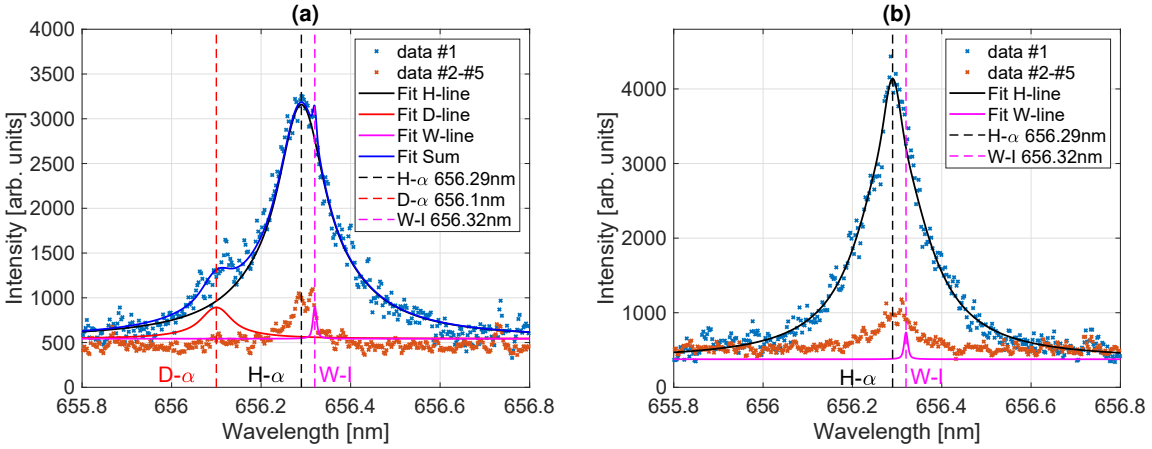

Figure 6.9: (left) High resolution detection of hydrogen isotope lines (H_α and D_α) in the exposed tungsten tile. (right) Comparable record on a pure tungsten tile. In black, red and blue pseudo-Voigt fits of the overlapping deuterium and hydrogen spectral line of Balmer-α transition are given. The blue crosses represent the measurement of the first laser irradiation (average of 80 positions) and orange the second to fifth irradiation at the same positions respectively. The applied gate delay and width are chosen as 1.08 µs. Figure is taken from ref. [93] and licensed under CC BY 4.0.

line can be detected. Only the atomic tungsten line at 656.32 nm can be observed. Applying a pseudo-Voigt fit brings the opportunity to compare the line broadening effects on the heavy and a regular hydrogen atoms. Here, the FWHM of $\Delta\lambda_H = 234\,\text{pm}$ and $\Delta\lambda_D = 170\,\text{pm}$ respectively is observed. This discrepancy can be explained by different reduced masses µ of the collision partners influencing the Stark effect and the dependency of the Doppler width on the atomic mass as $\sim \sqrt{m^{-1}}$. As it is explained in chapter 3.4.1, the combination of collision and temperature effects are responsible for the line broadening. From the hydrogen peak the corresponding plasma parameters that are necessary to distinguish the lines are extracted as $T_e < 20,000\,\text{K}$ and $n_e < 10^{17}\,\text{cm}^{-3}$.

Observing the corresponding crater for this LIBS measurements provide the information on the possible ablation rate that can be applied to this setup. Figure 6.8 (b) shows a typical crater produced by five single laser pulses in argon environment on the W-tile. With around 600 nm per pulse the ablation rate is comparable high to what is possible with the used laser, but with a lower ablation rate it is not possible to observe a noticeable signal from the hydrogen impurities. Integration over the whole crater brings the total ablated volume of $(282 \pm 25)\,\mu\text{m}^3$ for five consecutive laser irradiations.

The combination of all presented data on the temporal plasma emission dynamic and the possibility to separate the hydrogen isotopes in the first laser irradiation brigs the opportunity to estimate the deuterium impact to the yield ablated for a single irradiation. Here, a quantitative investigation on the deposition is possible and given for the tungsten tiles: The measured temperature can be used to find the deuterium and hydrogen concentration by plotting the measured intensity of the hydrogen Balmer-α line to the Boltzmann plane within the Boltzmann plot method from equation (3.26). Here, it is assumed that the tung-

sten and hydrogen subsystems exhibit the same temperature calculated by the Boltzmann plot method in the previews section. The used spectral characteristics of the H-I line are presented in table B.2. Note that the measured intensity needs to be adapted to the sensor sensitivity calibrated by a halogen lamp of defined emission characteristic. Now, estimations mentioned in the previews section can be applied for the CF-LIBS method. In addition, the composition of the observed plasma in a LTE (delays longer than 400 ns) is assumed to be purely tungsten, hydrogen, and deuterium atoms. Further minor impurities on the surface and in the bulk, and the argon atmosphere are ignored. From the intercept of the Boltzmann plot, the concentration of tungsten C_W and both Hydrogen-Isotopes H and D combined $C_{H\&D}$ can be estimated. The evaluated fraction is given as

$$\%(\mathrm{H}+\mathrm{D}) = \frac{C_{H\&D}}{C_{H\&D}+C_W} \cdot 100\%. \tag{6.3}$$

Note that the experimental factor F in the Boltzmann plot formula (3.26) is the same for both materials as it depends on the collection system and plasma size. From the high resolution measurement in fig. 6.9 and the pseudo-Voigt fits a ratio of the integrated concluded full areas can be calculated as $D_\alpha/H_\alpha \approx 0.08$. This relation is transferred to the total number ratio N_D/N_H and can then be used to estimate the total deuterium contamination. With a total ablated volume of $(57 \pm 5)\,\mu\mathrm{m}^3$ with each irradiation estimated from the findings in fig. 6.8 (b), the total number of ablated tungsten atoms is given as $(3.6 \pm 0.3) \times 10^{12}$. Taking into account the molar volume of tungsten as $M_{V,W} = 9.47 \times 10^{-6}\,\mathrm{m^3 mol^{-1}}$. Applying Equ. 6.3, the found concentration values and the total number ratio, the number of hydrogen and deuterium atoms are given as $N_H = (7.8 \pm 3.9) \times 10^{11}$ and $N_D = (6.2 \pm 2.8) \times 10^{10}$ respectively. Here, the uncertainty is just a statistical variation and has to be extended by the mentioned approximations and deviations of the ablated volume. This includes that the value is probably more an upper limit due to the overestimated Balmer$-\alpha$ intensity that is influenced by a W-I line. Concidering this, the value holds up to a comparison to the TDS data. The total number of deuterium atoms detected in the whole sample is estimated as $(3.8 \pm 0.8) \times 10^{16}$. Here, an accuracy of 21% is calculated for the TDS measurement. From this it follows that on the laser irradiated spot in the LIBS experiment up to $(1.2 \pm 0.2) \times 10^{11}$ atoms can be expected, which is a factor two larger than what is calculated by the CF-LIBS approach. This deviation might result from the uncertainty of the two methods, as it can be expected from studies on PSI-2 in ref. [65] that deuterium is only stored in depths of around 100 nm. Also note that the deuterium distribution along one dimension of the tiles surface is not homogeneous due to the plasma gradient given in the exposition process. This can result in an over or underestimation of the expected deuterium number depending on the position on the tile. The presented accumulated measurement is executed close to the center of the tile and along the axis where no significant changes in the deposition is expected. In conclusion, the presented CF-LIBS method can be used to determine the deuterium impact in the used W tiles as around $(1.7 \pm 0.5)\,\mathrm{at}\%$ in the first 600 nm behind the surface with a high lateral resolution of $\sim 20\,\mu\mathrm{m}$, according to the crater diameter. This result is consistent

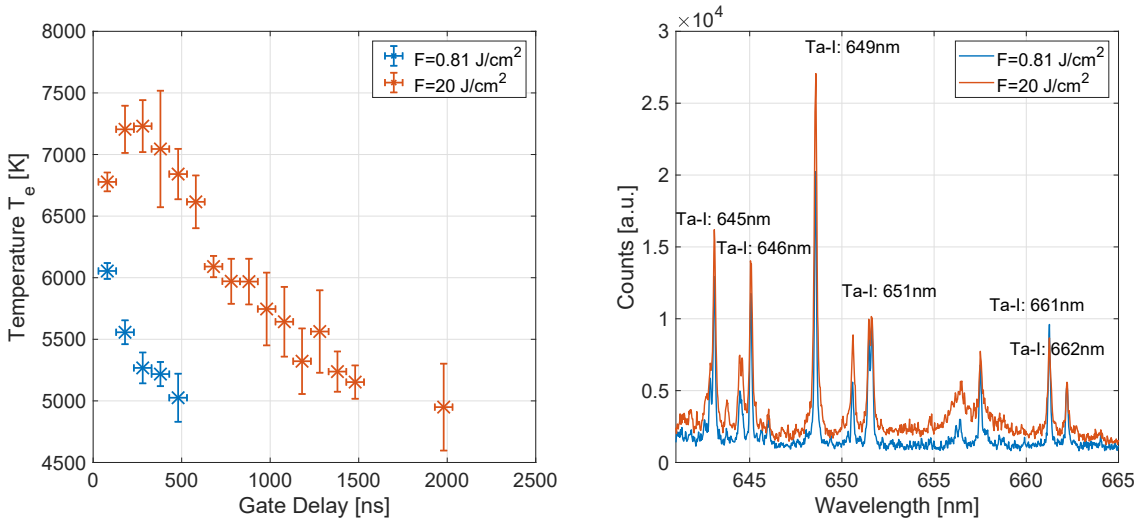

Figure 6.10: fs-LIBS on tantalum with 500 fs UV laser pulses of fluence 0.81 $\mathrm{Jcm^{-2}}$ and 20 $\mathrm{Jcm^{-2}}$. (left) Plasma temperature estimated by Boltzmann plot method. (right) Optical emission spectroscopy with *Isoplane320* spectrometer with a 1800 l/mm grating at gate delay 80 ns and width 100 ns.

with other findings [98] indicating a deuterium concentration rapidly decreasing to 0.2 at% in a depth larger than 1 µm behind the surface in similar prepared tungsten tiles.

High Depth Resolution on Tantalum

It has been shown that the deuterium content can be detected with a depth resolution of 600 nm in tungsten. With the fluence of 31 $\mathrm{Jcm^{-2}}$ the deuterium and hydrogen contribute to the plasma spectrum detected. In the next step the laser fluence was reduced by increasing the laser spot size on the sample surface. Here, the objective lens is substituted by a lens of $f = 100$ mm, which increases the focal spot size to a diameter of 25 µm resulting in a laser fluence of 20 $\mathrm{Jcm^{-2}}$. In addition, the distance of the surface and the focussing object is changed that it is placed 4 mm behind the focal spot. The ablated feature exhibits a diameter of 125 µm and a maximum depth of 30 nm for a single laser shot in tantalum. The laser fluence with this setting is determined as $F = 0.81\,\mathrm{Jcm^{-2}}$. With this configuration the plasma emission from a tantalum tile was detected. In fig. 6.10 the emission spectrum generated by the two different laser fluences, and the plasma temperatures determined are plotted. The spectral lines used for the Boltzmann plot method are denoted in the figure and optical parameters are taken from table B.2. This investigation reveals two main takeaways: First, the hydrogen and deuterium atoms in the plasma do not contribute to the spectrum detected. Second, a lower laser fluence leads to a shorter plasma persistence and lower overall plasma temperature. The data point out that material composition analysis might be possible with a high depth resolution of 30 nm or lower, but the analysis of hydrogen and its isotopes is not straight forward, either because the ablated amount might be below the detectable limit, or the hydrogen atoms are not excited efficiently according to the plasma temperature

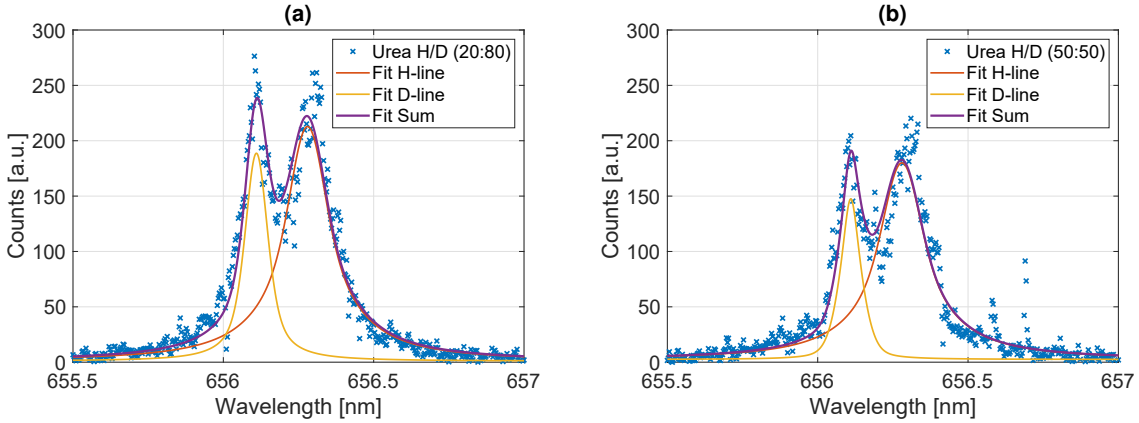

Figure 6.11: LIBS signal from mixed urea samples using laser pulses of 500 fs pulse duration, wavelength 343 nm and a fluence of 31 Jcm^{-2}.

detected. In this context another study is necessary with a way higher deuterium content in the tiles under investigation to estimate a detection limit with the presented method. Moreover, a double-pulse approach to increase this detection limit can be tested.

Detection of Hydrogen Isotopes in Organic Material

Another approach that has been made, is the comparison of the presented data to a test sample with a known hydrogen isotope ratio. On the one hand, this experiment presents the high resolution of the spectrometer used, and on the other hand these information might be used to calibrate the deuterium and hydrogen ratio in the plasma excited under investigation. For this, the organic compound urea (chemical formula: $CO(NH_2)_2$) in a hydrogen and deuterium version is analyzed in various mixing ratios. The white powder is mixed and pressed to a pellet of diameter 10 mm and 5 mm height. In fig. 6.11 the detected Balmer-α lines with the high resolution spectrometer (gate delay 0.8 µs and width 1 µs) of two samples are shown. The used laser exhibits the same parameters as in the experiment on tungsten and it is also executed in an argon environment at atmospheric pressure. Here, the mixing ratios of 20 : 80 and 50 : 50 (H/D) are compared. The presented data are accumulations of 200 detected signals (five consecutive irradiations at 200 different positions). A first observation is the significant discrepancy in line broadening similar to the measurement on the tungsten tile resulting from the deviating mass of deuterium and hydrogen. Moreover, the detected signal is dominated by the hydrogen line, which indicates a relatively high hydrogen contamination of the sample on the surface and in the bulk due to the manufacturing process. Nevertheless, it can be shown that the contribution of deuterium atoms to the plasma (in absolute detector counts) depends on the deuterium amount in the analyzed samples.

6.3 Conclusion and Outlook

In this chapter, the focus was on the analysis of hydrogen isotopes in PFC relevant material tantalum and tungsten. Two different approaches were presented, a nanosecond laser in a vacuum environment and a femtosecond laser operating in argon at atmospheric pressure. These completely deviating circumstances make it impossible to compare the results. Still both approaches contain the information that the deuterium retention in the tiles under investigation only contributes in the first laser irradiation on the surface to the detected spectrum. The experiments described, present the use of femtosecond and nanosecond LIBS as diagnostic techniques to analyze the hydrogen isotope impurities in metallic samples that are used as PFCs in confinement fusion experiments. With an ablation rate of 600 nm per pulse and a beam diameter of 20 µm, deuterium and hydrogen can be detected with this method. Here, the limitation of femtosecond LIBS can be observed compared to studies with picosecond lasers that provide a higher pulse energy. In particular, the studies by Oelmann et al. (2021, ref. [99]) exhibit a depth resolution of 30 nm in a double-pulse configuration. Nevertheless, the applied CF-LIBS method is an interesting quantitative approach to estimate the total deuterium content in the investigated tungsten tiles and is even more significant due to the use of the femtosecond laser. The estimated deuterium content of approximately 1.7 at% using this method is close to the expected quantity in the tungsten tiles that were exposed to the given deuterium plasma. Moreover, similar concentrations of hydrogen retention were found like in the comparable study by Pardede et al. (2021, ref. [100]). Further studies on this approach with tiles of varying deuterium content would be the next logical step to develop this method and to determine the limit of detection.

Summing up the presented studies, the use of a femtosecond lasers can bring important depth resolved information on hydrogen and deuterium content in versatile sorts of samples from metallic alloys to organic compounds. A crucial issue in all those experiments is a low intensity of the detected spectra, as it is necessary to choose a long gate delay and a high number of accumulations to be able to resolve the isotopic spectral shift. One solution might be the use of lower pressure of the ambient gas as for example presented in ref. [101]. Other studies like ref. [55], [102], [103] and the presented experiments in chapter 5.2 illustrate that the use of double-pulses might help to increase the detected spectral intensity. However, it has been shown that femtosecond based LIBS diagnostics can be used in a quantitative approach to detect minor elements stored in PFCs. In conclusion, these findings need to be transferred to applications in a vacuum environment to be able to serve as a relevant diagnostic tool inside of the fusion device vessels.

Chapter 7

Summary and Conclusion

The initial motivation of starting this work in 2019 was to give an assessment on the applicability of femtosecond laser pulses in a LIBS diagnostic on plasma-facing components of magnetic confinement fusion vessels to analyze material composition and hydrogen isotope impurities. Hereafter, the presented experiments in this work are summarized and reviewed with regard to this question. In the end, a concluding discussion on the feasibility of fs-LIBS under these circumstances is given consulting the findings from optical emission spectra induced by three different laser systems.

The task mentioned has initially been approached by comparing the fluence dependent ablation features of three different laser sources on tantalum, which works as a surrogate material to represent the PFCs in this context. The lasers used operate with pulse duration in the range of nanoseconds, picoseconds, and femtoseconds. Although the deviating laser parameters of the three systems in this experiment make a direct comparison of ablation threshold fluence unfeasible, the fundamental differences in the ablation characteristics are demonstrated clearly. According to the experiments presented, it has been shown that much lower pulse energies are necessary to create craters of comparable ablation depth when the pulse duration is reduced. This is well aligned with findings from common literature on laser-induced ablation processes. Moreover, ablated femtosecond craters exhibit less re-solidification of molten material compared to the nanosecond crater, which has been identified as evidence for better defined ablation yield for shorter laser pulses. This effect has been traced down to the reduced Heat Affected Zone (HAZ) in the bulk material by ultra-short pulses that might lead to a higher possible depth resolution in the material composition analysis of PFCs.

The ensuing studies emphasize the use of ultra-short sub-10-fs laser pulses to find experimental conditions for LIBS experiments in vacuum conditions. First, the spatial expansion of a tantalum plasma excited by 8 fs near IR laser pulses from the PHASER system is investigated. With laser intensity dependent images of the optical emission from the expanding plasma, optimal conditions for a bright plasma source have been found to range from 10^{14} to $10^{15}\,\mathrm{Wcm}^{-2}$. Here, time resolved investigations suggest a time-frame within the first 200 ns after the laser surface interaction to detect the characteristic atomic and ionic spectral lines, to avoid the continuum radiation of ablated clusters and nanoparticles from the surface. With

the new spectrometer provided by the German Research Foundation, it was possible to investigate the spectral composition of the expanding tantalum plasma. It turns out that the proposed time-frame of atomic line emissions in the first 200 ns after the laser-surface interaction was confirmed by using similar laser intensities. In addition, a more detailed diagnosis of a copper plasma induced by the same laser with varying intensity has been presented. In this context, a minimal laser intensity of $\sim 10^{16}\,\mathrm{Wcm}^{-2}$ has been found that is necessary to excite ionic emission lines to contribute to the detected spectrum.
Further steps towards a high resolution diagnostic regarding composition analyses and hydrogen isotope detection includes reducing laser intensity below $10^{16}\,\mathrm{Wcm}^{-2}$. By ablating a way smaller yield from the surface, and the reduction of plasma temperature, due to the lower intensity, the plasma emission signal decreases until the detection limit is reached. This work suggests the use of a collinear pre-pulse system to enhance the emitted spectral lines from the plasma. In particular, a pre-pulse of 1 % pulse energy with respect to the main pulse is used, while the main pulse is delayed by up to 800 ps. The resulting spectra from copper and tantalum reveal that this configuration indeed is able to enhance the spectral intensity and can even decrease the laser intensity necessary to excite the ionic copper lines by one order of magnitude. The use of such a configuration is promising in fs-LIBS analyses, which usually operate with high lateral and depth resolution ablating yields of masses in the micro-grams (µg) regime. Further studies might investigate, which pre-pulse setup is the most promising in this context. Although a few predictions are traced from the findings presented, the experimental results do not allow a final conclusions on the principle of the enhancement mechanism. In the end, it might be do to a combination of optimized coupling conditions of the ultra-short laser to the pre-ignited surface near plasma and a reheating process. A higher temperature of the excited copper plasma can be an evidence for both processes.
Apart from the high resolution material composition analysis using sub-10-fs pulses, the detection of hydrogen isotope impurities in tantalum and tungsten tiles by optical emission spectroscopy has been pursued in this work. For this purpose, the outcome of two main experiments are presented. First, a nanosecond laser is used in a vacuum environment to analyze the tantalum after the exposition to a deuterium plasma in the PSI-2 facility. After that, similarly prepared tungsten samples are investigated by a femtosecond laser in an argon environment. In the nanosecond experiment, typical challenges for realizing a reasonable LIBS setup and difficulties in the analysis of generated spectra are pointed out. In particular, it has been shown that single pulses lead to the outgassing of the whole amount of hydrogen and deuterium deposited around the laser interaction area on the samples investigated. In addition, the investigation of tantalum as a surrogate material made it difficult to extract quantitative statements from the Balmer-α emission detected, as it is superposed by three atomic tantalum lines. Consequently, another surrogate material is used in the next step. Here, tungsten is a suitable candidate, although the amount of deuterium retention proposed might be lower compared to the tantalum sample. The ensuing femtosecond LIBS experiment in argon at atmospheric pressure brings the opportunity to quantify the amount of hydrogen isotopes in the ablation yield from the tungsten surface. Here, a calibration free

LIBS approach is presented that displays a deuterium amount close to the expected value of 1 at% to 2 at%. This is also the amount of tritium anticipated in the plasma-facing walls of the upcoming magnetic confinement fusion experiment ITER. Note that the high depth resolution pursued on the order of the optical penetration depth ($\sim 10\,\mathrm{nm}$) is not achieved, because the contribution of deuterium was not detectable in the emission spectrum for lower laser fluences than $31\,\mathrm{Jcm^{-2}}$. As a solution, a higher number of accumulations where necessary to be able to detect a sufficient deuterium Balmer-α emission line signal.

Now, concluding statements on the feasibility of femtosecond LIBS in the context of *in-situ* hydrogen-isotope detection might be apposite: The advantages of femtosecond laser pulses in the ablation process leading to a much lower heat affection zone and a well defined ablation crater has been pointed out by the experiments presented in this thesis. Here, LIBS analyses of the material tantalum has been carried out with depth resolutions of 30 nm to 100 nm using the two different femtosecond lasers in this thesis. As soon as the composition of minor elements in the sample matrix has to be investigated, especially the impurity of light, low-concentration, elements like deuterium, the fs-LIBS technique reaches its limit with regard to the small ablation yield. It might be possible with a higher pulse energy and a larger laser spot on the surface to excite enough of those elements to be detectable. Even in this setup, it might be necessary to accumulate many signals from different fresh positions to detect the minor elements with a sufficient accuracy. Ways to enhance the plasma emission were shown and discussed using different ambient environment than vacuum or a second laser pulse either collinear or orthogonal to the plasma expansion. The most promising technique might be a collinear double-pulse system, as it would be easiest to apply to a LIBS setup applied to a remote handling arm inside of a fusion vessel. Nevertheless, the low pulse energy is the biggest disadvantage of femtosecond laser systems in this context. Despite the complex amplification stage of the PHASER system, the output laser energy is one to two orders of magnitude below the energy of the picosecond and nanosecond lasers applied in this work. According to those circumstances, it might be the wisest compromise to use picosecond laser systems for the aspired application, as the pulse energy is reasonable and the heat affection is still limited compared to longer laser pulses. Still, femtosecond lasers would be more precise tools in material analyses, where the size of the emitting plasma plume is not a limiting factor, because the collection system can be placed close to the source. Moreover, when more precise diagnostic techniques like for example residual gas mass spectroscopy come into play, a femtosecond laser might be the better choice. It can be used to detect minor elements in unknown alloys, determine the composition of layered targets, or be applied in the diagnostic of hydrogen impurities in ex-situ applications.

Appendix A

Two-Temperature Model

In chapter 2.2.1 a Two-Temperature Model (TTM) based on a lattice and electron subsystem is used to understand the coupling of the ultra-short laser pulse and the material. Moreover, it is applied in section 4.4 to simulate the laser ablation process on tantalum. For the solution of the coupled differential equations to model the heat diffusion of electron and lattice subsystem in equation (2.20) given in chapter 2.2.1, a Forward Time Centered Space (FTCS) scheme with *von Neumann* boundary conditions on the laser faced side and a fixed value of room temperature on the rear side is used. In the presented cases the intensity has a Gaussian shape in time with an initial interaction time t_0 and a pulse duration τ and is given as

$$I(t) = I_0 \exp\left[-4\log 2\left(\frac{t-t_0}{\tau}\right)^2\right]. \tag{A.1}$$

The thermophysical material parameters like electron and lattice heat capacity C_e and C_l, electron-phonon coupling term G, reflectivity R, and the electron thermal conductivity κ_{el} are all temperature dependent and will be explained in the following abstracts. These properties are updated in each time step with respect to the electron- and lattice temperature along the simulation grit. For all these calculations it can be distinguish between a low and a high temperature regime. This limit is similar to the Debye temperature $T_D = \hbar\omega_D/k_B$ that is limited by the total number of phonon modes N within the Debye sphere with cut-off frequency ω_D.

The temperature dependent quantities C_l, C_e, κ_{el}, G, and R, which are needed to calculate the heat transfer are described following ref. [104] and [105] in this chapter. In general, the atoms in a solid are arranged in different lattice configurations with an individual likelihood of mobility depending on material properties. Excitation of these lattices expresses in collective modes within the lattice subsystem. The properties of these modes (direction and energy) are considered as quasi particles called phonons. A phonon is described by its frequency ω and wavevector $\vec{q}$, and its energy is given as

$$\begin{aligned} \epsilon &= \hbar\omega \\ \omega &= v_s|\vec{q}|. \end{aligned} \tag{A.2}$$

Here v_s is the material dependent sound velocity. Phonon energy distribution follows a Bose-Einstein statistic and is given with the Boltzmann constant k_B as

$$n(\omega) = \frac{1}{e^{\hbar\omega/k_B T} - 1}. \tag{A.3}$$

With this information it is possible to calculate the lattice heat capacity C_l following the Debye-model.

Lattice Heat Capacity C_l

As the total number of phonon modes N is limited, the allowed wave vector is given in a so-called Debye sphere with a cut-off frequency ω_D and wave vector $q_D = \omega_D/v_s$. The volume of each allowed wave vector is given in a cube of edge length L as

$$\left(\frac{2\pi}{L}\right)^3 = \frac{8\pi^3}{V}. \tag{A.4}$$

Here the number of modes is defined as

$$N = \left(\frac{4}{3}\pi q_D^3\right)\left(\frac{8\pi^3}{V}\right)^{-1} \tag{A.5}$$

and the Debye temperature $T_D = \hbar\omega_D/k_B$. From the given energy distribution and the density of state

$$D(\omega) = \frac{\mathrm{d}N}{\mathrm{d}\omega} = \frac{V\omega^2}{2\pi^2 v_s^3} \tag{A.6}$$

the thermal energy is calculated for each polarization (one longitudinal and two transversal modes) as

$$U = \int D(\omega) n(\omega) \hbar\omega \, \mathrm{d}\omega. \tag{A.7}$$

Using the expressions for the density of state and Bose-Einstein distribution the combination of the three polarization (assuming independent v_s on the mode) the energy is given as

$$U = \frac{3V\hbar}{2\pi^2 v_s^2} \int_0^{\omega_D} \frac{\omega^3}{e^{\hbar\omega/k_B T} - 1} \, \mathrm{d}\omega. \tag{A.8}$$

By substitution of $x = \hbar\omega/k_B T$ and $x_D = T_D/T$ an expression for the lattice heat capacity can be given as

$$C_l = \frac{\partial U}{\partial T} = 9Nk_B \left(\frac{T}{T_D}\right)^3 \int_0^{x_D} \frac{x^4 e^x}{(e^x - 1)^2} \, \mathrm{d}x. \tag{A.9}$$

This expression is saturating to $C_l = 3Nk_B$ in the high temperature case ($T \gg T_D$) and is proportional to $\propto T^3$ in the low temperature case ($T \ll T_D$).

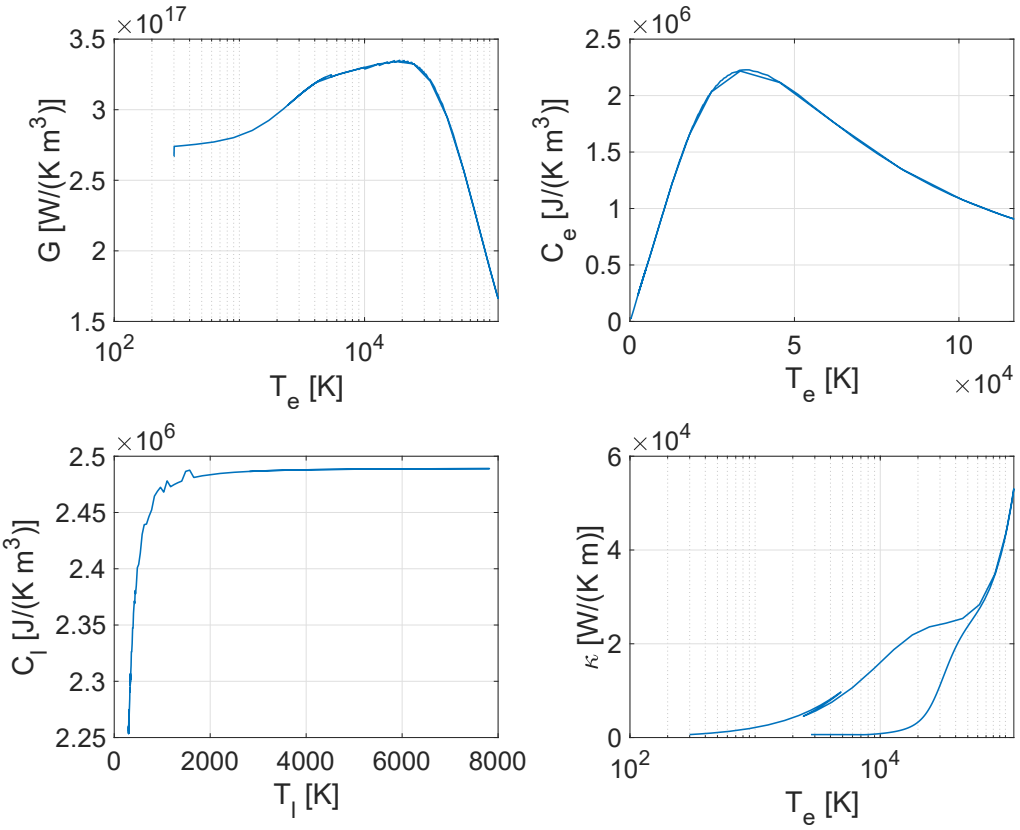

Figure A.1: Thermophysical properties (coupling constant G, electron and lattice heat capacity C_e and C_l) of aluminum for different temperatures T_e and T_l. Output created from a TTM simulation, where T_e and T_l are changing with time. The electron temperature first rises from 300 K to 10^5 K and decreases back to 300 K.

Electron Heat Capacity C_e

The description of the metal given by Einstein and Debye

$$C_{metal} = C_e + C_l \propto T + T^3 \tag{A.10}$$

holds in the low temperature case. In this case the Sommerfeld expansion is used and a linear dependence on electron temperature holds as $C_e(T_e) = \gamma T_e$ with $\gamma = \pi^2 k_B^2 D(\epsilon_F)/3$ defined with density of state value at fermi energy ϵ_F. At high electron temperatures the Sommerfeld expansion does not hold anymore. Due to the fermi distribution of the electrons within the free electron gas given as

$$f(\epsilon, \mu, T_e) = \left[\exp\left(\frac{\epsilon - \mu}{k_B T_e}\right) + 1\right]^{-1} \tag{A.11}$$

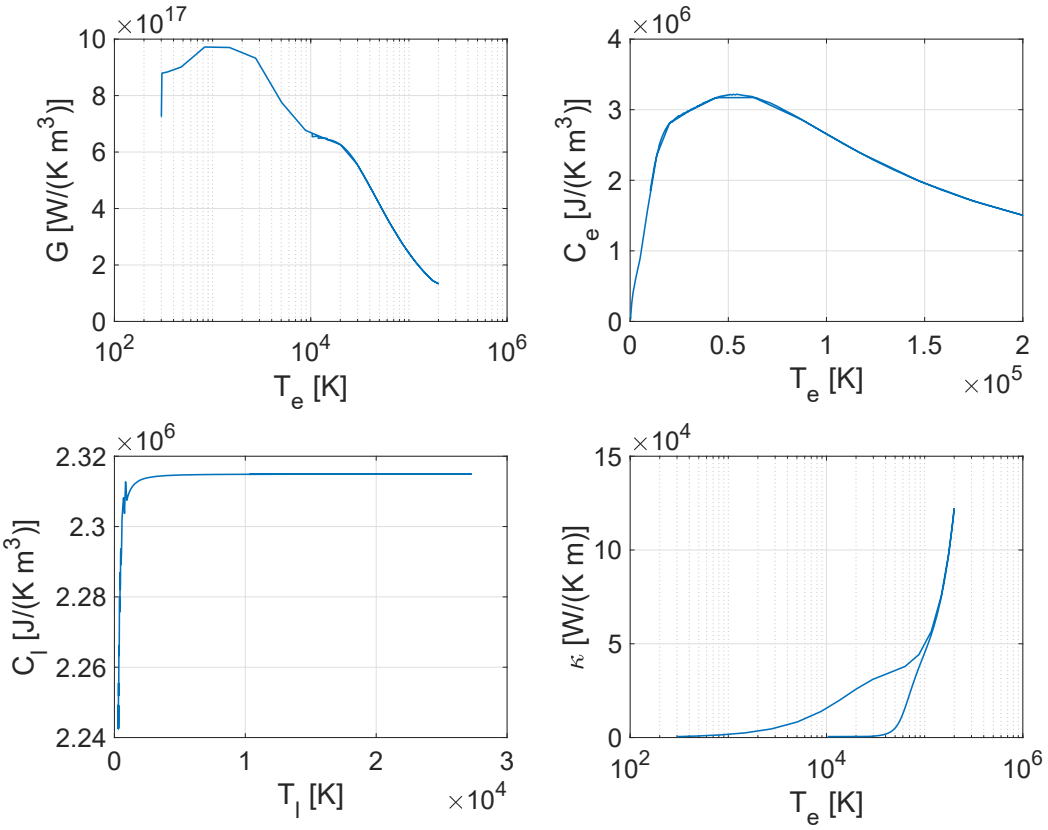

Figure A.2: Thermophysical properties (coupling constant G, electron and lattice heat capacity C_e and C_l) of tantalum for different temperatures T_e and T_l. Output created from a TTM simulation, where T_e and T_l are changing with time. The electron temperature first rises from 300 K to 10^5 K and decreases back to 300 K.

the heat capacity is calculated as

$$C_e(T_e) = \int_{-\infty}^{\infty} \frac{\partial f(\epsilon, \mu, T_e)}{\partial T_e} D(\epsilon)\epsilon \, \mathrm{d}\epsilon. \tag{A.12}$$

The temperature dependent chemical potential $\mu(T_e)$ can be gained by making use of the conservation of total number of electrons N_e that is given as

$$N_e = \int_{-\infty}^{\infty} f(\epsilon, \mu(T_e), T_e) D(\epsilon) \, \mathrm{d}\epsilon. \tag{A.13}$$

Thermal Conductivity κ_{el}

The heat transport in the two subsystems is described by the thermal conductivity κ_{el} and is defined by the electron-electron and electron-phonon collision frequencies ν_{ee} and ν_{eph}. Using $\nu = \nu_{ee} + \nu_{eph}$ the thermal conductivity in a solid can be expressed as

$$\kappa_{el} = \frac{1}{3} \cdot \frac{C_e v^2}{\nu}. \tag{A.14}$$

Here v^2 is the electron mean square velocity. Equation (A.14) is derived as

$$\kappa_{el}(T_e, T_l) = \frac{1}{3} v_F^2 \frac{C_e}{AT_e^2 + BT_l}, \tag{A.15}$$

using material constants A and B defined as

$$\begin{aligned} A &= \frac{A' k_B^2}{h \epsilon_F} \\ B &= \frac{2\pi k_B \lambda}{h}. \end{aligned} \tag{A.16}$$

A' is a dimensionless constant between 1 and 10 and λ is the electron-phonon mass enhancement parameter. Considering temperatures larger than the fermi temperature a more general expression for the thermal conductivity can be derived as

$$\kappa_{el} = K \cdot \frac{(\theta_e^2 + 0.16)^{5/4}(\theta_e^2 + 0.44)\theta_e}{(\theta_e^2 + 0.092)^{1/2}(\theta_e^2 + b\theta_l)} \tag{A.17}$$

with $\theta_e = k_B T_e / \epsilon_F$ and $\theta_l = k_B T_l / \epsilon_F$. The parameters K and b are material constants that can be derived from A and B at the fermi edge $T = T_F$.

Coupling Constant G

A general expression for the electron-phonon coupling factor is given as

$$G(T_e) = \frac{\pi \hbar k_B \lambda \langle \omega^2 \rangle}{D(\epsilon_F)} \int_{-\infty}^{\infty} D^2(\epsilon) \left(-\frac{\partial f}{\partial \epsilon} \right) \, \mathrm{d}\epsilon. \tag{A.18}$$

Here $\langle \omega^2 \rangle$ is given as the second moment of the phonon spectrum explained by McMillian et al. (1967) (ref. [106]).

Reflectivity R

In many studies (e.g. ref. [79]) the Drude-Lorentz model is assumed to hold in the description of the optical response of the free electrons in a metal. The permittivity in this case is equal to

$$\begin{aligned} \epsilon &= \epsilon_{Drude} + \epsilon_{Lorentz} \\ &= \left[1 - \frac{f_0 \omega_p^2}{\omega(\omega - i\nu)} \right]_D + \left[\sum_{j=1}^{k} \frac{f_j \omega_p^2}{\left(\omega_j^2 - \omega^2 \right) + i\omega\Gamma_j} \right]_L . \end{aligned} \tag{A.19}$$

The Drude part is described by the plasma frequency ω_p, oscillator strength f_0, collision rate ν and the laser frequency ω and the Lorentz part by the same values excited by inter-band transition j with the scattering rate of harmonic bound electrons Γ_j in addition. The plasma frequency is given by the electron density n_e, mass m_e, elemental charge e and vacuum

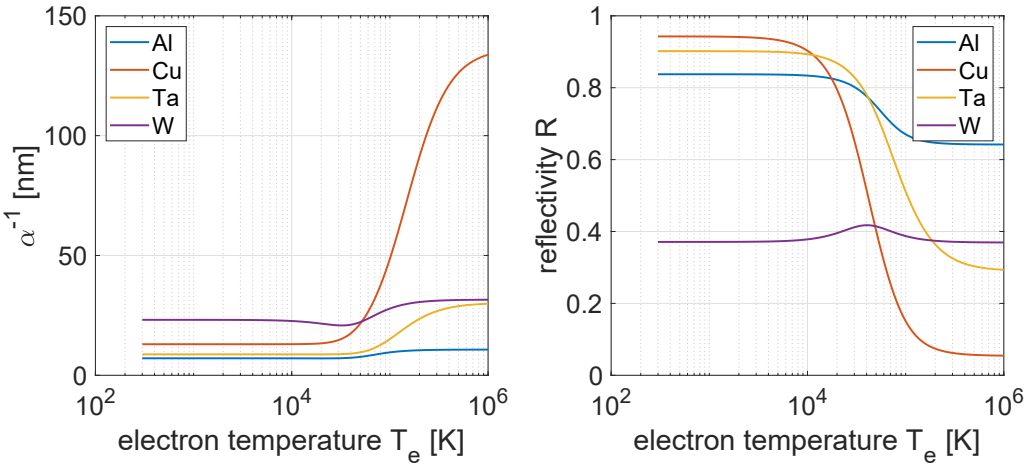

Figure A.3: (left) Temperature dependent optical penetration depth α^{-1} and (right) reflectivity R for $\lambda = 790\,\mathrm{nm}$ determined by the Drude-Lorentz model for an angle of incidence of $\Theta = \pi/4$.

permittivity ϵ_0 as

$$\omega_p = \sqrt{\frac{n_e e^2}{\epsilon_0 m_e}}. \tag{A.20}$$

The corresponding quantities for various materials can be found in ref. [107] and [76]. Here, $\nu = \nu_{ee} + \nu_{eph}$ is given as the collision rate that is dominated by the electron-phonon rate

$$\nu_{eph} = \frac{3}{2} C_\omega \frac{k_B T_i}{\hbar}. \tag{A.21}$$

from Debye temperature up to the melting point. C_ω is a dimensionless proportionality coefficient. For high temperaturesis is described by the electron-electron rate

$$\nu_{ee} = \frac{\pi^4 k_B^2 \sqrt{3}}{256} \frac{\omega_p}{\epsilon_F^2} T_e^2. \tag{A.22}$$

From this model the reflectivity R can calculated by the complex dielectric function $\epsilon = \epsilon_r + i\epsilon_i = (n + ik)^2$ using Fresnel equation with an incidence angle Θ as

$$R = \left| \frac{n_1 \sqrt{1 - \left(\frac{n_1}{n_2} \sin\Theta\right)^2} - n_2 \cos\Theta}{n_1 \sqrt{1 - \left(\frac{n_1}{n_2} \sin\Theta\right)^2} + n_2 \cos\Theta} \right|^2. \tag{A.23}$$

Note that $n_1 = 1$ is the refractive index of vacuum and $n_2 = \sqrt{\epsilon}$ of the material. In this approximation the full electronic structure of the metal and the density of state is not necessary. Following this model the reflectivity and the optical penetration depth $\alpha^{-1} = \lambda/(4\pi k)$ are calculated for some materials (W, Ta, Cu, and Al) that are used in the presented experiments in fig. A.3. All necessary parameters to calculate the temperature dependent material properties presented in this chapter are given in table A.1.

material	aluminum	copper	tantalum	tungsten
element	Al	Cu	Ta	W
lattice conf.	fcc	fcc	bcc	bcc
const. a [pm]	404	360	330	316
mass of atom [u]	26.96	63.55	180.95	183.84
Z	13	29	73	74
n_{atom} [m^{-3}]	6.02×10^{28}	8.47×10^{28}	5.60×10^{28}	6.32×10^{28}
ω_p [s^{-1}]	2.28×10^{16}	5.44×10^{16}	2.99×10^{16}	2.01×10^{16}
N_e	3	1	5	2
ϵ_F [eV]	11.7	7.0	15.6	9.2
T_D [K]	428	345	240	405
λ	0.45^b	0.08^a	0.877^c	0.28^b
$\lambda\langle\omega^2\rangle$ [meV^2]	185.9^b	377^a	180.4^c	112^a
H_v [kJ/mol]	284	313	753	774
ρ [g/cm^3]	2.7	8.92	16.65	19.25
T_{crit} [K]	7963^d	6550^e	8865^f	12466^g
ρ_{crit} [g/cm^3]	2.75^d	1.895^e	1.9^f	6.99^g
α @1064 nm [cm^{-1}]	1.25×10^6	8.2×10^5	1.16×10^6	4.38×10^5
R @1064 nm	0.93	0.97	0.95	0.49
α @790 nm [cm^{-1}]	1.41×10^6	1.14×10^6	1.15×10^6	4.32×10^5
R @790 nm	0.84	0.94	0.90	0.37
α @355 nm [cm^{-1}]	1.55×10^6	6.93×10^5	1.13×10^6	8.96×10^5
R @355 nm	0.90	0.34	0.55	0.34
α @343 nm [cm^{-1}]	1.55×10^6	6.79×10^5	1.14×10^6	9.26×10^5
R @343 nm	0.90	0.31	0.53	0.34

Table A.1: Relevant properties to calculate the thermophysical parameters of the observed materials. Standard data are taken from NIST database and R and α values are calculated by the Drude-Lorentz model at room temperature with an angle of incidence of $\Theta = \pi/4$ for all used laser wavelengths in the presented experiments. The electron-phonon coupling constants λ are taken from the following references: a: Ref. [108], b: Ref. [104], c: Ref. [109]. The critical point data are taken from: d: ref. [110], e: Ref. [111], f: Ref. [112] and g: Ref. [113]

Appendix B

Spectrometer Details

Spectrometer	Detector	f [mm]	$F\#$	Gratings [l/mm]	$R = \lambda/\Delta\lambda$	$\Delta\lambda_{BW}$ [nm]
Kymera328i	iStar	328	4.1	300	1500	270
				1200	6400	62
				1800	11000	36
IsoPlane320	PIMAX	320	4.6	300	1400	280
				1800	11000	37
				2400	19000	21
Shamrock750	iStar	750	9.7	150	1700	236
				1200	14500	27
				2400	43400	9
Horiba 1250M	iStar	1250	9	1200	24000	16
				2400	73000	5

Table B.1: Overview of all used spectrometers and camera devices with specified f-number $F\#$ and focal length f. The resolution R and bandwidth $\Delta\lambda_{BW}$ are calculated at central wavelength 656 nm and a slit width of 30 µm respectively.

In this part typical values of thespectrometers used taken from the specification sheets are presented in table B.1. The resolution R and bandwidth $\Delta\lambda_{BW}$ parameters are calculated with the formulas presented in chapter 3.3.1. Moreover, the sensitivity and wavelength calibration of the spectrometers are presented. In addition, the instrumental broadening is estimated using a low pressure Hollow Cathode Lamp (HCL) with a iron (Fe) core. For the *IsoPlane320* spectrometer with the 1800 l/mm grating the measurement is shown in fig. B.1. The instrumental broadening manifests in a Gaussian shaped peak. Here, pseudo-Voigt fits to Fe-I lines at 654.61nm, 659.31 nm and 667.81 nm are taken and their Gaussian width plotted with respect to the central wavelength. A linear dependence of w_{inst} on the wavelength is assumed so that the instrumental width at 656.28 nm can be estimated as $w_{\text{inst}} = 52.3$ pm. Note that the sensitivity of the spectrometer and camera sensor varies over the spectral range as it is wavelength dependent. A calibration halogen lamp with known relative spectral intensity can be used to determine the actual intensity of the spectral lines measured. This is important, when relative line intensities are compared in calibration free methods that take into account the temperature measured by the Boltzmann plot method. For this context,

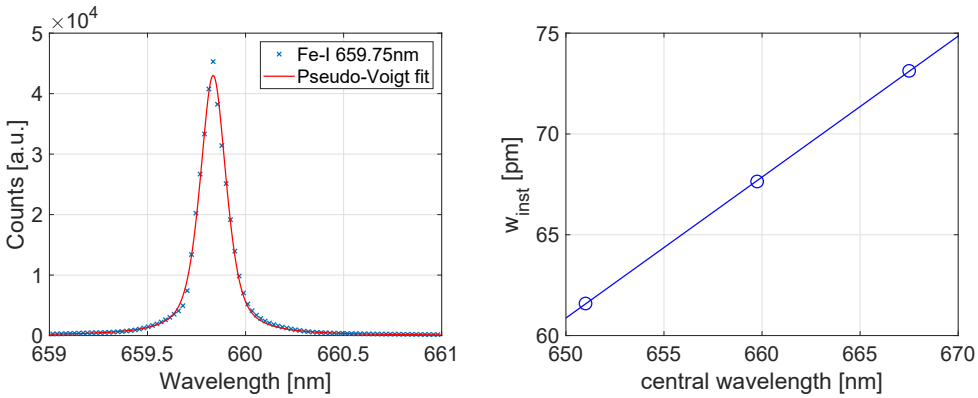

Figure B.1: (left) Pseudo-Voigt fit to the low pressure Fe-lamp line at 659.75 nm. (right) Gaussian width parameter of the pseudo-Voigt fits to three different atomic Iron (Fe-I) lines and a linear extrapolation respectively.

the emission from a halogen lamp with known reference spectrum is detected using the same grating settings as for the plasma emission experiment. Taking the ratio of the measured and reference spectrum leads to the corresponding wavelength dependent correction factors.
A spectral calibration needs to be executed for each used grating using the characteristic lines of a Hg or Ne lamp. Here, lines of farthest possible spectral distance are used to assign the pixel values on the camera chip for different grating angles. For example the Hg lines at 253.7 nm and 579.1 nm can be used in this context. In a first approach the offset of a single line from the assigned wavelength need to be executed. All other wavelengths will be adjusted linearly, which in total is a first order calibration routine. Afterwards some lines at the far edges of the spectrum might still be off or unbalanced. For this a second order routine adjusts the dispersion values that are influenced by exact focal length, inclusion angle and detection angle of the spectrograph. The software of the commercial spectrometers provide routines to adapt the nominal dispersion.
In chapter 3.4.2 the Boltzmann plot method is described. For this method information about emission characteristics of decent spectral lines are necessary to determine the plasma temperature. In the database from the National Istitute of Standards and Technology (NIST) these parameters are commonly available (ref. [87]). In table B.2 necessary parameters of selected spectral lines of analyzed material in this thesis are given.

Species	λ_{ki}[nm]	A_{ki}[s^{-1}]	Acc.	g_k	E_i[eV]	E_k[eV]
Ta-I	481.275	1.2×10^6	$\leq 10\%$	4	0.000000	2.575439
Ta-I	482.543	2.63×10^5	$\leq 7\%$	6	1.394032	3.962711
Ta-I	483.219	1.70×10^6	$\leq 7\%$	4	1.236843	3.801933
Ta-I	485.217	1.65×10^6	$\leq 7\%$	4	1.357654	3.912184
Ta-I	488.3950	1.11×10^6	$\leq 7\%$	8	1.147279	3.685176
Ta-I	490.460	1.95×10^6	$\leq 18\%$	10	1.873915	4.401148
Ta-I	492.127	1.18×10^6	$\leq 10\%$	4	0.750032	3.268681
Ta-I	492.601	1.53×10^6	$\leq 10\%$	4	0.752449	3.268681
Ta-I	645.036	2.20×10^6	$\leq 7\%$	10	1.516917	3.438507
Ta-I	645.583	1.45×10^5	$\leq 7\%$	4	1.147279	3.067249
Ta-I	648.537	5.8×10^6	$\leq 7\%$	10	1.1655369	3.566610
Ta-I	650.552	6.0×10^6	$> 50\%$	6	2.559845	4.465163
Ta-I	651.439	2.15×10^6	$\leq 7\%$	4	1.394032	3.296744
Ta-I	651.610	1.25×10^6	$\leq 7\%$	8	1.394032	3.296235
Ta-I	661.195	1.88×10^6	$\leq 18\%$	4	1.394032	3.268681
Ta-I	662.130	3.03×10^6	$\leq 10\%$	6	0.752449	2.624449
W-I	484.381	1.9×10^6	$\leq 10\%$	5	0.412313	2.971240
W-I	488.690	8.1×10^5	$\leq 10\%$	11	0.771099	3.307462
W-I	495.308	8.3×10^5	$\leq 10\%$	5	2.458319	4.960794
W-I	500.615	1.2×10^6	$\leq 10\%$	7	0.771099	3.247047
W-I	501.530	5.4×10^5	$\leq 10\%$	9	0.598844	3.070269
Cu-I	510.550	2.0×10^6	$\leq 18\%$	4	1.388948	3.8166920
Cu-I	515.320	6.0×10^7	$\leq 18\%$	4	3.7858977	6.1911751
Cu-I	521.820	7.5×10^7	$\leq 18\%$	6	3.8166920	6.1920252
Cu-I	522.010	1.5×10^7	$\leq 18\%$	4	3.8166920	6.1911751
Cu-I	529.250	1.09×10^7	$\leq 18\%$	8	5.395050	7.737027
Cu-II	490.973	2.04×10^8	$\leq 7\%$	13	14.32872921	16.85329783
Cu-II	491.838	2.9×10^8	$\leq 25\%$	9	14.59881086	17.1189425
Cu-II	493.16982	1.9×10^8	$\leq 25\%$	11	14.34033006	16.85365501
Cu-II	495.372	3.1×10^8	$\leq 25\%$	11	14.61564148	17.1177912
Cu-II	498.550	9.7×10^7	$\leq 18\%$	9	14.39211349	16.87831334
H-β	486.135	8.42×10^6	$\leq 0.3\%$	32	10.1988358	12.7485393
H-α	656.280	4.41×10^7	$\leq 0.3\%$	18	10.1988358	12.0875052

Table B.2: Spectroscopic parameters of selected lines from neutral hydrogen (H-I), tantalum (Ta-I), tungsten (W-I), and atomic and ionic copper (Cu-I, Cu-II) taken from the atomic spectra database NIST [87]. Here, the transition wavelength λ_{ki} from the upper energy level E_k to the lower level E_i are given with the corresponding transition probabilities A_{ki} and statistical weights g_k including the corresponding accuracy.

Appendix C

Pseudo-Voigt Fit

In the presented CF-LIBS approach in chapter 6.4, the exact spectral line shape of the isotopic shift in fig. C.1 is of main interest to identify the correct hydrogen and deuterium ratio and corresponding plasma parameters. Here, more insights to the used pseudo-Voigt fitting function that is used in different experiments are given. As mentioned in the methods part, the fitting follows the routine in ref. [60]. Here, the pseudo-Voigt function is given as a linear superposition of a Lorentz ($L(x, f_L)$) and a Gaussian ($G(x, f_G)$) function as

$$V(f_L, f_G) = \eta \cdot L(x, f_L) + (1 - \eta) \cdot G(x, f_G). \tag{C.1}$$

Here η is a weighting parameter given as

$$\eta = 1.36603 \cdot \frac{f_L}{f} - 0.47719 \cdot \left(\frac{f_L}{f}\right)^2 + 0.11116 \cdot \left(\frac{f_L}{f}\right)^3, \tag{C.2}$$

where f is given as

$$f = (f_G^5 + 2.69269 \cdot f_G^4 \cdot f_L + 2.42843 \cdot f_G^3 \cdot f_L^2 + ... \\ 4.47163 \cdot f_G^2 \cdot f_L^3 + 0.07842 \cdot f_G \cdot f_L^4 + f_L^5)^{1/5}. \tag{C.3}$$

Note that f_G and f_L are the FWHM of the Gauss and Lorentz part that are given as

$$G(x, f_G) = \frac{2\sqrt{\ln 2}}{f_G\sqrt{\pi}} \cdot \exp\left(-4 \ln 2 \frac{x^2}{f_G^2}\right) \tag{C.4}$$

and

$$L(x, f_L) = \frac{f_L}{2 \cdot \pi \cdot (x^2 + (f_L/2)^2)} \tag{C.5}$$

respectively. For the fit-function of the two isotopes

$$F(\lambda) = h \cdot V(f_{G,H}, f_{L,H}, \lambda - \lambda_H) + d \cdot V(f_{G,D}, f_{L,D}, \lambda - \lambda_D) + b \tag{C.6}$$

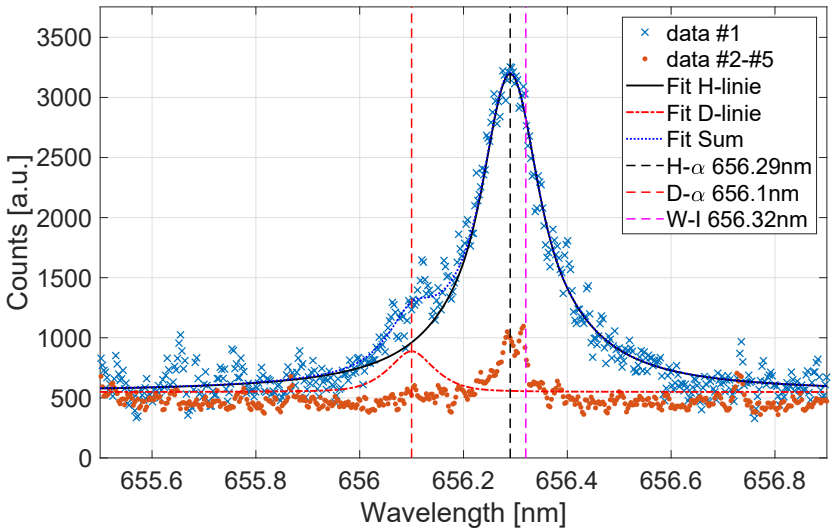

Figure C.1: Pseudo-Voigt fit on Hydrogen and Deuterium spectral line detected in tungsten (see fig. 6.9 and compare ref. [93]).

is used with $f_{G,H}$, $f_{G,D}$, $f_{L,H}$, $f_{L,D}$, h, d and the offset b as fitting parameters with fixed central wavelengths $\lambda_H = 656.28\,\text{nm}$ and $\lambda_D = 656.1\,\text{nm}$, when V is a normalized function. The calculated fitting parameters are given with a 95 % confidence bound as $f_{G,H} = 0.08635\,\text{nm}$, $f_{G,D} = 0.1184\,\text{nm}$, $f_{L,H} = 0.2025\,\text{nm}$, $f_{L,D} = 0.08784\,\text{nm}$, $h = 2648$, $d = 339.5$, and $b = 548.2$. From this fit the plasma parameters can be extracted as described and the hydrogen-deuterium composition is calculated by the ratio of the integrals over the two pseudo-Voigt functions.

Appendix D

Technical Description of the Pre-Pulse Module

Below, the most important technical aspects of the designed pre-pulse module introdcued in chapter 3.1 are described concerning the mechanical specifications of the motorized linear stage. In this context, detailed descriptions of the geometrical challenges in aligning the two beam arms and adjusting the optical delay stage are given.
The module is added to the beam path of the PHASER system, before the laser pulse is guided to the mirror-compressor inside the vacuum chamber. Here, a movable stage with the entrance to the pre-pulse module can be added to the beam path. In fig. D.1 the final version of the designed pre-pulse module is shown including the stage with beamsplitter BS1, mirror M1 and M7. In the pre-pulse configuration the first beamsplitter is a glass substrate that reflects 10 % of the incoming s-polarized beam and the second realigning beamsplitter is another glass substrate with a thin gold layer that reflects 90 % of the incoming beam. The 3 mm thick fused silica substrates are manufactured by *Laser Components* and coated with an anti-reflective layer ($R < 1\,\%$ between 600 nm and 900 nm) on the back-side to avoid further losses. The transmitted part at $BS1$ is guided over M2 to the delay stage. The first thing that has to be checked is, whether the incoming beam is parallel to the moving direction of the delay stage (High Precision Linear Stage *LIMES 84N* by *OWIS*). The quickest way to ensure this is to use a target paper at the position of mirror M3 on the two extreme settings of the delay stage. M1 and M2 are used to align the beam along the stage with a "beam-walk" to hit the target at the same spot in both extremes. To ensure that the reflected beam is still parallel to the stage, it does not matter how the first mirror on the delay stage M3 reflects the beam to M4. Excepting this, M4 can be used to find the position that brings an output beam that is again parallel to the stage. For this again a target can be used that is placed behind the stage. The following routine would be to set a point on the target, where the stage has the shortest delay length. Afterwards the stage moves to the other extreme position and M4 is used to align the beam back to this point. When the stage is aligned "perfectly", the beam hits the point at every stage position. Note that the initial set point will have a deviating position from the final output. The next step would be to align the main pulse

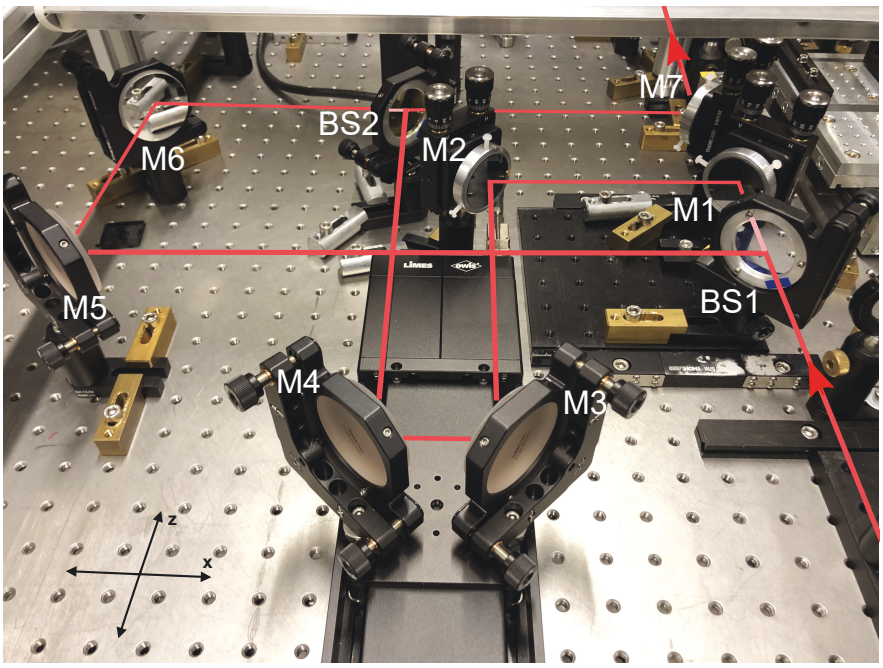

Figure D.1: Pre-pulse module setup with indicated beam path designed in the context of Jonah Book's bachelor thesis [54]. Mirrors are indicated with M and beam splitters with BS.

with beamsplitter BS2 and mirror M7 to the former beam path to the vacuum chamber. Finally, the pre-pulse that is reflected on BS1 can be aligned with M5 and M6 to the same path. If the two pulses are geometrically overlapping can be checked with higher precision in the experimental chamber around 15 m behind the aligned stage doing the focus diagnostic. The quality of the geometrical overlap is checked at different delay stage positions to verify that the two pulses are aligned in the best possible manner. For this, the focal spots of pre- and main pulse are detected by an objective lens in the experimental chamber attenuated by neutral density glasses to the same intensity. Both exhibit a Gaussian width of $w_G \approx 2\,\mu\text{m}$. The quality of the alignment is characterized by the distance of two Gaussian fits overlapping in the detection region. Along the whole mechanical stage of 12 cm length, the two beams have a distance of 0.42 µm to 1.1 µm. Taking two circles of radii $2w_G$ (99.9 % of the pulse energy) separated by these distances, the corresponding area overlaps with a percentage of 89 % in the best case and 73 % in the worst case. Compare these findings in fig. D.2. Note that the distance does not increase linearly with the delay stage position, which indicates that the parallelism of the stage is warranted to the best possible accuracy. The observed deviations along the stage can be explained by mechanical limitations of the linear stage exhibiting yaw and pitch angles up to 100 µrad. The positioning accuracy along the stage is given as 16 µm per 100 mm that corresponds to 107 fs delay between main- and pre- pulse, which is sufficient when inter-pulse delays in the picosecond regime are used. For higher resolution scans the step length should be chosen way smaller than 100 mm, which might decrease this uncertainty. After the two beams are aligned in the described manner, the temporal overlap can be found by a spectral analysis. Overlapping co-linear pulses indicate

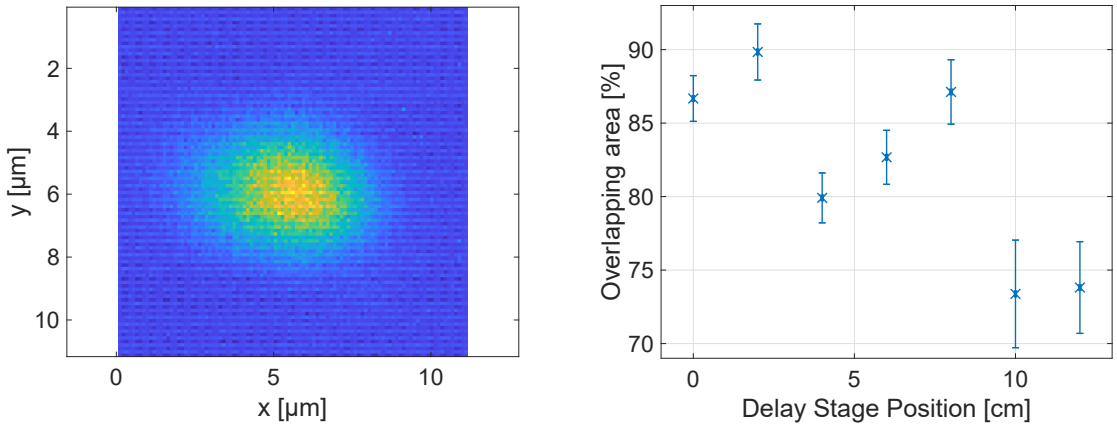

Figure D.2: (left) Simultaneous detection of pre- and main pulse (attenuated to the same intensity) overlapping at the focal spot detected by a CCD camera. (right) Percentage of overlapping area with circles of radius two times the Gaussian width. Indicated are statistical uncertainties of 502 measurements for each delay stage position.

spectral interference that is observable as "fringes" in the detected spectrum as soon as the beams from the two arms overlap. A Fourier analysis can bring the exact delay between the two pulses extracted from the "fringe" distance. With this method, the exact position of inter-pulse delay zero is detected with an accuracy on the order of 5 µm.

Bibliography

[1] Enerdata, *Globales Energie- und Klimastatistik- Jahrbuch 2022*, https://energiestatistik.enerdata.net,Accessed: 2022-09-22.

[2] J. D. Shakun, P. U. Clark, F. He, *et al.*, "Global warming preceded by increasing carbon dioxide concentrations during the last deglaciation," *Nature*, vol. 484, no. 7392, pp. 49–54, 2012. DOI: https://doi.org/10.1038/nature10915.

[3] Statistisches Bundesamt Deutschland, *Bruttostromerzeugung Deutschland*, https://www.destatis.de, Accessed: 2022-09-22.

[4] E. A. Azizov, "Tokamaks: from A. D. Sakharov to the present (the 60-year history of tokamaks)," *Physics-Uspekhi*, vol. 55, no. 2, p. 190, 2012. DOI: https://doi.org/10.3367/ufne.0182.201202j.0202.

[5] L. Spitzer Jr, "The stellarator concept," *The Physics of Fluids*, vol. 1, no. 4, pp. 253–264, 1958. DOI: https://doi.org/10.1063/1.1705883.

[6] J. Ongena, R. Koch, R. Wolf, and H. Zohm, "Magnetic-confinement fusion," *Nature Physics*, vol. 12, no. 5, pp. 398–410, 2016. DOI: https://doi.org/10.1038/NPHYS3745.

[7] A. Dinklage, C. Beidler, P. Helander, *et al.*, "Magnetic configuration effects on the Wendelstein 7-X stellarator," *Nature Physics*, vol. 14, no. 8, pp. 855–860, 2018. DOI: https://doi.org/10.1038/s41567-018-0141-9.

[8] J. D. Lawson, "Some criteria for a power producing thermonuclear reactor," *Proceedings of the physical society. Section B*, vol. 70, no. 1, p. 6, 1957. DOI: https://doi.org/10.1088/0370-1301/70/1/303.

[9] G. De Temmerman, K. Heinola, D. Borodin, *et al.*, "Data on erosion and hydrogen fuel retention in beryllium plasma-facing materials," *Nuclear Materials and Energy*, vol. 27, p. 100 994, 2021. DOI: https://doi.org/10.1016/j.nme.2021.100994.

[10] S. Brezinsek, T. Loarer, V. Philipps, *et al.*, "Fuel retention studies with the ITER-like wall in JET," *Nuclear Fusion*, vol. 53, no. 8, p. 083 023, 2013. DOI: https://doi.org/10.1088/0029-5515/53/8/083023.

[11] O. Ogorodnikova, "Fundamental aspects of deuterium retention in tungsten at high flux plasma exposure," *Journal of Applied Physics*, vol. 118, no. 7, p. 074 902, 2015. DOI: https://doi.org/10.1063/1.4928407.

[12] A. Huber, B. Schweer, V. Philipps, *et al.*, "Development of laser-based diagnostics for surface characterisation of wall components in fusion devices," *Fusion engineering and design*, vol. 86, no. 6-8, pp. 1336–1340, 2011. DOI: https://doi.org/10.1016/j.fusengdes.2011.01.090.

[13] G. Dacey, "Optical masers in science and technology: Advances in the control of light waves give promise of important applications in science and technology.," *Science*, vol. 135, no. 3498, pp. 71–74, 1962. DOI: https://doi.org/10.1126/science.135.3498.71.

[14] M. McCanta, P. Dobosh, M. Dyar, and H. Newsom, "Testing the veracity of LIBS analyses on mars using the LIBSSIM program," *Planetary and Space Science*, vol. 81, pp. 48–54, 2013. DOI: https://doi.org/10.1016/j.pss.2013.03.004.

[15] R. Gaudiuso, E. Ewusi-Annan, N. Melikechi, *et al.*, "Using libs to diagnose melanoma in biomedical fluids deposited on solid substrates: Limits of direct spectral analysis and capability of machine learning," *Spectrochimica Acta Part B: Atomic Spectroscopy*, vol. 146, pp. 106–114, 2018. DOI: https://doi.org/10.1016/j.sab.2018.05.010.

[16] V. C. Costa, J. P. Castro, D. F. Andrade, *et al.*, "Laser-induced breakdown spectroscopy (LIBS) applications in the chemical analysis of waste electrical and electronic equipment (WEEE)," *TrAC Trends in Analytical Chemistry*, vol. 108, pp. 65–73, 2018. DOI: https://doi.org/10.1016/j.trac.2018.08.003.

[17] K. Touchet, F. Chartier, J. Hermann, and J.-B. Sirven, "Laser-induced breakdown self-reversal isotopic spectrometry for isotopic analysis of lithium," *Spectrochimica Acta Part B: Atomic Spectroscopy*, vol. 168, p. 105 868, 2020. DOI: https://doi.org/10.1016/j.sab.2020.105868.

[18] D. Strickland and G. Mourou, "Compression of amplified chirped optical pulses," *Optics communications*, vol. 55, no. 6, pp. 447–449, 1985. DOI: https://doi.org/10.1016/0030-4018(85)90151-8.

[19] V. Zorba, J. Syzdek, X. Mao, R. E. Russo, and R. Kostecki, "Ultrafast laser induced breakdown spectroscopy of electrode/electrolyte interfaces," *Applied Physics Letters*, vol. 100, no. 23, p. 234 101, 2012. DOI: https://doi.org/10.1063/1.4724203.

[20] Z. Hu, N. Gierse, C. Li, *et al.*, "Development of laser-based technology for the routine first wall diagnostic on the tokamak east: Libs and lias," *Physica Scripta*, vol. 2017, no. T170, p. 014 046, 2017. DOI: https://doi.org/10.1088/1402-4896/aa8650.

[21] J. Oelmann, Z. Hu, C. Li, *et al.*, "Analyses of deuterium retention in tungsten and graphite first wall materials by laser-induced ablation spectroscopy on east," *Fusion Engineering and Design*, vol. 162, p. 112 108, 2021. DOI: https://doi.org/10.1016/j.fusengdes.2020.112108.

[22] B. N. Chichkov, C. Momma, S. Nolte, F. Von Alvensleben, and A. Tünnermann, "Femtosecond, picosecond and nanosecond laser ablation of solids," *Applied Physics A*, vol. 63, no. 2, pp. 109–115, 1996.

[23] S. Kirkwood, Y. Tsui, R. Fedosejevs, A. Brantov, and V. Y. Bychenkov, "Experimental and theoretical study of absorption of femtosecond laser pulses in interaction with solid copper targets," *Physical Review B*, vol. 79, no. 14, p. 144 120, 2009. DOI: https://doi.org/10.1103/PhysRevB.79.144120.

[24] S. Rand, "Inverse bremsstrahlung with high-intensity radiation fields," *Physical Review*, vol. 136, no. 1B, B231, 1964. DOI: https://doi.org/10.1103/PhysRev.136.B231.

[25] D. Semkat, R. Redmer, and T. Bornath, "Collisional absorption in aluminum," *Physical Review E*, vol. 73, no. 6, p. 066 406, 2006. DOI: https://doi.org/10.1103/PhysRevE.73.066406.

[26] Y.-Q. Cui, W.-M. Wang, Z.-M. Sheng, Y.-T. Li, and J. Zhang, "Laser absorption and hot electron temperature scalings in laser–plasma interactions," *Plasma Physics and Controlled Fusion*, vol. 55, no. 8, p. 085 008, 2013. DOI: https://doi.org/10.1088/0741-3335/55/8/085008.

[27] P. Gibbon and E. Förster, "Short-pulse laser-plasma interactions," *Plasma physics and controlled fusion*, vol. 38, no. 6, p. 769, 1996. DOI: https://doi.org/10.1088/0741-3335/38/6/001.

[28] M. Cerchez, R. Jung, J. Osterholz, *et al.*, "Absorption of ultrashort laser pulses in strongly overdense targets," *Physical review letters*, vol. 100, no. 24, p. 245 001, 2008. DOI: https://doi.org/10.1103/PhysRevLett.100.245001.

[29] F. Brunel, "Not-so-resonant, resonant absorption," *Physical review letters*, vol. 59, no. 1, p. 52, 1987. DOI: https://doi.org/10.1103/PhysRevLett.59.52.

[30] X. Zhao and Y. C. Shin, "Femtosecond laser ablation of aluminum in vacuum and air at high laser intensity," *Applied Surface Science*, vol. 283, pp. 94–99, 2013. DOI: https://doi.org/10.1016/j.apsusc.2013.06.037.

[31] J. Byskov-Nielsen, J.-M. Savolainen, M. S. Christensen, and P. Balling, "Ultra-short pulse laser ablation of metals: Threshold fluence, incubation coefficient and ablation rates," *Applied Physics A*, vol. 101, no. 1, pp. 97–101, 2010. DOI: https://doi.org/10.1007/s00339-010-5766-1.

[32] S. Amoruso, R. Bruzzese, X. Wang, N. Nedialkov, and P. Atanasov, "Femtosecond laser ablation of nickel in vacuum," *Journal of Physics D: Applied Physics*, vol. 40, no. 2, p. 331, 2007. DOI: https://doi.org/10.1088/0022-3727/40/2/008.

[33] H. Dachraoui, W. Husinsky, and G. Betz, "Ultra-short laser ablation of metals and semiconductors: Evidence of ultra-fast coulomb explosion," *Applied Physics A*, vol. 83, no. 2, pp. 333–336, 2006. DOI: https://doi.org/10.1103/PhysRevB.62.13167.

[34] R. Stoian, D. Ashkenasi, A. Rosenfeld, and E. Campbell, "Coulomb explosion in ultrashort pulsed laser ablation of Al 2 O 3," *Physical review B*, vol. 62, no. 19, p. 13 167, 2000. DOI: https://doi.org/10.1103/PhysRevB.62.13167.

[35] T. A. Labutin, V. N. Lednev, A. A. Ilyin, and A. M. Popov, "Femtosecond laser-induced breakdown spectroscopy," *Journal of Analytical Atomic Spectrometry*, vol. 31, no. 1, pp. 90–118, 2016. DOI: https://doi.org/10.1039/C5JA00301F.

[36] R. Tamaki, T. Kasai, G. Asai, *et al.*, "Pulse-to-pulse detection of terahertz radiation emitted from the femtosecond laser ablation process," *Optics Express*, vol. 30, no. 13, pp. 23 622–23 630, 2022. DOI: https://doi.org/10.1364/OE.459588.

[37] S. I. Ashitkov, M. B. Agranat, P. S. Kondratenko, *et al.*, "Ultrafast laser-induced phase transitions in tellurium," *Journal of Experimental and Theoretical Physics Letters*, vol. 76, no. 7, pp. 461–464, 2002. DOI: https://doi.org/10.1134/1.1528702.

[38] S. Sundaram and E. Mazur, "Inducing and probing non-thermal transitions in semiconductors using femtosecond laser pulses," *Nature materials*, vol. 1, no. 4, pp. 217–224, 2002. DOI: https://doi.org/10.1038/nmat767.

[39] X. Ye, Z. He, F. Gao, and B. Pan, "Non-thermal melting of tungsten under intense electronic excitations," *Acta Materialia*, vol. 216, p. 117 158, 2021. DOI: https://doi.org/10.1016/j.actamat.2021.117158.

[40] L. V. Zhigilei, Z. Lin, and D. S. Ivanov, "Atomistic modeling of short pulse laser ablation of metals: Connections between melting, spallation, and phase explosion," *The Journal of Physical Chemistry C*, vol. 113, no. 27, pp. 11 892–11 906, 2009. DOI: https://doi.org/10.1021/jp902294m.

[41] F. Vidal, T. Johnston, S. Laville, *et al.*, "Critical-point phase separation in laser ablation of conductors," *Physical review letters*, vol. 86, no. 12, p. 2573, 2001. DOI: https://doi.org/10.1103/PhysRevLett.86.2573.

[42] B. Wu and Y. C. Shin, "A simple model for high fluence ultra-short pulsed laser metal ablation," *Applied surface science*, vol. 253, no. 8, pp. 4079–4084, 2007. DOI: https://doi.org/10.1016/j.apsusc.2006.09.007.

[43] P. Lorazo, L. J. Lewis, and M. Meunier, "Short-pulse laser ablation of solids: From phase explosion to fragmentation," *Physical review letters*, vol. 91, no. 22, p. 225 502, 2003. DOI: https://doi.org/10.1103/PhysRevLett.91.225502.

[44] P. Lorazo, L. J. Lewis, and M. Meunier, "Thermodynamic pathways to melting, ablation, and solidification in absorbing solids under pulsed laser irradiation," *Physical Review B*, vol. 73, no. 13, p. 134 108, 2006. DOI: https://doi.org/10.1103/PhysRevB.73.134108.

[45] D. Mihalas, "Stellar atmospheres," *San Francisco: WH Freeman*, 1978.

[46] G. Cristoforetti, A. De Giacomo, M. Dell'Aglio, *et al.*, "Local thermodynamic equilibrium in laser-induced breakdown spectroscopy: Beyond the mcwhirter criterion," *Spectrochimica Acta Part B: Atomic Spectroscopy*, vol. 65, no. 1, pp. 86–95, 2010. DOI: https://doi.org/10.1016/j.sab.2009.11.005.

[47] T. Fujimoto and R. McWhirter, "Validity criteria for local thermodynamic equilibrium in plasma spectroscopy," *Physical Review A*, vol. 42, no. 11, p. 6588, 1990. DOI: https://doi.org/10.1103/PhysRevA.42.6588.

[48] D. Spence, J. Evans, W. Sleat, and W. Sibbett, "Regeneratively initiated self-mode-locked Ti: Sapphire laser," *Optics letters*, vol. 16, no. 22, pp. 1762–1764, 1991. DOI: https://doi.org/10.1364/OL.16.001762.

[49] C. Iaconis and I. A. Walmsley, "Self-referencing spectral interferometry for measuring ultrashort optical pulses," *IEEE Journal of quantum electronics*, vol. 35, no. 4, pp. 501–509, 1999. DOI: https://doi.org/10.1109/3.753654.

[50] W. Kornelis, J. Biegert, J. Tisch, *et al.*, "Single-shot kilohertz characterization of ultrashort pulses by spectral phase interferometry for direct electric-field reconstruction," *Optics letters*, vol. 28, no. 4, pp. 281–283, 2003. DOI: https://doi.org/10.1364/OL.28.000281.

[51] J. Wegner, *Ablation von Metallen mittels hochintensiver, few-cycle Laserpulse*. 2020, https://docserv.uni-duesseldorf.de/servlets/DocumentServlet?id=52441.

[52] R. A. Ganeev, "Generation of high-order harmonics of high-power lasers in plasmas produced under irradiation of solid target surfaces by a prepulse," *Physics-Uspekhi*, vol. 52, no. 1, p. 55, 2009. DOI: https://doi.org/10.3367/UFNe.0179.200901c.0065.

[53] W. Lu, M. Nicoul, U. Shymanovich, *et al.*, "Optimized K α x-ray flashes from femtosecond-laser-irradiated foils," *Physical Review E*, vol. 80, no. 2, p. 026 404, 2009. DOI: https://doi.org/10.1103/PhysRevE.80.026404.

[54] J. Book, "Entwicklung und charakterisierung einer vorpuls-einheit für einen ultrakurzpulslaser," B.s. Thesis, 2021.

[55] J. Mildner, C. Sarpe, N. Götte, M. Wollenhaupt, and T. Baumert, "Emission signal enhancement of laser ablation of metals (aluminum and titanium) by time delayed femtosecond double pulses from femtoseconds to nanoseconds," *Applied Surface Science*, vol. 302, pp. 291–298, 2014. DOI: https://doi.org/10.1016/j.apsusc.2013.09.137.

[56] J. W. Strutt *et al.*, "Investigations in optics, with special reference to the spectroscope," *Philosophical magazine*, vol. 8, no. 49, pp. 261–274, 1879, https://www.tandfonline.com/doi/pdf/10.1080/14786448008626795.

[57] A. B. Shafer, L. R. Megill, and L. Droppleman, "Optimization of the czerny–turner spectrometer," *JOSA*, vol. 54, no. 7, pp. 879–887, 1964. DOI: https://doi.org/10.1364/JOSA.54.000879.

[58] P. Hoess and K. Fleder, "Subnanosecond optical gating and irising properties of different types of microchannel plate image intensifiers (mcpii)," in *Optical Diagnostics for Fluids/Heat/Combustion and Photomechanics for Solids*, SPIE, vol. 3783, 1999, pp. 194–200. DOI: https://doi.org/10.1117/12.365739.

[59] M. A. Gigosos, M. A. Gonzalez, and V. Cardenoso, "Computer simulated balmer-alpha,-beta and-gamma stark line profiles for non-equilibrium plasmas diagnostics," *Spectrochimica Acta Part B: Atomic Spectroscopy*, vol. 58, no. 8, pp. 1489–1504, 2003. DOI: https://doi.org/10.1016/S0584-8547(03)00097-1.

[60] T. Ida, M. Ando, and H. Toraya, "Extended pseudo-voigt function for approximating the voigt profile," *Journal of Applied Crystallography*, vol. 33, no. 6, pp. 1311–1316, 2000. DOI: https://doi.org/10.1107/S0021889800010219.

[61] V. Dwivedi, M. Veis, A. M. Roldán, *et al.*, "CF-LIBS study of pure Ta, and WTa+ D coating as fusion-relevant materials: a step towards future in situ compositional quantification at atmospheric pressure," *The European Physical Journal Plus*, vol. 136, no. 11, p. 1177, 2021. DOI: https://doi.org/10.1140/epjp/s13360-021-02179-0.

[62] E. Mal, R. Junjuri, M. K. Gundawar, and A. Khare, "Temporal characterization of laser-induced plasma of tungsten in air," *Laser and Particle Beams*, vol. 38, no. 1, pp. 14–24, 2020. DOI: https://doi.org/10.1017/S0263034619000788.

[63] A. Taleb, V. Motto-Ros, M. J. Carru, *et al.*, "Measurement error due to self-absorption in calibration-free laser-induced breakdown spectroscopy," *Analytica Chimica Acta*, vol. 1185, p. 339 070, 2021. DOI: https://doi.org/10.1016/j.aca.2021.339070.

[64] J. Roth, E. Tsitrone, T. Loarer, *et al.*, "Tritium inventory in ITER plasma-facing materials and tritium removal procedures," *Plasma Physics and Controlled Fusion*, vol. 50, no. 10, p. 103 001, 2008. DOI: https://doi.org/10.1088/0741-3335/50/10/103001.

[65] A. Kreter, D. Nishijima, R. Doerner, *et al.*, "Influence of plasma impurities on the fuel retention in tungsten," *Nuclear fusion*, vol. 59, no. 8, p. 086 029, 2019. DOI: https://doi.org/10.1088/1741-4326/ab235d.

[66] N. P. Bobyr, V. S. Efimov, B. I. Khripunov, D. A. Kozlov, and A. A. Mednikov, "Deuterium retention in w-ta alloys after low-temperature plasma irradiation and gas exposure," *Physica Scripta*, vol. 96, no. 12, p. 125 633, 2021. DOI: https://doi.org/10.1088/1402-4896/ac3ea4.

[67] C. Sang, X. Bonnin, M. Warrier, *et al.*, "Modelling of hydrogen isotope inventory in mixed materials including porous deposited layers in fusion devices," *Nuclear Fusion*, vol. 52, no. 4, p. 043 003, 2012. DOI: https://doi.org/10.1088/0029-5515/52/4/043003.

[68] G. Amsel and W. Lanford, "Nuclear reaction techniques in materials analysis," *Annu. Rev. Nucl. Part. Sci.;(United States)*, vol. 34, 1984. DOI: https://doi.org/10.1146/annurev.ns.34.120184.002251.

[69] M. Mayer, E. Gauthier, K. Sugiyama, and U. Von Toussaint, "Quantitative depth profiling of deuterium up to very large depths," *Nuclear Instruments and Methods in Physics Research Section B: Beam Interactions with Materials and Atoms*, vol. 267, no. 3, pp. 506–512, 2009. DOI: https://doi.org/10.1016/j.nimb.2008.11.033.

[70] T. Hirai, M. Rubel, V. Philipps, *et al.*, "Testing of tungsten and tantalum limiters at the TEXTOR tokamak: Material performance and deuterium retention," *Physica Scripta*, vol. 2003, no. T103, p. 59, 2003, https://iopscience.iop.org/article/10.1238/Physica.Topical.103a00059/pdf.

[71] J. Oelmann, *Quantitative Untersuchung des Laserablationsprozesses mittels Kombination von optischer Spektroskopie und Massenspektrometrie*. Plasmaphysik, 2020, http://hdl.handle.net/2128/24182.

[72] J. Oelmann, C. Li, S. Brezinsek, *et al.*, "Depth resolved analysis of hydrogen in W7-X graphite components using laser-induced ablation-quadrupole mass spectrometry (LIA-QMS)," *Nuclear materials and energy*, vol. 18, pp. 153–158, 2019. DOI: https://doi.org/10.1016/j.nme.2018.12.019.

[73] S. Mittelmann, J. Oelmann, S. Brezinsek, D. Wu, H. Ding, and G. Pretzler, "Laser-induced ablation of tantalum in a wide range of pulse durations," *Applied Physics A*, vol. 126, no. 9, pp. 1–7, 2020. DOI: https://doi.org/10.1007/s00339-020-03838-2.

[74] S. Mittelmann, J. Oelmann, S. Brezinsek, *et al.*, "Comparison of laser-induced ablation thresholds of tantalum in a wide range of pulse durations," *47th EPS Conference on Plasma Physics*, 2021, http://ocs.ciemat.es/EPS2021PAP/pdf/P2.3006.pdf.

[75] D. Zhao, N. Gierse, J. Oelmann, *et al.*, "Investigation of laser ablation features of molybdenum bulk for picosecond laser-based techniques in fusion devices," *Fusion Engineering and Design*, vol. 151, p. 111 379, 2020. DOI: https://doi.org/10.1016/j.fusengdes.2019.111379.

[76] W. S. Werner, K. Glantschnig, and C. Ambrosch-Draxl, "Optical constants and inelastic electron-scattering data for 17 elemental metals," *Journal of Physical and Chemical Reference Data*, vol. 38, no. 4, pp. 1013–1092, 2009. DOI: https://doi.org/10.1063/1.3243762.

[77] S. Tani and Y. Kobayashi, "Pulse-by-pulse depth profile measurement of femtosecond laser ablation on copper," *Applied Physics A*, vol. 124, no. 3, pp. 1–5, 2018. DOI: https://doi.org/10.1007/s00339-018-1694-2.

[78] A. H. Hamad, *Effects of different laser pulse regimes (nanosecond, picosecond and femtosecond) on the ablation of materials for production of nanoparticles in liquid solution*. IntechOpen London, UK, 2016.

[79] T. Genieys, M. Sentis, and O. Utéza, "Investigation of ultrashort laser excitation of aluminum and tungsten by reflectivity measurements," *Applied Physics A*, vol. 126, no. 4, pp. 1–14, 2020. DOI: https://doi.org/10.1007/s00339-020-3440-9.

[80] E. G. Gamaly, A. V. Rode, B. Luther-Davies, and V. T. Tikhonchuk, "Ablation of solids by femtosecond lasers: Ablation mechanism and ablation thresholds for metals and dielectrics," *Physics of plasmas*, vol. 9, no. 3, pp. 949–957, 2002. DOI: https://doi.org/10.1063/1.1447555.

[81] E. V. Struleva, P. S. Komarov, and S. I. Ashitkov, "Characteristics of tantalum ablation under the impact of a femtosecond laser," *High Temperature*, vol. 56, no. 5, pp. 648–651, 2018. DOI: https://doi.org/10.1134/S0018151X18050255.

[82] L. Torrisi, F. Caridi, A. Picciotto, D. Margarone, and A. Borrielli, "Particle emission from tantalum plasma produced by 532 nm laser pulse ablation," *Journal of applied physics*, vol. 100, no. 9, p. 093 306, 2006. DOI: https://doi.org/10.1063/1.23584000.

[83] M. Leitner, W. Schröer, and G. Pottlacher, "Density of liquid tantalum and estimation of critical point data," *International Journal of Thermophysics*, vol. 39, no. 11, pp. 1–14, 2018. DOI: https://doi.org/10.1007/s10765-018-2439-3.

[84] S. Harilal, N. Farid, A. Hassanein, and V. Kozhevin, "Dynamics of femtosecond laser produced tungsten nanoparticle plumes," *Journal of Applied Physics*, vol. 114, no. 20, p. 203 302, 2013. DOI: https://doi.org/10.1063/1.4833564.

[85] P. Lickschat, D. Metzner, and S. Weißmantel, "Fundamental investigations of ultrashort pulsed laser ablation on stainless steel and cemented tungsten carbide," *The International Journal of Advanced Manufacturing Technology*, vol. 109, no. 3, pp. 1167–1175, 2020. DOI: https://doi.org/10.1007/s00170-020-05502-8.

[86] K. Anoop, S. Harilal, R. Philip, R. Bruzzese, and S. Amoruso, "Laser fluence dependence on emission dynamics of ultrafast laser induced copper plasma," *Journal of Applied Physics*, vol. 120, no. 18, p. 185 901, 2016. DOI: https://doi.org/10.1063/1.4967313.

[87] A. Kramida, Yu. Ralchenko, J. Reader, and and NIST ASD Team, NIST Atomic Spectra Database (ver. 5.9), [Online]. Available: https://physics.nist.gov/asd [2022, March 14]. National Institute of Standards and Technology, Gaithersburg, MD. 2021. DOI: https://dx.doi.org/10.18434/T4W30F.

[88] S. Noël and J. Hermann, "Reducing nanoparticles in metal ablation plumes produced by two delayed short laser pulses," *Applied Physics Letters*, vol. 94, no. 5, p. 053 120, 2009. DOI: https://doi.org/10.1063/1.3079404.

[89] A. Semerok and C. Dutouquet, "Ultrashort double pulse laser ablation of metals," *Thin solid films*, vol. 453, pp. 501–505, 2004. DOI: https://doi.org/10.1016/j.tsf.2003.11.115.

[90] R. Teghil, A. Santagata, A. De Bonis, *et al.*, "Applications of ultra-short pulsed laser ablation: Thin films deposition and fs/ns dual-pulse laser-induced breakdown spectroscopy," *Physica Scripta*, vol. 78, no. 5, p. 058 113, 2008. DOI: https://doi.org/10.1088/0031-8949/78/05/058113.

[91] M. Stumpf, "Pump-probe-experimente zur diagnostik von ultrakurzpuls-laser-plasmen," M.s. Thesis, 2017.

[92] E. Kautz, A. Devaraj, D. Senor, and S. Harilal, "Hydrogen isotopic analysis of nuclear reactor materials using ultrafast laser-induced breakdown spectroscopy," *Optics Express*, vol. 29, no. 4, pp. 4936–4946, 2021. DOI: https://doi.org/10.1364/OE.412351.

[93] S. Mittelmann, K. Touchet, X. Mao, *et al.*, "Hydrogen Isotope Analysis in W-Tiles using fs-LIBS," *Scientific Reports*, vol. 13, no. 2285, 2023. DOI: https://doi.org/10.1038/s41598-023-29138-2.

[94] J. Hermann, D. Grojo, E. Axente, C. Gerhard, M. Burger, and V. Craciun, "Ideal radiation source for plasma spectroscopy generated by laser ablation," *Physical Review E*, vol. 96, no. 5, p. 053 210, 2017. DOI: https://doi.org/10.1103/PhysRevE.96.053210.

[95] S. Zhang, X. Wang, M. He, *et al.*, "Laser-induced plasma temperature," *Spectrochimica Acta Part B: Atomic Spectroscopy*, vol. 97, pp. 13–33, 2014. DOI: https://doi.org/10.1016/j.sab.2014.04.009.

[96] C. Aragón and J. A. Aguilera, "Characterization of laser induced plasmas by optical emission spectroscopy: A review of experiments and methods," *Spectrochimica Acta Part B: Atomic Spectroscopy*, vol. 63, no. 9, pp. 893–916, 2008. DOI: https://doi.org/10.1016/j.sab.2008.05.010.

[97] X. Jiang, G. Sergienko, A. Kreter, S. Brezinsek, and C. Linsmeier, "In situ study of short-term retention of deuterium in tungsten during and after plasma exposure in psi-2," *Nuclear Fusion*, vol. 61, no. 9, p. 096 006, 2021. DOI: https://doi.org/10.1088/1741-4326/ac112e.

[98] V. K. Alimov, W. Shu, J. Roth, *et al.*, "Surface morphology and deuterium retention in tungsten exposed to low-energy, high flux pure and helium-seeded deuterium plasmas," *Physica Scripta*, vol. 2009, no. T138, p. 014 048, 2009. DOI: https://doi.org/10.1088/0031-8949/2009/T138/014048.

[99] J. Oelmann, E. Wüst, G. Sergienko, and S. Brezinsek, "Double pulse laser-induced breakdown spectroscopy for the analysis of plasma-facing components," *Physica Scripta*, vol. 96, no. 12, p. 124 064, 2021. DOI: https://doi.org/10.1088/1402-4896/ac379c.

[100] M. Pardede, I. Karnadi, R. Hedwig, *et al.*, "High sensitivity hydrogen analysis in zircaloy-4 using helium-assisted excitation laser-induced breakdown spectroscopy," *Scientific Reports*, vol. 11, no. 1, pp. 1–10, 2021. DOI: https://doi.org/10.1038/s41598-021-01601-y.

[101] E. J. Kautz, E. C. Rönnebro, A. Devaraj, D. J. Senor, and S. S. Harilal, "Detection of hydrogen isotopes in zircaloy-4 via femtosecond LIBS," *Journal of Analytical Atomic Spectrometry*, vol. 36, no. 6, pp. 1217–1227, 2021. DOI: https://doi.org/10.1039/D1JA00034A.

[102] N. Giannakaris, A. Haider, C. M. Ahamer, S. Grünberger, S. Trautner, and J. D. Pedarnig, "Femtosecond single-pulse and orthogonal double-pulse laser-induced breakdown spectroscopy (LIBS): Femtogram mass detection and chemical imaging with micrometer spatial resolution," *Applied Spectroscopy*, p. 00 037 028 211 042 398, 2021. DOI: https://doi.org/10.1177/00037028211042398.

[103] G. Yang, Q. Lin, Y. Ding, D. Tian, and Y. Duan, "Laser induced breakdown spectroscopy based on single beam splitting and geometric configuration for effective signal enhancement," *Scientific reports*, vol. 5, no. 1, pp. 1–11, 2015. DOI: https://doi.org/10.1038/srep07625.

[104] Z. Lin, L. V. Zhigilei, and V. Celli, "Electron-phonon coupling and electron heat capacity of metals under conditions of strong electron-phonon nonequilibrium," *Physical Review B*, vol. 77, no. 7, p. 075 133, 2008. DOI: https://doi.org/10.1103/PhysRevB.77.075133.

[105] B. Rethfeld, D. S. Ivanov, M. E. Garcia, and S. I. Anisimov, "Modelling ultrafast laser ablation," *Journal of Physics D: Applied Physics*, vol. 50, no. 19, p. 193 001, 2017. DOI: https://doi.org/10.1088/1361-6463/50/19/193001.

[106] W. McMillan, "Transition temperature of strong-coupled superconductors," *Physical Review*, vol. 167, no. 2, p. 331, 1968. DOI: https://doi.org/10.1103/PhysRev.167.331.

[107] A. D. Rakić, A. B. Djurišić, J. M. Elazar, and M. L. Majewski, "Optical properties of metallic films for vertical-cavity optoelectronic devices," *Applied optics*, vol. 37, no. 22, pp. 5271–5283, 1998. DOI: https://doi.org/10.1364/AO.37.005271.

[108] S. Brorson, A. Kazeroonian, J. Moodera, *et al.*, "Femtosecond room-temperature measurement of the electron-phonon coupling constant γ in metallic superconductors," *Physical Review Letters*, vol. 64, no. 18, p. 2172, 1990. DOI: https://doi.org/10.1103/PhysRevLett.64.2172.

[109] A. Al-Lehaibi, J. C. Swihart, W. H. Butler, and F. J. Pinski, "Electron-phonon interaction effects in tantalum," *Physical Review B*, vol. 36, no. 8, p. 4103, 1987. DOI: https://doi.org/10.1103/PhysRevB.36.4103.

[110] M. Demin, O. Koroleva, A. Shapranov, and A. Aleksashkina, "Atomistic modeling of the critical region of copper using a liquid-vapor coexistence curve," *Mathematical Montisnigri*, vol. 46, pp. 61–71, 2019. DOI: https://doi.org/10.20948/mathmontis-2019-46-6.

[111] G. Faussurier, C. Blancard, and P. L. Silvestrelli, "Evaluation of aluminum critical point using an ab initio variational approach," *Physical Review B*, vol. 79, no. 13, p. 134 202, 2009. DOI: https://doi.org/10.1103/PhysRevB.79.134202.

[112] A. Likalter, "Critical points of metals of three main groups and selected transition metals," *Physica A: Statistical Mechanics and its Applications*, vol. 311, no. 1-2, pp. 137–149, 2002. DOI: https://doi.org/10.1016/S0378-4371(02)00840-3.

[113] H. Hess, "Critical data of metals-estimations for tungsten," *Physics and Chemistry of Liquids*, vol. 30, no. 4, pp. 251–256, 1995. DOI: https://doi.org/10.1080/00319109508030672.

Publications

Peer-reviewed articles

S. Mittelmann, J. Oelmann, S. Brezinsek, D. Wu, H. Ding, G. Pretzler. **Laser-induced ablation of tantalum in a wide range of pulse durations**. Appl. Phys. A, 126(9), 1-7 (2020).

S. Mittelmann, K. Touchet, X. Mao, M. Park, S. Brezinsek, G. Pretzler, V. Zorba. **Hydrogen Isotope Analysis in W-Tiles using fs-LIBS**. Sci. Rep. 13, 2285 (2023)

Conference Contributions

S. Mittelmann, S. Brezinsek, V. Zorba, G. Pretzler, **Towards high depth resolution H-isotope diagnostic in Tantalum and Tungsten tiles**, LIBS 2022 in Bari, Italy (talk)

S. Mittelmann, J. Oelmann, D. Wu, S. G. Sergienko, S. Brezinsek, H. Ding, G. Pretzler, **Comparison of Laser-Induced Breakdown Spectroscopy (LIBS) results on deuterium loaded high Z materials from lasers of different pulse duration**, DPG Frühjahrstagung SMuK 2021, virtual, (poster)

S. Mittelmann, J. Oelmann, S. Brezinsek, G. Sergienko, D. Wu, H. Ding, G. Pretzler, **Comparison of Laser-Induced Ablation Thresholds of Tantalum in a Wide Range of Pulse Durations**, EPS Conference on Plasma Physics 2021, virtual, (poster, conference paper)

S. Mittelmann, J. Wegner, J. Riedlinger, G. Pretzler, **Experimental and Numerical Observation of the Interaction of fs-Laser Pulses with Solids in a Wide Range of Intensities**, ASLIBS 2019 in Jeju, South Korea (poster)

Adopted content from own publications

Laser-induced ablation of tantalum in a wide range of pulse durations

The content in chapter 4 is mainly taken, slightly adapted, and complemented from the joint publication ref. [73].

Contribution to the publication:

- Self-reliant writing as corresponding author of the first submitted draft
- Realization of the experimental setup at home institute
- Participation and supervision of the contributing experiments at Dalian University of Technology and Forschungszentrum Jülich
- Crater analysis with confocal microscope and data processing

Comparison of Laser-Induced Ablation Thresholds of Tantalum in a Wide Range of Pulse Durations

Parts of the content in section 4.4 and 5.1 are taken from the conference contribution paper ref. [74].

Contribution to the publication:

- Self-reliant writing as corresponding author of the first submitted draft
- Realization of the experimental setup at home institute in collaboration with J. Oelmann by an idea of G. Sergienko
- Development of TTM simulation

Hydrogen Isotope Analysis in W-Tiles using fs-LIBS

Most of the content in section 6.2 is taken from the joint publication ref. [93] to be submitted with a few additions.

Contribution to the publication:

- Self-reliant writing as corresponding author of the first draft
- Realization of the experimental setup at Lawrence Berkeley National Laboratory
- Data processing and interpretation in collusion with the other authors
- Crater analysis with white light interferometer and data processing

List of Abbreviations and Acronyms

LASER	**L**ight **A**mplification by **S**timulated **E**mission of **R**adiation
LIBS	**L**aser **I**nduced **B**reakdown **S**pectroscopy
CF-LIBS	**C**alibration **F**ree **LIBS**
PHASER	**P**hase-stabilized **H**eine l**ASER**
AOM	**A**cousto-**O**ptical **M**odulator
AOFS	**A**cousto-**O**ptical **F**requency **S**hifter
BS	**B**eam-**S**plitter
CPA	**C**hirped **P**ulse **A**mplification
CCD	**C**harge-**C**ouple **D**evice
iCCD	**i**ntensified **CCD**
CEP	**C**arrier **E**nvelope **P**hase
CMOS	**C**omplementray **M**etal-**O**xide-**S**emiconductor
CPPS	**C**ritical-**P**oint **P**hase **S**eparation
CW	**C**ontinous-**W**ave
DC	**D**irect **C**urrent
DUT	**D**alian **U**niversity of **T**echnology
DFG	**D**eutsche **F**orschungs**g**emeinschaft
DPSS	**D**iode **P**umped **S**olid **S**tate
EAST	**E**xperimental **A**dvanced **S**uperconducting **T**okamak
ELM	**E**dge-**L**ocalized **M**ode
EPS	**E**uropean **P**lasma **S**ociety
FTCS	**F**orward **T**ime **C**entered **S**pace
FWHM	**F**ull **W**idth at **H**alf **M**aximum
FWHA	**F**ull **W**idth at **H**alf **A**rea
GDD	**G**roup **D**elay **D**ispersion
HAZ	**H**eat **A**ffected **Z**one
HCL	**H**ollow **C**athode **L**amp
HeRA	**He**ine **R**esearch **A**cademy
HHU	**H**einrich-**H**eine-**U**niversität
HWHM	**H**alf **W**idth at **H**alf **M**aximum

IEK-4	**I**nstitut für **E**nergie- und **K**limaforschung **4**, Forschungszentrum Jülich
ILPP	**I**nstitut für **L**aser- und **P**lasma**p**hysik
IR	**I**nfra**r**ed
ITER	**I**nternational **T**hermonuclear **E**xperimental **R**eactor
JET	**J**oint **E**uropean **T**orus
LIA-QMS	**L**aser **I**nduced **A**blation - **Q**uadrupol **M**ass **S**pectroscopy
LBNL	**L**awrence **B**erkeley **N**ational **L**aboratory
LIP	**L**aser **I**nduced **P**lasma
LTE	**L**ocal **T**hermodynamic **E**quilibrium
MCP	**M**icro-**C**hannel **P**late
MSL	**M**ars **S**cience **L**aboratory
NIST	**N**ational **I**nstitute of **S**tandards and **T**echnology
Nd:YAG	**N**eo**d**ymium-doped **Y**tterbium **A**luminum **G**ernet crystal
NRA	**N**uclear **R**eaction **A**nalysis
OES	**O**ptical **E**mission **S**pectroscopy
PFC	**P**lasma **F**acing **C**omponents
PSF	**P**oint **S**pread **F**unction
PWI	**P**lasma-**W**all **I**nteraction
RF	**R**adio-**F**equency
SESAM	**SE**miconductor **S**turable **A**bsorber **M**irror
SPIDER	**S**pectral **P**hase **I**nterferometry for **D**irect **E**lectric-field **R**econstruction
TE	**T**hermodynamic **E**quilibrium
TDS	**T**hermal **D**esorption **S**pectroscopy
TTM	**T**wo-**T**emperature **M**odel
Ti:Sa	**Ti**tanium **Sa**pphier doped crystal
UV	**U**ltra-**V**iolet
VIS	**VIS**ible
W-7X	**W**endelstein **7-X**

List of Figures

List of Tables

Acknowledgements

In erster Linie möchte ich mich bei meinem Doktorvater Prof. Georg Pretzler bedanken. Vielen Dank, dass Sie mir den Weg für meine Promotion bereitet haben, indem Sie mir die Möglichkeit gaben an einem spannendem, internationalen Projekt gefördert durch die Deutsche Forschungsgemeinschaft mitzuarbeiten. Genauso bin ich Ihnen Dankbar für Ihre Unterstützung bei meiner Bewerbung für das Fulbright Stipendium, das mich wissenschaftlich und persönlich geformt hat. Darüber hinaus habe ich großen Respekt davor, wie viel Wert Sie auf eine umfassende und tiefegehende Ausbildung von Wissenschaftler*innen von der ersten Vorlesung bis zur Promotion legen. Vielen Dank für diese Chance.
Ich möchte ebenfalls meinen Dank an Götz Lehmann für die Übernahme der Aufgabe zur Zweitkorrektur dieser Arbeit und als Mentor meiner Promotion ausdrücken. Schon während meiner Masterarbeit habe ich viel von deiner physikalischen Kompetenz und dem herzlichen Umgang mit Studierenden profitiert. Ich bin froh, dass sich der Kreis schließt und du auch jetzt wieder Teil dieses wichtigen Schritts in meiner Laufbahn bist und warst. Vielen Dank dafür.
An dieser Stelle ist es mir ebenfalls eine Freude mich für die Förderung durch Fulbright Germany und der Heine Research Academy (HeRA) zu bedanken, die es mir ermöglicht haben meinen Horizont zu erweitern und den wissenschaftlichen Austausch mit dem Lawrence Berkeley National Laboratory und der Dalian University of Technology anzustoßen und voranzutreiben.
I will always remember the time I spent at Lawrence Berkeley National Laboratory, and I am honored to work and discuss with you guys on interesting experiments. Thank you Vassilia for making this cooperation possible, and Kévin, Minok, and Xianglei for your support in the laser laboratory and on data interpretation.
Another extraordinary experience was made possible by Prof. Hongbin Ding who invited me to his research group at Dalian University of Technology. Thank you for your support and hospitality during my one month stay. Also thanks to you, Ding Wu and your colleagues for making this time most productive and enriching.
Diese Kooperation war nur möglich durch meine Kollegen vom IEK-4 am Forschungszentrum Jülich, Sebastijan Brezinsek, Gennady Sergienko und Jannis Oelmann. Danke für das Teilen eurer Resourcen und Zeit.
Viel zu verdanken habe ich ebenfalls dem gesamten Team vom Institut für Laser- und Plasmaphysik (ILPP). Danke Dirk für deine Laserexpertise und das jährliche Einordnen der

Gefährlichkeit unseres Lasersystems. Vielen Dank Claudia für deine Hilfe bei diversen administrativen Hürden. Mein großer Dank geht auch an Stefan fürs Lösen der kleineren und größeren Probleme, nicht nur technischer Natur. Natürlich auch vielen Dank an Alle, die jemals mit mir am ILPP gearbeitet und gelernt haben und die Arbeit am Institut nicht als solche haben wirken lassen.
Im Besonderen möchte ich an dieser Stelle meinen Dank für einige Wegbegleiter*innen einzeln ausdrücken:
Michael, dank dir habe ich vor knapp 6 Jahren entschieden meine Bachelorarbeit am Institut zu machen. Du bist einer der wichtigsten Wegbegleiter für mich, nicht erst seitdem wir uns gemeinsam durch unsere Doktorarbeit unter Corona-Bedingungen gekämpft haben. Du bist und bleibst Inspirationsquelle und Vorbild in wissenschaftlichen wie privaten Themen. Danke für deine Freundschaft.
Basti, nicht nur deine unglaubliche Ruhe bei der Justage des Laser Verstärkers und Oszillators, sondern auch deine professionelle Herangehensweise an unterschiedliche Probleme werden für mich immer Vorbild sein. Danke für die Ruhe und Herzlichkeit, die du ausstrahlst und mich hier und da geerdet haben.
Julian, ich möchte dir zum einen dafür danken, dass durch deine Vorarbeit das Projekt an dem ich arbeiten durfte und die Kooperation mit Jülich erst möglich gemacht worden ist. Zum anderen warst und bist du mir in vielen Dingen ein Vorbild und bin froh von dir lernen zu dürfen.
Jonah, im Zuge deiner Bachelorarbeit konnten wir gemeinsam die Vorpulseinheit realisieren. Vielen Dank dafür.
Jan, Marc und Nico, im letzten Jahr mussten wir drei den Laden hier am Laufen halten und im besten Fall voranbringen. Vielen Dank für eure neuen Perspektiven und Diskussionen, aus denen ich ein tieferes Verständnis für unseren Laser und die physikalischen Prozesse ziehen konnte.
Ein besonderer Dank geht an meine ehemaligen Kommilitonen und guten Freunde, Florian, Jens, Hannah, und Paulus. Danke für eure Unterstützung und Freundschaft während der anstrengenden Jahre des Physikstudiums und darüber hinaus. Ohne euch hätte ich das niemals geschafft.
Mit euch gibt es zum Glück auch mal Ablenkung von jeglichen physikalischen Themen: Vielen Dank an Max, Julian, Johanna, Yannik, Hannah und Jonathan.
Thank you Prudhvi for beeing the best flatmate I could imagine during the last years. In particular I acknowledge your countless attempts to distract me from the tough life as a PHD student by showing me ways to enjoy life.
To all my friends I met during my stay in the United States, thank you all for supporting me on my way up to now and hopefully further in the future. In particular I want to thank Sofia, Diane, Giuseppe, Matteo, Fabrizio, Daniela, Alex, and Lars.
Zu guter Letzt möchte ich mich bei meiner Familie bedanken, die bedingungslos hinter mir und meinen Entscheidungen steht und auf die ich mich immer verlassen kann. Danke, dass Ihr mir diesen Weg ermöglicht und alles etwas leichter gemacht habt. Ich habe euch lieb.

Eidesstattliche Versicherung

Ich versichere an Eides statt, dass die Dissertation von mir selbstständig und ohne unzulässige fremde Hilfe unter Beachtung der "Grundsätze zur Sicherung guter wissenschaftlicher Praxis an der Heinrich-Heine-Universität Düsseldorf" erstellt worden ist.

Düsseldorf, 08.11.2022

Steffen Mittelmann